

**Imaging Viscoelasticity in Hydropolymers and Breast Tissue with Ultrasound**

by

Mallika Sridhar Keralapura

B.S. in Electronics and Communication Engineering (Bangalore University) 1998  
M.S.E in Biomedical Engineering (University of Akron, Akron, Ohio ) 2001

A dissertation submitted in partial satisfaction of the  
requirements for the degree of  
Doctor of Philosophy

in

Biomedical Engineering

in the

GRADUATE DIVISION

of the

UNIVERSITY OF CALIFORNIA, DAVIS

Committee in charge:  
Dr. Michael F. Insana, Chair  
Dr. John M. Boone  
Dr. Scott I. Simon

Fall 2006

The dissertation of Mallika Sridhar Keralapura is approved:

---

Chair

Date

---

Date

---

Date

University of California, Davis

Fall 2006

**Imaging Viscoelasticity in Hydropolymers and Breast Tissue with Ultrasound**

Copyright 2006

by

Mallika Sridhar Keralapura

## Abstract

Imaging Viscoelasticity in Hydropolymers and Breast Tissue with Ultrasound

by

Mallika Sridhar Keralapura

Doctor of Philosophy in Biomedical Engineering

University of California, Davis

Dr. Michael F. Insana, Chair

Recent advances in molecular biology of breast cancer are providing new opportunities for imaging. For instance, signaling mechanisms between cancer cells and surrounding stromal cells control various facets of tumor progression including growth rate, degree of invasiveness, and metastatic potential. The stroma can respond to molecular signals by altering the local environment of the tumor. Some of the associated extra-cellular matrix changes are fibrosis, desmoplasia and associated edema that alter the mechanical properties of the tissue. Our overall goal for cancer imaging is to use ultrasound to track viscoelastic properties of breast tumors and thereby reveal essential new information about disease-specific changes. In this dissertation, we focus on developing the analytical and experimental imaging science for viscoelastic breast imaging. To conduct these studies, we developed tissue-mimicking hydro-polymers made from gelatin that helped us discover a

molecular-scale interpretation of the viscoelastic response. Gelatin polymers are simple to construct, and are elastically uniform within the resolution of the ultrasonic imaging system and share common viscoelastic features with breast tissue.

There are ways to mechanically stimulate media under investigation. We choose to apply external-quasi static stress fields because of its simplicity and safety for clinical trials, and because these stimuli probe the low frequency portion of the complex modulus spectrum, a region for which little is known. Guidelines/techniques established with gelatin are then applied for in-vivo imaging of normal volunteers and patient breast tissue.

Spatio-temporal behavior of gelatin is described by linear viscoelastic theory as developed for polymeric solids. Creep and stress relaxation measurements generate broad, continuous, bimodal spectral distributions that can be related to molecular-scale processes. These distributions guide data modeling resulting in retardance time estimates that are associated with spectral peaks, thereby offering a concise summary of viscoelastic behavior reflective of underlying microstructure. We explore the role that ultrasonic imaging parameters like acquisition time and ultrasonic frame rate play in maximizing lesion visibility in images. Other factors such as stress stimulus uncertainty, and interference from purely viscous mechanisms influence the values of parameters and image contrast. Similar techniques applied on in-vivo breast tissue with volunteers revealed the range of applied stresses for which linear viscoelastic models apply. The response data obtained from hydropolymers and in-vivo breast tissue were characteristic of lightly cross-linked amorphous solid polymers. Preliminary clinical viscoelastic imaging on patients with breast tumors yielded

tumor specific retardance time contrast consistent with the underlying alteration in extracellular matrix for these tumors.

---

Dr. Michael F. Insana  
Dissertation Committee Chair

# Contents

<b>List of Figures</b>	<b>iv</b>
<b>List of Tables</b>	<b>ix</b>
<b>1 Introduction and Literature Review</b>	<b>1</b>
1.1 Contrast Mechanisms for Ultrasound . . . . .	3
1.2 Breast Tissue: Gross Anatomy and Microstructure . . . . .	5
1.3 Breast Cancer Biology . . . . .	8
1.4 Molecular Imaging Techniques . . . . .	13
1.5 Contrast Mechanisms for Ultrasound Viscoelasticity Imaging . . . . .	14
1.6 Imaging mechanical properties using Ultrasound . . . . .	16
1.6.1 External methods . . . . .	18
1.6.2 Internal methods . . . . .	20
1.7 Specific Aims . . . . .	23
1.8 Strategy for Viscoelastic Imaging . . . . .	24
1.8.1 Gelatin hydro-polymers as physical models . . . . .	24
1.8.2 Algorithms for Displacement Estimation for Viscoelastic Imaging . . . . .	27
1.9 Scope and Outline . . . . .	28
<b>2 Viscoelastic Measurements on Gelatin Hydropolymers</b>	<b>30</b>
2.1 Methodology . . . . .	32
2.1.1 Constitutive Equation . . . . .	33
2.1.2 Uniaxial Compressive Stress: Creep . . . . .	34
2.1.3 Shear Stress and Strain . . . . .	43
2.1.4 Uniaxial Compressive Strain: Stress Relaxation and Relaxation Spectra . . . . .	44
2.1.5 Gelatin Model . . . . .	46
2.1.6 Gelatin Sample Preparation . . . . .	48
2.1.7 Viscoelastic Measurement Techniques . . . . .	50
2.1.8 Data Processing . . . . .	53

2.1.9	Goodness of Fit and Model Order . . . . .	54
2.2	Results . . . . .	56
2.2.1	Viscosity . . . . .	56
2.2.2	Linearity . . . . .	56
2.2.3	Poisson's Ratio . . . . .	57
2.2.4	Effects of Acquisition Time . . . . .	58
2.2.5	Validation . . . . .	59
2.2.6	Image Contrast . . . . .	61
2.2.7	Viscoelastic Spectra . . . . .	63
2.3	Discussion . . . . .	65
2.4	Appendix A . . . . .	69
2.5	Appendix B . . . . .	70
<b>3</b>	<b>Viscoelastic Imaging on Gelatin Hydropolymers</b>	<b>73</b>
3.1	Methodology . . . . .	76
3.1.1	Constitutive Equations for Viscoelastic Imaging . . . . .	76
3.1.2	Parameterizing Creep Data for Imaging . . . . .	79
3.1.2.1	Method I: $\chi^2$ Model Fitting. . . . .	79
3.1.2.2	Method II: Hankel-SVD Method. . . . .	80
3.1.3	Simulations . . . . .	83
3.1.4	Retardation-Time Error Analysis . . . . .	85
3.1.5	Gelatin Sample Preparation . . . . .	87
3.1.6	Imaging Viscoelastic Properties . . . . .	88
3.1.6.1	Computer controlled stress. . . . .	89
3.1.6.2	Freehand stress. . . . .	90
3.1.7	Acquisition and processing parameters . . . . .	90
3.2	Results . . . . .	90
3.2.1	Retardance Time Images . . . . .	92
3.2.2	Acquisition Time . . . . .	94
3.2.3	Linear Viscous Creep . . . . .	95
3.2.4	Stress variance . . . . .	97
3.3	Discussion . . . . .	98
<b>4</b>	<b>Viscoelastic Imaging on In-vivo Breast Tissue</b>	<b>101</b>
4.1	Methodology . . . . .	104
4.1.1	Volunteer Studies . . . . .	104
4.1.1.1	Positioning and data acquisition . . . . .	104
4.1.1.2	Linearity Testing: . . . . .	106
4.1.1.3	Creep Measurement: . . . . .	107
4.1.1.4	Imaging Creep: . . . . .	107
4.1.1.5	Creep Recovery Measurement: . . . . .	107
4.1.1.6	Stimulus effects: . . . . .	108

4.1.2	Data Modeling and Analysis . . . . .	108
4.1.2.1	Constitutive Models . . . . .	108
4.1.2.2	Parameterizing Creep Data . . . . .	109
4.1.2.3	Effects of acquisition time . . . . .	111
4.1.3	Pilot Patient Study . . . . .	111
4.2	Results . . . . .	112
4.2.1	Volunteer Results . . . . .	112
4.2.2	Patient Studies . . . . .	120
4.3	Discussion . . . . .	121
<b>5</b>	<b>Overall Discussion and Conclusions</b>	<b>130</b>
5.1	Overall Discussion . . . . .	131
5.1.1	Spectra and Data parameterization . . . . .	131
5.1.2	Viscoelastic measurements . . . . .	133
5.1.3	Sources of uncertainty affecting contrast . . . . .	135
5.1.4	In-vivo feasibility and methodology . . . . .	137
5.2	Conclusions . . . . .	138
	<b>Bibliography</b>	<b>141</b>
<b>A</b>	<b>Projects and Publications</b>	<b>150</b>

# List of Figures

1.1	Example sonograms from (a) benign and (b) malignant tumors. . . . .	3
1.2	Illustration of breast tissue gross anatomy and microstructural views of breast lobules. In the figure, (a) breast tissue macrostructure (b) light microscopy images showing lobular structures (c) immunostained image showing milk glands in a lobule. . . . .	6
1.3	Images of the distribution of collagen fibers and proteoglycan molecules in the inter- and intra lobular stroma. In the figure (a) shows an electron microscopy image of loose intra-lobular stroma and (b) shows electron microscopy image of dense inter-lobular stroma. . . . .	7
1.4	Illustration of collagen fibers with associated proteoglycans. Also shown in a zoomed version is one proteoglycan molecule and its ability to alter water structuring due to charges it carries. . . . .	8
1.5	Histologic section of breast tissue and a corresponding cartoon. . . . .	9
1.6	Illustrations showing progression of breast cancer from (a) Ductal carcinoma In Situ (DCIS) to (b) Angiogenesis and collagen secretion stages to (c) Invasive ductal carcinoma. . . . .	10
1.7	(a) Illustration of the structure of collagen fibrils in connective tissue (b) Illustration of gelatin aggregates (c) Electron microscopy images of gelatin at 2 levels of concentration. . . . .	26
2.1	(a) Creep curves for a second-order ( $L = 2$ ) Voigt model and a step stress stimulus are illustrated. Curve a is drawn directly from Eq (2.8) with finite $\eta_0$ ; its slope at $t \gg T_2$ is $\sigma_a/\eta_0$ . Curve b is from the same equation where $\eta_0 = \infty$ . In both cases $\epsilon_2/\epsilon_1 = 2.5$ , $T_1 = 3$ s, and $T_2 = 100$ s. (b) The corresponding Fourier spectra, $\check{D}(\omega)$ , are from Eq (2.10). Spectra from a step and 1 s ramp stress stimulus are compared. . . . .	37

2.2	(a) Retardation spectra from simulated data. Plotted are $\tilde{L}(\omega) = L(\tau) _{\tau=1/\omega}$ for comparison with the Fourier spectrum. Creep data were generated from Eq (2.12) for $\epsilon_0 = \sigma_a/\eta_0 = 0$ assuming a broadband, bi-modal input as given by the circle points (Input). Estimated retardation spectra (RS), $\tilde{L}^{(k)}(\omega)$ for $k = 1, 2, 5, 6$ , are compared to the Fourier spectrum (FS), $\check{D}(\omega)$ , computed from the same data. (b) $\tilde{L}^{(6)}$ estimates without noise in the creep data and with noise (signal-to-noise ratio = 32.2 dB). An 9-th order polynomial filter was applied to the noisy data before estimation. . . . .	41
2.3	Limitation of $L^{(k)}(\tau)$ for representing retardance time distributions. The abscissa is $b/a$ from the log-normal input distribution $L(\tau) = \exp(-(\ln \tau - a)^2/2b^2)$ . The ordinate is the full-width-at-half-maximum bandwidth of retardance spectral estimates. Circles denote the exact output bandwidth for the input distribution, while the curves are bandwidths for $k$ th-order estimates using noiseless creep data. Results suggest that the $L^{(6)}(\tau)$ represents bandwidths of log-normal distributions above 150 s with acceptable bias error. . . . .	42
2.4	Illustration of collagen structures in connective tissue (fibril) and in gelatin (aggregates). . . . .	47
2.5	Illustrations of four viscoelastic experiments. (a) Measurement method A applies uniaxial stress or strain stimuli to unconfined gelatin samples to estimate compressive relaxation modulus $E(t)$ or compressive creep compliance $D(t)$ . It is also the ultrasonic strain imaging technique. (b) Method B applies uniaxial strain to estimate the compressive wave modulus $M(t)$ for rigidly confined sample boundaries. (c) Method C is a cone-plate rheometer applied to estimate shear creep compliance $J(t)$ . (d) Method D applies an indenter to gelatin samples to estimate the elastic modulus $E_0$ . All positions are computer controlled with sub-micron accuracy, and forces are measured with a precision of 0.01 g. . . . .	50
2.6	(a) Shear creep measured with applied step stresses of $\sigma'_a = 3$ and 30 Pa using Method C and Type B gelatin (5.5%). (b) Viscosity estimates (Section 2.1.3) versus time for creep data at 30 Pa. Steady-state values were attained beginning at $\sim 600$ s. (c) Example of shear creep recovery curve for Type A gelatin at $\sigma'_a = 100$ Pa. Values calculated from the creep and recovery phases are reported separately. . . . .	55
2.7	Demonstrations of linearity. (a) Stress-strain curves for stiff (10%) and soft (5.5%) Type A gelatin using unconfined samples and uniaxial harmonic stimuli (Method A). The two stress levels indicated were used in subsequent creep measurements. (b) Shear creep Fourier spectra for Type B gelatin (Method C). . . . .	57
2.8	Poisson's ratio estimates versus time, $\nu(t)$ . Error bars denote one standard deviation computed by propagating displacement measurement errors. . . .	58

2.9	(a) Dependence of $T_\ell$ on acquisition time, and the effect of eliminating steady-state viscosity (linear term in Eq (2.17)). $T_1$ and $T_2$ estimates for a third-order Voigt model are shown. (b) Variation of $T_1$ contrast over acquisition time is shown. . . . .	59
2.10	Comparisons of measurements made using different methods. Samples were all type A gelatin aged 3 days. (a) Elastic modulus; (b) equilibrium compliance; and (c) steady-state viscosity under compression. Error bars are standard deviations that indicate uncertainty between repeated measurements. . . . .	60
2.11	(a) Contrast between 10% and 5.5% homogeneous gelatin samples for seven compliance parameters. (b) Example $\epsilon_0$ image for a composite sample consisting of 5.5% gel background with a 10% gel inclusion. (c) Example $T_1$ image. . . . .	60
2.12	Normalized Fourier, retardation, and relaxation spectra. (a) Unconfined type A gelatin samples (aged 3 days) loaded uniaxially at $\sigma_a = 860$ Pa are measured for 2000 s using Method A. (b) Confined type A gelatin samples (aged 1 day) strained uniaxially at $\epsilon_a = 0.02$ are measured for 2500 s using Method B. (c) Type B gelatin samples (aged 1 day) sheared at $\sigma'_a = 3$ Pa are measured for 3000 s in a rheometer using Method C. (d) Unconfined type A gelatin samples (aged 3 days) strained uniaxially at $\epsilon_a = 0.08$ are measured for 2000 s by combining Methods A and B. Arrows indicate frequencies corresponding to the resonandance times given in Table 2.1. Spectral amplitudes are uniformly reduced across the bandwidth as samples age. . . . .	63
2.13	Effects of rest time on viscoelastic estimates. Top: Variation of $T_1$ (left group), $T_2$ (middle group), and $T_3$ (right group) for a third-order Voigt model are shown for baseline measurements (0) and rest times of 1 and 2 hours. Error bars indicate fitting uncertainties. Bottom: Table showing initial baseline retardance times in seconds and percent biases for rest times of 1 or 2 hours between measurements. . . . .	72
3.1	(a) Normalized $H(\tau)$ distribution for gelatin compression in a confined geometry. (b) Normalized $L(\tau)$ distribution for gelatin compression in an unconfined geometry similar to imaging experiments. Both curves are reproduced from (Chapter 2) [1]. Markers along the $\tau$ axes indicate estimates of peak resonandance times by applying <i>Method I</i> with and without weighting and <i>Method II</i> as described in Section 3.1.2 . . . . .	78
3.2	Points marked (o) are the log-normal retardation spectra input into the simulation (peak value is 100 s and the bandwidth is 220 s). The lines are estimates of the spectrum from Eq (3.3) fit to the data using <i>Method I</i> (solid line) and <i>Method II</i> (dashed line). . . . .	84

3.3	The coefficient of variation for $T_1$ is plotted versus that for the input stress. Predicted values (analytical) and those estimated from simulation (computational) are shown. . . . .	84
3.4	Imaging viscoelastic properties of a gelatin phantom. The object (left) is compressed from above and held while the ultrasound system records a series of RF echo frames from which a sequence of strain images (center) is computed. Pixels from the strain-image sequence are fit to viscoelastic models to compute $T_\ell$ images (right). . . . .	88
3.5	(a) Model order estimates from <i>Method I</i> for two SNR values, 18 dB and 40 dB, and varying $L(\tau)$ bandwidth. (b) Corresponding values for $T_m$ ( <i>Method I</i> ) and $T_\ell$ ( <i>Method II</i> ). The input peak value is 100 s. . . . .	91
3.6	(a) <i>Method I</i> Mean % contrast for parametric images. Error bars denote 1 standard deviation of the mean. <i>Method I</i> images: (b) B-mode image showing 0.8 cm inclusion, (c) elastic strain image $\epsilon_0$ , (d) $T_1$ image, (e) $T_2$ image, (f) $\sigma_a/\eta_0$ image, and (g) $\chi^2$ map using Eq (3.4). . . . .	92
3.7	(a) Variation in retardance time estimates with acquisition time for <i>Method I</i> and a gelatin phantom. (b) Variation in retardance-time contrast with acquisition time. . . . .	94
3.8	(a) $T_2$ background and inclusion estimates at different scaled $\sigma_a/\eta_0$ values (b) Corresponding contrast values. . . . .	95
3.9	$T_1$ variation over short acquisition times with and without compensating for linear viscous creep. . . . .	96
3.10	(a) Freehand force applied over time to a gelatin sample with and without feedback. (b) Relative stress variability as recorded from two volunteers that apply forces with and without feedback. . . . .	97
4.1	(a) Volunteer positioning for long-duration echo frame acquisitions (b) Coupling of transducer and force sensor when force measurement is made. . . .	104
4.2	General protocol used for volunteer studies. . . . .	106
4.3	Freehand force application to breast using transducer-sensor combination for linearity testing. . . . .	112
4.4	Force-strain curves for 2 breast tissue acquisitions. Mean strain was calculated for the region-of-interest indicated in Fig 4.2. . . . .	113
4.5	Force-strain curves for forces between 2-5 N for visualization of the linear regime of breast tissue. . . . .	114
4.6	(a) Ramp and hold freehand force applied to the breast for up to 200 s. (b) Creep response over time. . . . .	115
4.7	Creep response over time for (a) 5.5 N and (b) 7.5 N applied force. . . . .	116
4.8	(a) Creep-Relaxation experiment applied to the breast over 200 s. (b) Creep-Relaxation response over time. . . . .	117

4.9	Freehand force applied to the breast with transducer-sensor combination. Plotted alongside are estimated creep curves. (a-b) no force feedback (c-d) real-time sonogram feedback (e) Creep estimated when only transducer with plate was used as the compression device. . . . .	124
4.10	Retardance spectra for breast tissue. Spectra mapped alongside gelatin spectra reproduced from [20]. Markers on the $\tau$ axis indicate retardance times in accordance to Table-4.1. ‘*’ indicates no weighting whereas ‘x’ indicates weighting. . . . .	125
4.11	(a) Sonogram (b) $T_1$ image of normal breast tissue. (c) Variation of retardance times in fat and glandular regions over acquisition time (d) Variation of contrast between glandular and fat regions over acquisition time. . . . .	125
4.12	(a) Sonogram (b) Elastic strain $\epsilon_0$ (c) $T_1$ image (d) Variation of $T_1$ over acquisition time for lesion and background areas (e) Variation of contrast over acquisition time. Mass histologically determined as a fibroadenoma. . . . .	126
4.13	Sonograms and elastic strain $\epsilon_0$ images of malignant carcinomas. Reproduced from Barakat <i>et. al.</i> . . . . .	127
4.14	Sonogram, Elastic strain $\epsilon_0$ and $T_1$ images for 2 cases of benign fibroadenomas. . . . .	128
4.15	Sonogram, Elastic strain $\epsilon_0$ and $T_1$ images for 2 cases of malignant ductal carcinomas. . . . .	129

# List of Tables

2.1	Viscoelastic parameters for 5.5% gelatin acquired by fitting measurements to model functions. First column lists the discrete viscoelastic model order. Second column contains compressive compliance [kPa <sup>-1</sup> ] and retardance time [s] constants from data of Fig 2.12a. Third column contains wave modulus [kPa] and relaxation time [s] constants from Fig 2.12b. Fourth column contains shear compliance [kPa <sup>-1</sup> ] and retardance time constants from Fig 2.12c. Fifth column contains compressive relaxation modulus [kPa] and relaxation time constants from Fig 2.12d. $Q$ is the probability from $\chi^2$ goodness-of-fit test. . . . .	62
3.1	<u>Algorithm for Method I</u> . . . . .	80
3.2	<u>Algorithm for Method II</u> . . . . .	81
4.1	<u>Algorithm for Data Parameterization</u> . . . . .	110

# Chapter 1

## Introduction and Literature Review

Breast cancer is the leading cause of death in women between the ages of 35 and 54 years and accounts for 32% of all cancers. According to the American Cancer Society (ACS), 95% of cases were from women aged 40 or higher during 1998-2002. ACS statistics indicated that there will be 211,240 new cases of invasive breast cancer and 40,410 deaths resulting from the disease in 2005 [2]. These mortality numbers have decreased at a rate of 2.3% per year from 1990 with larger decreases in younger women. Many improvements in patient outcome can be attributed to advances in diagnostic imaging and therapeutics.

Currently, screening for breast cancer involves mammography in addition to sonography (ultrasonic imaging). Primary role of breast sonography is to differentiate solid tumors from cysts and to guide needles during biopsies for histological evaluation of the disease. Mammography is most accurate for detecting early tumors that produce microcalcifications, but can be associated with decreased detection sensitivity in dense breasts [3]. When

used in conjunction with sonography especially in dense breasts, detection sensitivity of small tumors increases to 94% from 75% [3].

Unfortunately, sonograms or mammograms are not always cancer specific. In sonograms, most tumors appear hypoechoic (slightly dark), hence, benign masses (fibroadenomas or fibrocystic changes) cannot be differentiated from malignant lobular or ductal carcinomas (see Fig 1.1). Differential diagnosis requires invasive biopsy procedures that introduce risks and discomfort to the patient and increase hospital costs. Thus, new effective imaging technologies that are sensitive and specific to early stage cancers can contribute significantly to early diagnosis, reduce unwanted biopsies, and hence reduce mortality rates.

Our long term goal is to increase cancer specific diagnostic information by using ultrasound. Given that currently no imaging technique can really discriminate tumors non-invasively for all types of cancers, we aim to integrate new ultrasound technologies with already existing diagnostic imaging techniques to enhance discriminative diagnosis of tumors. Our methodology involves imaging stromal features of breast tissues without contrast enhancement, safely, and at low cost using the unique capabilities of ultrasound. Ultrasound is highly sensitive to small changes in the mechanical or viscoelastic properties of tissues that are altered significantly during the progression of the disease (see Sec. 1.3). Measurement of these properties require small deformations applied to the tissue. Thus, we wish to integrate advances in cancer biology with the understanding of ultrasound interactions with tissue to visualize cancer related changes.

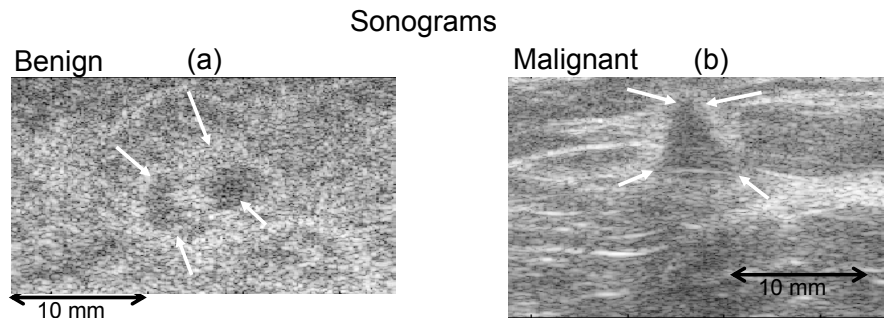


Figure 1.1: Example sonograms from (a) benign and (b) malignant tumors.

## 1.1 Contrast Mechanisms for Ultrasound

Ultrasonic imaging relies on reflections and scattering from tissue structures to produce the signal that appears in sonograms. Spatial variations in acoustic impedance (function of mass density and speed of sound) and bulk compressibility modulus are responsible for these signals or echoes and thus provide the object contrast necessary for sonographic visualization of tissue. In particular, bulk modulus changes are the primary cause of ultrasonic backscatter in soft tissue [4] and normally vary within 15% [5].

Of the four types of body tissues - mesenchymal, epithelial, reticuloendothelial, and nervous - ultrasound is most sensitive to the mesenchyma (connective tissue stroma, ducts, lobules, microcalcifications, muscle, lymphatics, collagen fibers, etc.) [6]. Sound is scattered at the surfaces of these microstructures due to differences in density and bulk compressibility with the statistical features of the echo signals directly related to the size [7], preferred orientation and relative amounts of these structures [4]. The echo signal is strongest when the wavelength of sound is approximately equal to the size of the scat-

terer [8]. Hence for imaging frequencies in the diagnostic range, 8-20 MHz (wavelength: 192-77  $\mu\text{m}$ , assuming speed of sound in tissue = 1540 m/s), strongest scatterers will be the connective tissue stroma (collagen fibers, vasculature etc.) when sizes are equal to the wavelength. Sensitive sonographic detection of scatterers is essential for accurate displacement estimation for tracking mechanical properties of the stroma. Thus ultrasound excitation frequency (speed/wavelength) dictates the scale of structures that scatter sound energy. If higher frequencies are used, greater than 100 MHz, cellular structures will primarily contribute to the signal. This is associated with a decreased depth of penetration since ultrasound is highly attenuated at higher frequencies. Scattered energy is decreased by 100 dB if 1 cm of tissue is traversed (attenuation is 0.5 dB/cm/MHz) in pulse-echo ultrasound at 100 MHz. 3-5 cm of tissue can be traversed if 10 MHz ultrasound frequency is used with clinical scanners that have attenuation-based compensation critical for breast imaging.

The wavelength also determines the limit of spatial resolution for ultrasound. For a 10 MHz broadband pulse with 50% fractional bandwidth, the axial resolution achievable is 0.3 mm ( $2*\lambda$ ). This short pulse correlates the response of random scatterers in its volume to generate fully developed speckle evident in sonograms (see Fig 1.1). Consequently, larger structures on the order of the wavelength can be resolved easily but statistical properties of speckle also describe scatterers much smaller in size. Furthermore, a broadband pulse not only keeps the spatial resolution high but also undergoes minimal distortion during deformations resulting in efficient correlation between scatterers for displacement estimation

[9].

Thus, for tracking deformation patterns in breast stroma due to a mechanical stimulus, ideal frequencies are standard diagnostic ranges between 8-20 MHz given its depth of penetration and wavelength for resolving stromal structures. Choice of a broadband pulse is required for high spatial resolution and for increased correlation among scatterers during deformation.

## **1.2 Breast Tissue: Gross Anatomy and Microstructure**

In this section, we describe breast anatomy and its microstructure as it applies to ultrasonic imaging of stromal mechanical properties. Fig 1.2a shows breast tissue anatomy. The organ comprises of many lobules, which consist of milk producing glands. The lobules and glands are linked by thin tubes called ducts. The connective tissue surrounding the lobules and large ducts are dense connective tissue while tissue within lobules are loose connective tissue [10]. The layer just below the skin is fat and muscle connects the breast to the chest wall. Fig 1.2b shows a light microscopy image of a breast tissue slice for the purpose of demonstration of the lobular units. These lobular units have milk producing glands in them as shown in Fig 1.2c.

Since mesenchymal tissue is the primary source of ultrasonic backscatter, the size, orientation and distribution of collagen in the inter and intra lobular spaces of the breast are important features for interpreting sonographic images. Attached to these structures are other

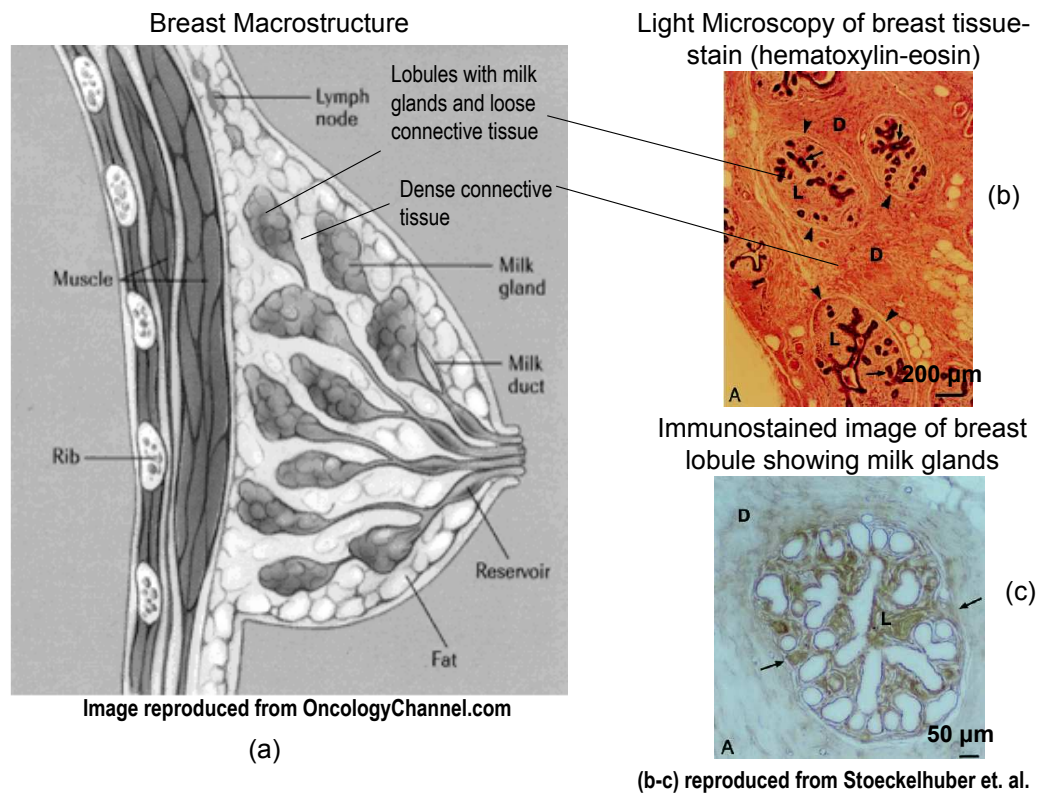


Figure 1.2: Illustration of breast tissue gross anatomy and microstructural views of breast lobules. In the figure, (a) breast tissue macrostructure (b) light microscopy images showing lobular structures (c) immunostained image showing milk glands in a lobule.

extra-cellular matrix (ECM) molecules such as proteoglycans [10]. They are comprised of hydrated glycoproteins covalently bonded to polysaccharide chains called glycosaminoglycans (GAGs). GAGs carry large numbers of negatively charged groups that bind water molecules. Other glycoproteins such as fibronectin link cells to the ECM; laminin is present in the membrane lining ducts and lobules and connects cells within those components to the ECM [11]. Fig 1.3 shows electron microscopy images of the dense and loose breast stroma reproduced from [10] to illustrate the distribution of collagen fibers and associated proteoglycans. The fiber orientation in the intra-lobular stroma is quasi-random with large

number of proteoglycans attached. These molecules are also present without collagen association loosely in the ECM (see arrows in Fig 1.3a) and play major roles of altering tissue viscosity [10]. Inter-lobular stroma has fibers more regularly spaced again associated with large number of proteoglycans.

To understand the role of a proteoglycan in structuring water, Fig 1.4 illustrates it with a cartoon of the ECM zooming in on a proteoglycan molecule.

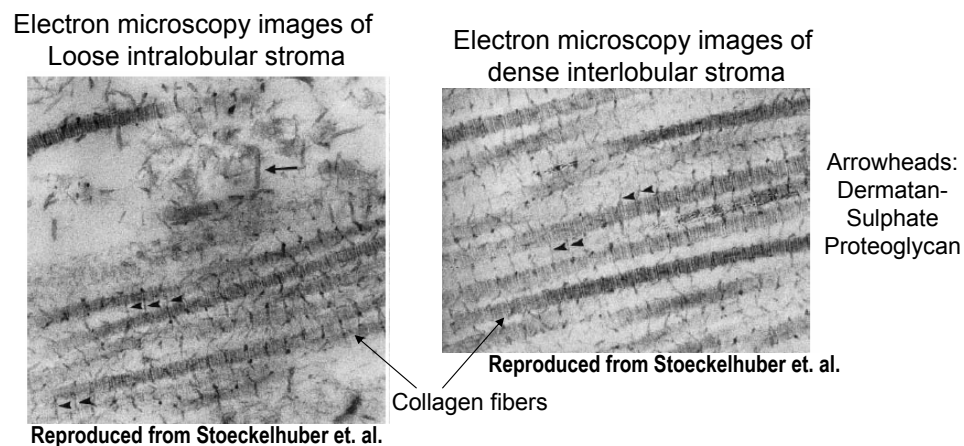


Figure 1.3: Images of the distribution of collagen fibers and proteoglycan molecules in the inter- and intra lobular stroma. In the figure (a) shows an electron microscopy image of loose intra-lobular stroma and (b) shows electron microscopy image of dense inter-lobular stroma.

If the distribution, size and orientation of collagen that gives rise to ultrasonic backscatter is tracked precisely using ultrasound when deformations are applied, stromal viscoelastic/mechanical properties can be extracted. This underlying stroma is altered during cancer progression as discussed in Sec. 1.3 below giving ultrasonic based viscoelastic imaging its diagnostic capabilities.

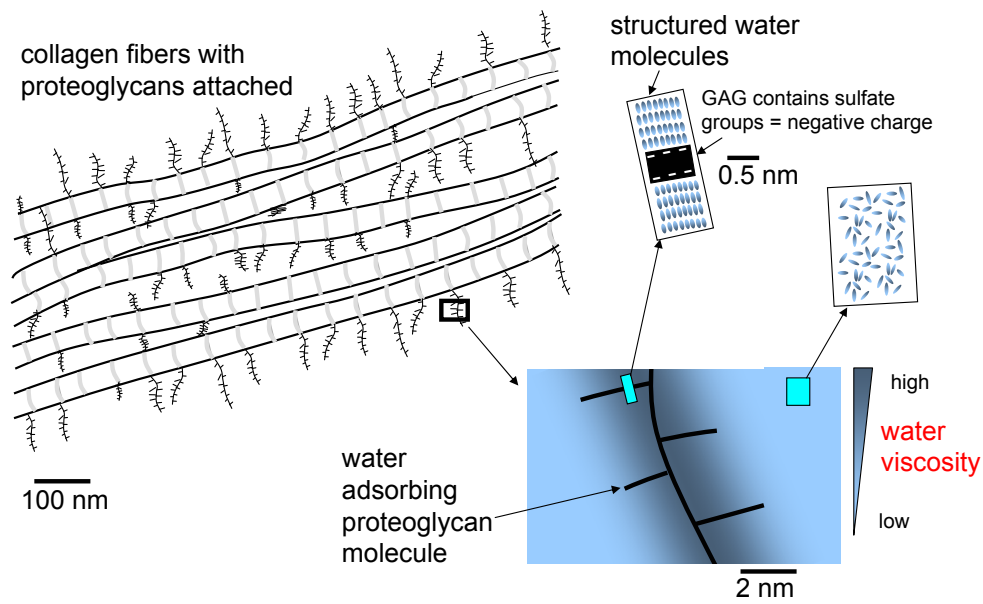


Figure 1.4: Illustration of collagen fibers with associated proteoglycans. Also shown in a zoomed version is one proteoglycan molecule and its ability to alter water structuring due to charges it carries.

### 1.3 Breast Cancer Biology

The most common cancers are carcinomas of the mammary duct and lobule [12]. Figures 1.5 and 1.6 illustrate the progression of ductal carcinomas from normal tissue. Fig 1.5 shows a normal histologic section of breast tissue and a cartoon alongside, displaying a ductal region and surrounding connective tissue (mesenchyma) comprised of stromal cells (fibroblasts), collagen fibers (Types I, III [13]) and blood supply (arterioles and capillaries). The basement membrane (Type IV collagen [11]) is lined by epithelial cells and encloses the milk duct. Basement membrane is a specialized structure that provides a stable foundation on which normal epithelial cells adhere. Although it holds normal cells tightly in place, it also allows access to nutrients, immune cells and soluble growth factors required

for tissue maintenance.

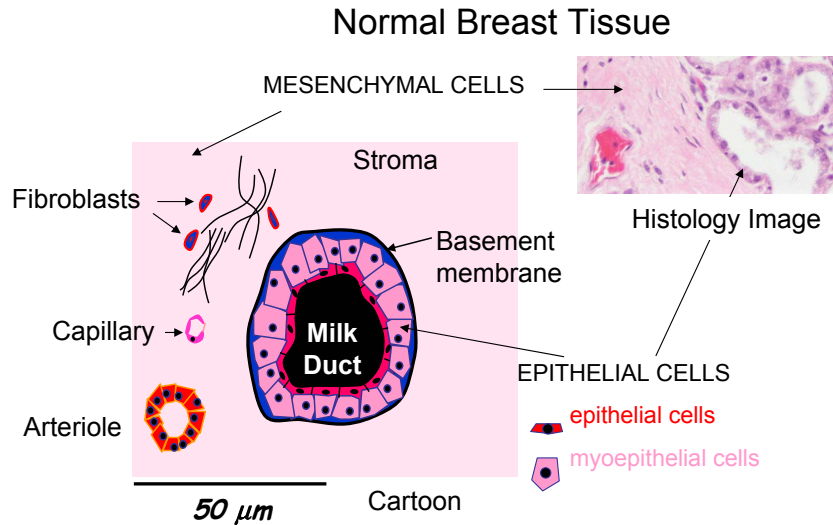


Figure 1.5: Histologic section of breast tissue and a corresponding cartoon.

An initiator such as a carcinogen (radiation, chemicals, viruses etc.) transforms the genetic material (DNA) of epithelial cells. These mutated cells remain dormant until acted upon by promoters such as hormones. The balance between promoters and inhibitors determines neoplastic growth rate [6]. Thus, tumors arise from cells that have sustained genetic mutations resulting in deregulation of several of their normal growth-controlling mechanisms [12].

Adenocarcinoma of the breast often begins as ductal carcinoma in situ (DCIS) characterized by epithelial hyperplasia (Fig 1.6a). The development and activities of these cells depend on the interaction with the surrounding environment (basement membrane and underlying stroma). The hyperplastic epithelial cells use signaling to recruit a variety of stromal cells throughout the growth process. For instance, cancer cells secrete

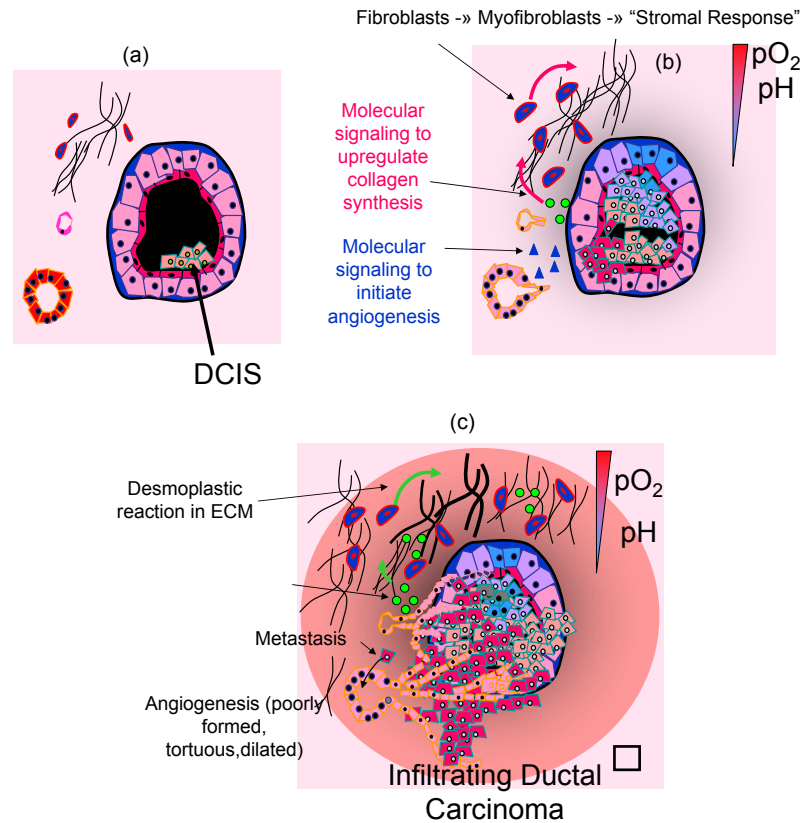


Figure 1.6: Illustrations showing progression of breast cancer from (a) Ductal carcinoma In Situ (DCIS) to (b) Angiogenesis and collagen secretion stages to (c) Invasive ductal carcinoma.

growth factors such as TGF- $\beta$ 1 which enhances its proliferation and further converts some surrounding stromal fibroblasts to myofibroblasts to begin the secretion of collagen and fibronectin. This is a stromal response as a consequence of cell signaling. Other factors such as Platelet-Derived-Growth-Factor (PDGF) expressed by cancer cells is chemotactic and hence recruits macrophages from surrounding tissue to enhance fibroblast conversions. Thus, both epithelial and stromal compartments co-develop [12]. In these early stage cancers, the stromal response is protective in nature [12], since myoepithelial and myofibroblasts secrete lysyl oxidase, an enzyme that crosslinks collagen and elastin stabilizing the

matrix preventing invasion of the basement membrane.

As cancer cells grow to fill the duct (Fig 1.6b), they turn on an “angiogenic switch” [14] triggered by metabolic stress (low  $pO_2$ , pH and hypoglycemia), mechanical stress (pressure generated by proliferating cells), inflammatory responses and genetic mutations. Angiogenic molecules then emanate from various cells like cancer cells, stromal cells, blood and the ECM to promote angiogenesis (formation of new blood vessels). For instance Vascular-Endothelial-Growth-Factor (VEGF) is upregulated that increases vascular permeability inducing formation of new vessels [12]. Since vascular cells (endothelium) must penetrate the basement membrane in order to lay down new blood vessels, molecules such as matrix metalloproteinases (MMPs) play a vital role in remodeling the ECM. They degrade, or proteolyse the ECM allowing blood vessels to enter the tumor and tumor cells to escape the basement membrane thereby creating an environment conducive to tumor formation.

Once the basement membrane is breached, DCIS becomes Invasive Ductal Carcinoma (IDC) (Fig 1.6c). Now tumor cells are in close proximity with stromal cells and heterotypic paracrine signaling occurs resulting in large number of myofibroblast conversions. These then secrete large amounts of collagen and fibronectin that stiffens the tumor. Macrophages contract and help stiffen lesions even further. Stiffening or *Desmoplasia* on the leading edge of the tumor causing it to grow in size. As the amount of collagen increases, dermatan sulphate proteoglycan content decreases 2-7 fold [15] for loose and dense connective tissue respectively, worsening the edema already present from the leaky new vasculature and

poor lymphatic systems. Benign solid tumors, like fibroadenomas progress quite differently and often feature increased collagen density with proportional increase in proteoglycan molecule concentration. In fact, the milk duct is compressed to a thin border due to the increase in collagen density. Thus, we expect fibroadenomas to be stiffer than the surrounding tissues (palpable) and more viscous.

The tumor now has high metastatic potential since transformed epithelial cells can enter the leaky neovasculature and poorly functioning lymphatics. Invasive tumors also secrete large amounts of MMPs which allow for breakdown of the ECM and extravasation of the tumor cells into the blood stream. Metastasis is a rare event and requires a perfect environment during tumor cell extravasation from the host tissue and intravasation into the new tissue after traveling through the vasculature [16]. Thus having metastatic potential is not sufficient to have a metastatic event.

Thus, the progression of breast cancer from in situ hyperplasia to metastatic disease involves interplay among cellular signaling and micro-environmental responses (eg. Desmoplasia, Edema); the former can be monitored using molecular imaging methods and the latter using ultrasonic methods. Hence, though breast adenocarcinomas begin in epithelial cells, the importance of the stromal compartment in cancer formation gives ultrasound based viscoelastic imaging its diagnostic capabilities.

## 1.4 Molecular Imaging Techniques

Molecular imaging techniques are well suited for imaging cancer directly. Successful techniques enhance object contrast for molecular-scale events by targeting circulating *imaging probes* for attachment to specific sites of disease. Standard modalities then image the energy emitted or reflected from the attached probes. One approach to molecular imaging employs integrin-based imaging probes to identify regions of enhanced angiogenic (new blood vessel) activity [17, 18]. Other approaches target gene expression and protein functions [19, 20]. Each of these uses a probe that targets signaling molecules or receptor sites. The challenges with these techniques is to design agents with targets so that they remain active while circulating in the blood stream but seek out the target effectively. A less direct approach uses  $^{18}\text{F}$ -PET probes to quantify changes in tumor cell metabolism that are highly correlated with cancer [21]. Other methods use confocal and multi-photon microscopy to visualize the effects of ECM-cell signaling on stromal microstructure, in vivo [22] using autofluorescence to generate the contrast necessary to study ECM structure.

Rather than directly imaging cancer signaling, we wish to image the effects of signaling or the micro-environment of the tumor. For instance, viscoelastic properties of breast tissue under compression will depend on the ECM organization of the inter-lobular and intra-lobular connective tissue stroma. This organization is altered during cancer progression giving rise to desmoplasia, fibrosis and associated edema. These micro-environmental changes can be accessed with ultrasound. Furthermore, by measuring viscoelastic properties of the tissue, it is possible to track stromal changes that could help us detect and

classify lesions bearing in mind that classification will depend on patient physiology, age and menstrual cycle [23], tumor grade etc. Thus, imaging mechanical features of cancers using ultrasound is an indirect method without contrast enhancement. Such methods can be implemented without the use of targeted probes, hence are non-invasive, inexpensive and can be integrated into the standard screening protocol used for diagnosis of breast cancers, potentially decreasing the number of unwanted biopsies.

## **1.5 Contrast Mechanisms for Ultrasound Viscoelasticity**

### **Imaging**

As described above, breast tumors stiffen significantly [24] from *Desmoplasia* and *Edema*, which is why physicians palpate tissues to look for possible masses. Palpation is however effective only for large stiff masses that are superficial. Remote palpation can be done by exploiting the phase sensitive nature of ultrasonic imaging systems to measure very tiny motion, on the order of microns. Though the spatial resolution is limited by the pulse wavelength, the echo phase allows us to reliably track micron-scale scatterer motion following a deformation [9]. Motion tracking can be done with sophisticated correlation or regularized methods (Details in Sec. 1.8.2) by comparing echoes reflected from scatterers before and after deformation. High echo coherence (similarity of echoes) is crucial for precise displacement measurement. Strain experienced by the tissue due to the applied stress stimuli can then be estimated by the gradient of the displacement.

Since tissues are heterogeneous, applied stresses and responses (displacement and strain) vary spatially ( $\mathbf{x}$ ) and temporally. If a weak arbitrary force is applied to the surface of a medium, it produces infinitesimal spatially varying stresses that induce infinitesimal spatially varying strains that reflect the material properties of the media. Material properties are elements of a fourth-order tensor which can be significantly simplified assuming isotropy to yield properties that describe volume and shape changes over time due to the applied stimulus. Shape changes are reflected in the shear modulus  $G(t)$  or compliance  $J(t)$  and volume changes in bulk modulus  $K(t)$  or compliance  $B(t)$ . These are the fundamental properties when the tissue is deformed.

A typical static breast-imaging experiment involves compressing the tissue using the ultrasound transducer in the direction of the sound beam axis against the chest wall. Other boundaries are free to move. Over a small tissue volume below the transducer, the medium expands in directions perpendicular to the axis of compression. Stress and strain can then be described using ideal uniaxial compression. Under these ideal conditions, only stress along the beam axis is present. If displacement or strain is estimated using ultrasound along the same direction, estimates are very precise since echoes are most sensitive to object movements due to the phase-sensitivity of ultrasound in that direction. With this geometry, only derived material constants such as Elastic moduli  $E(t)$  or compliance  $D(t)$  can be measured. These are combination of shear and bulk features. In particular  $D(t) = \frac{1}{9}B(t) + \frac{1}{3}J(t)$ . Assuming tissue incompressibility, bulk compliance approaches zero and shear compliance is the fundamental material property measured with this experiment.

We now examine modulus from a slightly different experiment. When an ultrasound wave travels through the body, a force is applied along one spatial axis causing a deformation in the same direction without expanding or contracting the medium perpendicular to the direction of force. Particles only move just a few nanometers in the direction of passing ultrasound wave when low power is used. On the other hand, tissue displacements from an external compression are much larger and in all directions. Stress and strain generated with wave propagation is governed by a wave modulus given by  $M(t) = K(t) + \frac{4}{3}G(t)$ , again a combination of bulk and shear properties. If incompressibility of tissue is assumed, bulk features dominate shear and hence bulk properties primarily determine wave propagation and scattering in tissues.

Thus, time varying shear features of a medium govern contrast mechanisms for viscoelastic imaging and bulk features govern ultrasonic imaging. Independence of these two properties are important if we use ultrasound to track material properties else applied forces would alter wave properties and ultrasonic echo signals could not be used to accurately track motion.

## **1.6 Imaging mechanical properties using Ultrasound**

In the following section, we briefly review other techniques that exist in the literature for measuring mechanical properties using ultrasound. Note that development in this area is heavily focused on the instrumentation and detection of mechanical properties; with lit-

the exploitation of ECM changes during cancer progression or mechanisms responsible for viscoelastic behavior. In general, measurements of mechanical properties are collectively known as elasticity imaging. They are categorized based on the nature and location of the stimulus as external or internal techniques that apply static or dynamic excitations. External methods apply the stimulus on the surface of the tissue where as internal techniques either use ultrasound generated radiation force or use the natural artery pulsatory pressures [25]. Static stimuli can involve a simple compression or an impulse force where as dynamic stimuli involve vibrations (Hz-KHz) to generate shear waves which are subsequently tracked to reflect mechanical properties.

In a typical external static experiment, the transducer surface compresses the medium surface in the direction of the sound beam while allowing other boundaries to move. As discussed previously, the elastic modulus or compliance are the material properties for this experiment. However, to infer a spatially varying modulus distribution for heterogeneous media, knowledge of spatially varying stress and strain are required. The strain field can be accurately mapped out with ultrasonic techniques (Sec. 1.8.2) but the stress field is normally unknown and could vary especially around boundaries. Some investigators use complicated reconstruction techniques for stress determination [26], but information increase is normally modest when compared to computation time. Others [27], just use the high-resolution strain maps to interpret stiffness once observers are trained to visualize patterns and associated artifacts.

In dynamic methods, equations of motion [5] are used to describe the relationships

between material properties and displacements measured during shear wave propagation. For this experiment, shear modulus is the material property when linearity, isotropy, incompressibility and local homogeneity are assumed. Shear moduli are complex quantities, with the imaginary parts representing attenuation or losses in a viscoelastic medium. For harmonic motion, and no losses, the shear modulus is directly related to shear wave speed;  $C_s = \sqrt{(G/\rho)}$ , where  $C_s$  is the shear wave speed,  $G$  is the shear modulus and  $\rho$  is the density of the medium. Normally, wave speed and attenuation in soft tissues are normally functions of excitation frequency. Again assumptions of local homogeneity implies inaccurate results near region boundaries. These can be improved by using internal methods that use radiation force to produce very localized motion resulting in equations that can be solved ignoring boundaries.

We now briefly review techniques of elasticity imaging.

### 1.6.1 External methods

Ophir *et. al* [28] developed a method called elastography and used external compression methods under static conditions to form strain/elasticity images using a correlation algorithm, by tracking tissue displacements from pre-and post-compression echo signals. Only elastic properties were measured with this deformation. Using this method, many in-vivo studies on the breast and prostate have been reported [29]. Groups like Hall *et. al.* [30] use these external techniques for in-vivo measurements and have worked extensively with developing real-time algorithms for differentiating breast masses. For the population

of palpable breast masses they explored, they show that images of fibroadenomas present with low contrast when compared to that of high contrast invasive ductal carcinomas when the tissue was pre-compressed to a large extent before further compression. They use the width or area of the lesion as a discriminant marker in addition to contrast for lesion classification [31]. The above studies were done on palpable masses and other factors that affect classification like the changing tumor microenvironment, age, etc. were not investigated. Nitta *et.al* [32] on the other hand combined loading (compression) and unloading to quantify viscoelastic properties by using the area under the hysteresis loop of stress strain curves. Strain and displacement were estimated in real-time using a combined autocorrelation method. Their results showed that breast tissue displayed large hysteresis.

Parker *et. al* [33], [34] used dynamic methods and externally vibrated tissues to generate low-amplitude and low-frequency ( $<0.1$  mm and  $<1000$  Hz) shear waves, and detected resultant displacements using Doppler ultrasound. Their results indicated that lesion detectability increased with vibration frequency; however, lossy mechanisms in tissue ultimately limited the penetration of high frequency shear waves (KHz). Difficulties with such methods are the dependence of the result on the vibration frequency. Sandrin *et.al.* developed transient elastography [35] techniques based on plane shear waves to quantify viscoelastic properties. They used an ultra-fast ultrasonic scanner at a rate of 5000 frames/s (100 times higher than conventional scanners) to detect fast tissue motion induced by low frequency shear waves generated by low frequency (50-500 Hz) vibrations. The amplitude and phase of the propagating shear wave as a function of distance was fit to a linear model

to give the shear wave speed and its attenuation respectively to reflect shear modulus. With high viscous mediums such as the breast, shear wave velocity changes depending on the frequency of vibration. These dispersive properties can reflect the viscous characteristics of the medium. In the above method, viscoelastic properties can be detected to a very sensitive degree but elaborate instrumentation and algorithms were required to estimate properties with special adaptations required for non-planar waves often seen in breast tissue.

### **1.6.2 Internal methods**

There are several approaches to producing tissue motion using internal vibration by either using natural or radiation forces. Acoustic radiation force is a phenomenon associated with the propagation of acoustic waves through a dissipative medium. It is caused by a transfer of momentum from the wave to the medium, arising either from absorption or reflection of the wave [36]. One of the first static methods with radiation force was proposed by Sugimoto *et. al.* [37] where they used radiation force of ultrasound to make a minute deformation in the tissue and measured the transient recoil using Doppler ultrasound to evaluate tissue elastic properties. Other groups induced shear waves using radiation force. In a method called shear-wave elasticity imaging (SEWI) [38] (Sarvazyan *et. al.*), an ultrasound beam amplitude-modulated was used to induce a localized radiation stress inside the soft tissue resulting in shear wave oscillations. Since these waves travel at a very low speed, typically around few meters per second [4], and are also highly attenuated in soft tissue, it was possible to induce them in a very limited region hence avoiding the influence

of tissue boundaries. One drawback of this method was that the pulsed ultrasound exerted a radiation stress on all tissue through which it propagated. Furthermore, in-vivo feasibility of this method was low since ultrasound doppler was used for detection which required higher peak intensities close to or violating FDA regulations for intensity of the ultrasound beam. Another shear wave imaging method developed by Bercoff *et.al.* [39] called super-sonic shear imaging (SSI), provided quantitative shear modulus mapping of an organ in less than 30 ms by the use of a super sonic shear source to create a quasi-plane shear wave using an ultra-fast, ultrasonic scanner (5000 frames/sec). Implementation of this technique required elaborate and expensive instrumentation and was associated with extremely large data sets.

Greenleaf *et.al.* developed a technique called Vibro-acoustography [40]. They produced a map of the mechanical response of an object to a dynamic radiation force applied at each point. A dynamic radiation force was produced by focussing continuous-wave ultrasound beams at slightly different frequencies traveling along different paths. The interference between the two beams produced a radiation force oscillating at the difference frequency. The object vibrated, resulting in an acoustic radiation field that was detected by a sensitive hydrophone and is used to form an image of the object. Vibro-acoustic spectrograms [41] could also be produced if the difference frequency was swept over a range of frequencies. The acoustic emission at each frequency was plot to reflect the resonance peak of the medium [42]. Vibro-acoustography has been primarily tested on ex-vivo tissue and phantom data. In-vivo feasibility requires strict FDA adherence due to continuous wave ul-

trasound. Furthermore, since it uses a hydrophone for detection, it requires an acoustically quiet environment for proper detection.

Newer methods with radiation force developed by Nightingale *et.al* [43] (Acoustic Radiation Force Imaging: ARFI) and Walker *et.al*, [44] applied radiation force and tracked resulting displacements using correlation methods. They measured maximum tissue displacements of about 15 microns and recorded tissue recovery for less than 2 ms observing smaller displacements, higher time to peak and slower recovery for stiffer regions in tissues. Possible disadvantages with this technique is tissue heating due to high acoustic intensities applied especially if fine spatial resolution is required. Though the authors have shown that these values do not violate clinical FDA limits, this issue would ultimately limit the use of this technique in-vivo especially if used for routine diagnostic purposes.

Thus, there exists a number of ways to measure mechanical properties by engaging a response in tissue to a mechanical stimulus. External methods are quite elegant and easy to apply, could be readily clinically applicable, but may have problems generating enough force for deep-lying tissues. Furthermore they are affected by local boundaries. Internal methods like radiation force are very localized, not affected by boundaries, and are useful when the tissue is very deep or enclosed in a hard shell. However, it is limited to measuring very small displacements and can produce tissue or transducer heating especially if fine spatial resolution is needed.

## 1.7 Specific Aims

Our overall goal is to increase cancer specific diagnostic information by imaging mechanical/viscoelastic features of the stroma without contrast enhancement, safely, and at low cost using the unique capabilities of ultrasound. We wish to image micro-environmental responses (eg. Desmoplasia, Edema) of cancer signaling to describe important features of malignant breast disease. Our approach is to use an external quasi-static stimulus resembling a step function and track deformation using ultrasound with frequencies between 8-20 MHz (primarily due to its stromal specificity, depth of penetration and spatial resolution) to reflect time varying shear or elastic features of a medium. We use this type of stimulus due to its simplicity of application, potential in-vivo applicability and its ability to engage a broadband response enabling understanding of viscoelastic mechanisms.

Specific aims of this dissertation are: -

- Describe a medium's response to a quasi-static stimulus using parameters that reflect underlying mechanisms and microstructure.
- Validate parameters obtained with this stimulus using other measurements with known geometries.
- Quantify the sources of interference and uncertainty that alter contrast and parameter estimates.
- Establish in-vivo feasibility and develop acquisition methodology for in-vivo imaging on volunteers and patients.

## 1.8 Strategy for Viscoelastic Imaging

As a first step we choose to use hydro-polymers made from gelatin as a physical model for breast tissue to develop the required imaging science for quasi-static stimuli. Protocols established with polymers will then guide future in-vivo experiments. No animal models are used in evaluating the imaging science, reason being that the microstructure of tumors in mouse models is significantly different from breast cancers. They have homogeneous cell populations, develop quickly and with little desmoplasia while human breast cancers are usually heterogeneous, develop slowly over years and often with desmoplastic responses [12]. Since we are most interested in the stromal responses, we evaluate the technique directly on human volunteers and a small population of cancer patients.

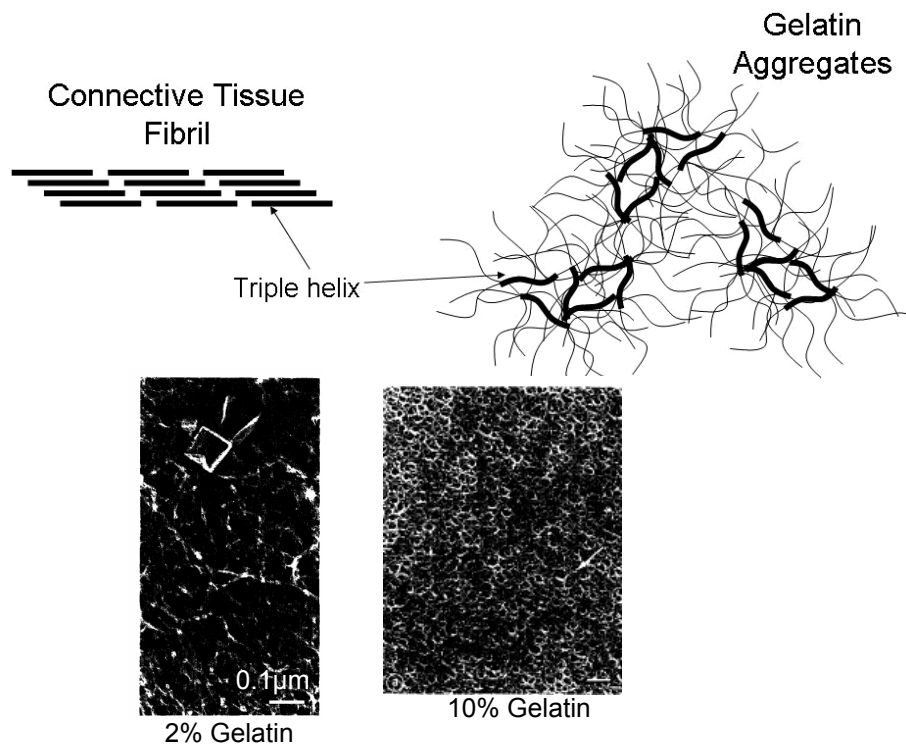
### 1.8.1 Gelatin hydro-polymers as physical models

Fibrous collagen networks are the major elements that provide mechanical integrity to tissues like the breast stroma. Hydro-polymers, such as gelatin, are obtained by hydrolytic degradation of collagen and derive from its fundamental molecular unit, a triple helical structure and the tropocollagen rod. Gelatin gels have lower material strength than the connective tissues from which they derive because the collagen is denatured. Chemical and thermal stresses that break down the natural type I collagen super structure during processing is only partially reconstituted during gelation and with many fewer covalent bonds [45]. While fragments of the original triple  $\alpha$ -helix structure reform, most of the protein molecules remain as peptide chains that are randomly tangled among the sparse helical

fragments [46], [47]. The molecular weight of the protein molecules is generally above 125 kDa, suggesting a matrix of relatively long and interconnected peptide chains. Unlike natural connective tissue collagen, there is no polysaccharide gel surrounding these chains [10]. At room temperature and pressure, gelatin gels are lightly cross-linked amorphous polymers surrounded by layers of structured water. The supermolecular assembly of gelatin is stabilized mainly through hydrogen bonds. Yet there are many reactive ionic groups exposed that adsorb water molecules. The peptide structure and molecular surface charges determine the viscoelastic behavior; consequently, the properties vary with pH, molecular weight, salt concentration, thermal and mechanical histories [48]. Unlike stromal collagen, gelatin is soluble in aqueous solutions at 37°C. However, its mechanical and thermal stability can be improved by chemical cross-linking of the side chain groups with aldehyde groups of cross-linkers like formaldehyde. This chemical cross-linking with formaldehyde increases the stiffness a little at first (1 day) but significantly over time [49]. The stiffness can also be altered by increasing the concentration of gelatin during the manufacturing process, because of the increased number of cross-links formed [50, 48].

Thus we choose gelatin gels over matrigels or other tissue constructs since they are simple to construct, are elastically uniform within the resolution of the ultrasonic imaging system, manifest essential tissue-like material features, They also have an extensive literature of mechanical measurements [51, 52, 53, 54, 46, 55, 56] and have been extensively characterized for ultrasonic systems [57, 58]. Fig 1.7 shows a gelatin aggregate (electron microscopy image [55] and cartoon) and a collagen fibril structure. As seen in the mi-

croscopy images, most units of gelatin are in peptide form entangled with each other in a random manner.



Reproduced from Djabourov et. al.

Figure 1.7: (a) Illustration of the structure of collagen fibrils in connective tissue (b) Illustration of gelatin aggregates (c) Electron microscopy images of gelatin at 2 levels of concentration.

Thus the gelatin gels chosen as the media for testing are deformed using a quasi-static stimulus. Ultrasonic data acquired during stimulus application is converted into displacement and strain using techniques described below.

## 1.8.2 Algorithms for Displacement Estimation for Viscoelastic Imaging

The backbone structure from two lab-developed algorithms [27, 59] that determine the displacement field using correlation based methods and regularized optical flow are used in this dissertation. These algorithms focus on estimating elastic strain between a pair of RF echo frames. Modifications have been made to these for adaptation for viscoelastic imaging. We briefly review the backbone structure of these two methods below.

**Multi-resolution cross correlation [27, 60]:** In this method, companding (joint operations of compressing and expanding echo fields) is used prior to cross-correlation, to compensate for scaling and shifting of scatterers in the scan plane to improve the precision of correlation-based measurements for displacement detection. Displacements are first estimated in a global companding (GC) process followed by local companding (LC) and 1-D cross correlation. A block matching (Sum-Absolute-Difference (SAD)) routine is implemented on the data before and after compression using non-overlapping large kernels. The companding and shift parameters estimated is then used to scale and shift the uncompressed echo frame, such that the data of the uncompressed tissue closely matches the data of the compressed tissue. Local companding involves a similar process but with a larger number of overlapping kernels smaller in size, for block matching. The estimated displacements are interpolated in 2-D to get a continuous displacement field and is used to deform the pre-compressed frame locally. Axial residual displacements are detected with 1-D cross correlation using a small correlation window function. The total displacement for each

step is then summed and the axial gradient in the direction of the beam is taken to obtain strain images.

Cross-correlation is a very accurate and effective estimator of distance (or similarity) between echo fields. It is capable of tracking small variations even when very low strains are involved and is robust to noise. However, strain is subjected to ultrasonic speckle decorrelation induced by out-of-plane motion, non-uniform motion of sub-resolution scatterers, non-uniformity of the ultrasound field and non-rigid tissue deformation [59] leading to loss of echo signal coherence and displacement estimation errors.

**Regularized Optical Flow [59]:** A regularized algorithm was developed to reduce decorrelation noise on the basis that data alone can be insufficient to solve ambiguities due to loss of echo coherence. The approach integrates a priori knowledge into the motion estimation process by regularization. An energy function, which reflects the constraints of conservation of echo amplitude and smoothness of the displacement field, is minimized to find the most probable value of the field. Regularization is achieved by minimizing local variations in the displacement field.

## 1.9 Scope and Outline

The scope of this dissertation is to develop new viscoelastic imaging techniques using ultrasound that are relatively simple, safe, in-vivo feasible, and such that estimated mechanical parameters reflect the under-lying microstructure and mechanisms. Imaging

science and mechanical testing is performed on gelatin hydropolymers and in-vivo volunteer and patient breast tissue. No animal models have been used for testing. Chapter 2 describes analytical methods from linear viscoelastic theory as applied to gelatin hydropolymers for the purpose of formulating approaches to molecular-scale interpretations of the viscoelastic response. Chapter 2 is a manuscript accepted for publication at the American Society of Mechanical Engineers (ASME) - Journal of Biomechanical Engineering. Measurements made under different geometries are compared and limitations of linking viscoelastic parameters are explored. Guidelines established in Chapter 2 are the basis for imaging experiments in Chapter 3 all investigated for hydropolymers. Chapter 3 explores measurement aspects related to viscoelastic parameter selection and error analysis and investigates the importance of certain imaging parameters such as data acquisition time, stimulus noise, and other interferences that influence parameters and image contrast. Chapter 3 is a manuscript under review in the Physics in Medicine and Biology journal. Imaging guidelines from Chapter 3 are used for in-vivo imaging of breast tissue for volunteers and a small pool of patients (Chapter 4) with specific comparisons with gelatin. Chapter 4 also addresses in-vivo applicability of the technique, confirmation of model assumptions, stimulus errors, new scanning techniques, characteristics of the viscoelastic response and data parameterization for molecular level understanding. Chapter 4 is a manuscript and will be submitted to a journal in edited form.

## **Chapter 2**

# **Viscoelastic Measurements on Gelatin**

## **Hydropolymers**

There exists several techniques for imaging spatiotemporal distributions of mechanical properties in biological tissues and engineered constructs on scales from molecules to organs. Collectively they are known as elasticity imaging. Diagnostic techniques employ phase-sensitive imaging modalities capable of tracking local tissue movements induced by a mechanical stimulus. The resulting image displays components of displacement or strain and sometimes a compliance or modulus. For example, ultrasonic and magnetic resonance (MR) techniques are frequently applied to breast tissues to image viscoelastic properties of tumors [61, 62, 63]. The principal advantage of elasticity imaging is the large object contrast for tissue stiffness [24] that occurs within stromal tissues in response to the advancing disease [12, 64]. Another large application area is vascular elasticity imaging us-

ing MR [65], optical [66], x-ray [67], and ultrasonic [68] methods. Emerging applications include viscoelastic imaging of macromolecules [69] and engineered tissue constructs [70]. The excitement about elasticity imaging is extending beyond diagnosis as we increase our understanding of the role of cellular mechanochemical transduction [71], particularly in cancer [12] and atherosclerosis [72].

Clinical elasticity imaging of breast cancer patients shows that malignant tumors most frequently appear as stiff regions (low strain or high modulus) compared to background media [73, 74]. Stiffening is common because of edema, cellular hyperplasia, and characteristic increases in stromal collagen concentration and cross linking. However, cancers can also appear softer than the background tissue [75] because the magnitude, spatial homogeneity and temporal variation of the strain response depend on the physiology [23] and tumor microenvironment [64] of a specific patient. In addition, images of viscoelastic features show both lower [76] and higher [62, 63] resonance times for malignant masses as compared to benign masses. Although electron microscopy data show changes in the connective tissue ultrastructure [15] that suggest lower viscosity, not enough is known about the viscoelastic behavior of breast tissues *in vivo* to determine if the diversity of findings are due to patient or experimental variabilities. To advance diagnostic applications, we must discover how disease-related changes to molecular bonding within stromal tissues affect the broad spectrum of viscoelastic responses. This is essentially the inverse problem of estimating structural features of polymers from measured mechanical properties.

This chapter reviews classical linear theory for polymers undergoing standard mechan-

ical (quasi-static) stimuli in the context of ultrasonic strain imaging. We investigate the role of discrete rheological models (Voigt and Maxwell) that offer concise parametric summaries of viscoelastic behavior. Measurements of gelatin gels with different experimental geometries test the validity of model assumptions, show the consequences of violations, and define ultrasonic imaging parameters required for strain imaging. Gelatin shares a basic structure and many features of stromal breast tissues, and yet it is a simpler medium with adjustable mechanical properties. Therefore gelatin gels are excellent media for investigating the strengths and weaknesses of elasticity imaging. One long-term goal of elasticity imaging research is to interpret microstructural reorganization of connective tissues during cancer progression from the macroscopic deformation patterns in viscoelastic images. Our experience with gelatin provides a framework for future tissue investigations.

## **2.1 Methodology**

This section reviews constitutive equations for the experimental geometries used in this study, including strain imaging where stress and strain vary in space and time. Imaging techniques often apply stresses and measure time-varying strain patterns, therefore the discussion is focused on creep. Results from other geometries and stimuli allow comparisons for validating imaging techniques.

### 2.1.1 Constitutive Equation

Assume a small cubic volume of gelatin is centered at vector position  $\mathbf{x}$ . Applying a weak force to volume surfaces at time  $t = t_0$  produces infinitesimal stresses  $d\sigma_{ij}(\mathbf{x}, t')$ , where  $t' = (t - t_0)$ . These induce infinitesimal strains  $d\epsilon_{ij}(\mathbf{x}, t) = S_{ijkl}(\mathbf{x}, t - t') d\sigma_{kl}(\mathbf{x}, t')$  for  $t' > 0$ , where the material properties of the medium are elements of the fourth-order compliance tensor  $S_{ijkl}$ . In media with linear time-invariant material properties, strains histories can be superimposed [77, 78] to find

$$\epsilon_{ij}(\mathbf{x}, t) = \int_0^t dt' S_{ijkl}(\mathbf{x}, t - t') \frac{\partial \sigma_{kl}}{\partial t'}(\mathbf{x}, t'). \quad (2.1)$$

Eq (2.1) describes time-varying strain for volume elements within a linear viscoelastic medium, and thus it also describes the strain image of a deformed object.

Adopting the notation  $\tilde{\epsilon}(\mathbf{x}, s) = \mathcal{L}\epsilon(\mathbf{x}, t) = \int_0^\infty dt \exp(-st)\epsilon(\mathbf{x}, t)$  for the one-sided Laplace transform, Eq (2.1) becomes

$$\tilde{\epsilon}_{ij}(\mathbf{x}, s) = s\tilde{S}_{ijkl}(\mathbf{x}, s)\tilde{\sigma}_{kl}(\mathbf{x}, s). \quad (2.2)$$

Here  $s$  is a complex variable fundamental to the Laplace transform. For isotropic media,  $S$  can be expanded to give the generalized viscoelastic Hooke's law (cf. Eq (11.2-8) [79])

$$\tilde{\epsilon}_{ij}(\mathbf{x}, s) = \left( \frac{1}{9}s\tilde{B}(\mathbf{x}, s) - \frac{1}{6}s\tilde{J}(\mathbf{x}, s) \right) \tilde{\Sigma}(\mathbf{x}, s)\delta_{ij} + \frac{1}{2}s\tilde{J}(\mathbf{x}, s)\tilde{\sigma}_{ij}(\mathbf{x}, s), \quad (2.3)$$

where  $\tilde{\Sigma}(\mathbf{x}, s) = \tilde{\sigma}_{11}(\mathbf{x}, s) + \tilde{\sigma}_{22}(\mathbf{x}, s) + \tilde{\sigma}_{33}(\mathbf{x}, s)$  is the trace of the stress matrix and  $\delta_{ij}$  is the Kronecker delta.  $\tilde{B}(\mathbf{x}, s)$  is bulk compliance that describes volume changes in the medium and  $\tilde{J}(\mathbf{x}, s)$  is shear compliance that describes shape changes, both in the Laplace

domain. The subscripts  $kl, ij$  are interchangeable since the stress and strain tensors are the same size and have only 6 independent terms.

The task now is to formulate stress tensors for different measurement conditions and apply Eq (2.3) to predict strain. In this manner, the results of standard measurement techniques with known geometry can be compared to those of imaging experiments where the geometry is less well known.

### 2.1.2 Uniaxial Compressive Stress: Creep

Our imaging experiments involve application of a uniaxial compressive stress under free-slip boundary conditions. Ideally this experiment generates only one non-zero stress element,  $\tilde{\sigma}_{11}$ , and three normal strains, although  $\tilde{\epsilon}_{22} = \tilde{\epsilon}_{33}$  for isotropic materials. Solving Eq (2.3) for the strain tensor corresponding to the applied stress yields

$$\tilde{\epsilon}_{11}(\mathbf{x}, s) = \left( \frac{1}{9}s\tilde{B}(\mathbf{x}, s) + \frac{1}{3}s\tilde{J}(\mathbf{x}, s) \right) \tilde{\sigma}_{11}(\mathbf{x}, s). \quad (2.4)$$

For ultrasonic strain imaging, strain is estimated along the axis of the sound beam and in the direction of the applied force,  $x_1$ . Consequently,  $\tilde{\epsilon}_{11}$  in Eq (2.4) is often referred to as axial strain in imaging experiments [27]. Axial strain images are common because ultrasonic echoes are most sensitive to object movements along the phase-sensitive beam axis. In the following,  $\tilde{\epsilon}$  indicates  $\tilde{\epsilon}_{11}$  except where otherwise noted.

From one strain measurement, however, only the linear combination of shear and bulk compliances can be determined. Thus we study the measurable quantity *compressive com-*

pliance [79],  $\tilde{D}(\mathbf{x}, s) = (1/9)\tilde{B}(\mathbf{x}, s) + (1/3)\tilde{J}(\mathbf{x}, s)$ , where

$$\tilde{\epsilon}(\mathbf{x}, s) = s\tilde{D}(\mathbf{x}, s)\tilde{\sigma}_{11}(\mathbf{x}, s). \quad (2.5)$$

The literature on creep measurements in collagen [80] and gelatin gels [51, 52] provides guidance on modeling compliance. A generalized Voigt model is often useful [53, 79],

$$s\tilde{D}(\mathbf{x}, s) = D_0 + \sum_{\ell=1}^L \frac{D_\ell}{1 + sT_\ell} + \frac{1}{s\eta_0}. \quad (2.6)$$

Constants  $D_\ell$  are compressive creep compliances, and  $T_\ell$  are discrete retardation times that are proportional to viscosity coefficients  $\eta_\ell$  of the  $\ell$ th viscoelastic component:  $T_\ell = D_\ell \eta_\ell$ . If we can eliminate the last term in Eq (2.6) and let  $T_L$  be the largest time constant, the Fourier transform of compliance will exist because the region of convergence,  $s > -1/T_L$ , includes the imaginary axis. Eq (2.6) implies a time-independent elastic strain and  $L$  distinct viscoelastic strains that delay in time the full response. The last term describes the steady-state compressive-flow viscosity coefficient,  $\eta_0$ . In weakly compressed tissues,  $\eta_0$  may represent flow of vascular fluids; in hydrogels it represents movement of unbound water.

A constant uniaxial force  $\mathbf{F}_1$  is suddenly applied at  $t_0$  to a cubic sample of side-area  $A$  along the  $x_1$  axis. Then  $\sigma_{11}(\mathbf{x}, t) = \sigma_a(\mathbf{x})u(t - t_0)$ , where  $\sigma_a = F_1/A$  for the volume element located at  $\mathbf{x}$ , and the step function  $u(t - t_0)$  is zero for  $t < t_0$  and one for  $t \geq t_0$ . The Laplace transform of the step stress stimulus is

$$\tilde{\sigma}_{11}(\mathbf{x}, s) = \sigma_a(\mathbf{x})/s. \quad (2.7)$$

Combining Eqs (2.5) – (2.7) and taking the inverse Laplace transform yields for  $t > t_0$ ,

$$\epsilon(\mathbf{x}, t) = \epsilon_0(\mathbf{x}) + \sum_{\ell=1}^L \epsilon_{\ell}(\mathbf{x}) [1 - \exp(-(t - t_0)/T_{\ell}(\mathbf{x}))] + (t - t_0) \frac{\sigma_a(\mathbf{x})}{\eta_0(\mathbf{x})}, \quad (2.8)$$

where strain amplitudes  $\epsilon_{\ell} = \sigma_a D_{\ell}$  for  $0 \leq \ell \leq L$ . The strain response of the Voigt model to a step load in time has three components.

The initial elastic response occurs immediately after compression,  $\epsilon(\mathbf{x}, t_0+) \simeq \epsilon_0(\mathbf{x})$ , before the viscous mechanisms have time to engage. Purely elastic responses are implicitly assumed in “static” elastography techniques that ignore time-varying strain [27, 28, 81]. If  $\sigma_a(\mathbf{x}) = \sigma_a$  is constant throughout the volume, then the instantaneous elastic response is directly proportional to the compressive compliance  $D_0$  (and inversely proportional to the elastic modulus  $E_0$ ) in the volume element. Stresses in heterogeneous media, whose volume elements have unknown boundary conditions, vary unpredictably with position. Strain images in such media must be carefully interpreted to infer stiffness.

The second term defines the time-varying viscoelastic (VE) response,  $\epsilon_{VE}(\mathbf{x}, t) = \epsilon(\mathbf{x}, t) - \epsilon_0(\mathbf{x}) - (t - t_0)\sigma_a(\mathbf{x})/\eta_0(\mathbf{x})$ . In solids, strain builds exponentially over time with rate constants  $T_{\ell}$  until the total strain reaches the steady-state value  $\sum_{\ell=0}^L \epsilon_{\ell}(\mathbf{x})$  at  $t \gg T_L(\mathbf{x})$ . Measurable viscoelastic responses are from breakage and reformation of weak molecular bonds, release of polymer filament entanglements [53], and other internal restructuring.

The third term in Eq (2.8), which varies linearly in time, describes viscous flow within the polymer; e.g., curve a in Fig 2.1a. If time-varying strain plateaus (curve b), the polymer behaves as a solid. VE solids are modeled with Eq (2.8) by setting the last term to zero.

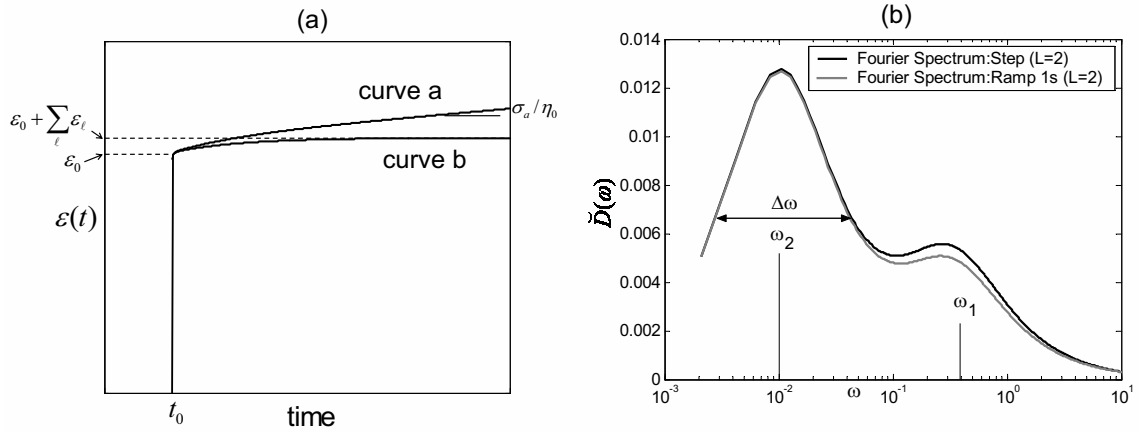


Figure 2.1: (a) Creep curves for a second-order ( $L = 2$ ) Voigt model and a step stress stimulus are illustrated. Curve a is drawn directly from Eq (2.8) with finite  $\eta_0$ ; its slope at  $t \gg T_2$  is  $\sigma_a/\eta_0$ . Curve b is from the same equation where  $\eta_0 = \infty$ . In both cases  $\epsilon_2/\epsilon_1 = 2.5$ ,  $T_1 = 3$  s, and  $T_2 = 100$  s. (b) The corresponding Fourier spectra,  $\check{D}(\omega)$ , are from Eq (2.10). Spectra from a step and 1 s ramp stress stimulus are compared.

Model parameters  $D_\ell$ ,  $T_\ell$  and  $\eta_0$  that vary spatially are candidate parameters for diagnostic imaging. Because  $\sigma_a(\mathbf{x})$  is unknown in practice, we study  $\epsilon_\ell = D_\ell \sigma_a$  in place of  $D_\ell$ .

Ultimately, the value of  $\epsilon_\ell$ ,  $T_\ell$ , and  $\eta_0$  as diagnostic imaging features depends on their sensitivity and specificity to disease-related changes in tissue structure and biochemistry [64]. The discrete compliance model of Eq (2.6) is attractive because it offers a testable number of parameters that may be interpreted in terms of polymer structure. Fung [77] and others warn against determining the order of the model by blindly fitting model functions to data. The retardation spectrum [53, 82] described below provides another tool for estimating retardance time distributions.

First, we examine the Fourier spectrum of the VE creep response in two ways. One describes the spectrum of the creep *measurement*  $\check{\epsilon}_{VE}(\omega)$  to determine sampling requirements. Strain is sampled in time at the frame rate of the ultrasound system. Another

describes the frequency spectrum of the *medium response*  $\check{D}(\omega)$ .

*Fourier Spectra:* The Fourier transform of the VE response to a uniaxial step stress may be found from the Laplace domain representation of Eqs (2.5) – (2.7) by substituting  $s = i\omega$ ,

$$\tilde{\epsilon}_{VE}(\omega) = \frac{1}{i\omega} \sum_{\ell=1}^L \epsilon_{\ell} \left( \frac{1 - i\omega T_{\ell}}{1 + \omega^2 T_{\ell}^2} \right). \quad (2.9)$$

$\omega$  is angular temporal frequency in rad/sec and  $i = \sqrt{-1}$ . If  $T_1$  is the smallest time constant, then the  $\ell = 1$  term determines the highest frequency in the response bandwidth. The frequency spectrum of this creep component is  $|\tilde{\epsilon}_{VE}(\omega)| = \epsilon_1 / (\omega \sqrt{1 + \omega^2 T_1^2}) \rightarrow \epsilon_1 / \omega^2 T_1$  for  $\omega \gg 1/T_1$ . The measurement spectrum decreases monotonically as  $\omega^{-2}$  and thus is bandlimited.

Of great interest is the frequency spectrum of material properties, specifically the loss spectrum for compressive compliance  $\check{D}(\omega)$  [79]. From Eqs (2.5) and (2.6),

$$\check{D}(\omega) \triangleq \omega \tilde{D}(\omega) = -\mathcal{I} \left. \frac{s \tilde{\epsilon}_{VE}(s)}{\sigma_a} \right|_{s=i\omega} = \sum_{\ell=1}^L \frac{D_{\ell} \omega T_{\ell}}{1 + \omega^2 T_{\ell}^2}, \quad (2.10)$$

where  $\mathcal{I}$  is the imaginary part of what follows. The procedure for estimating  $\check{D}(\omega)$  from creep data begins by eliminating the elastic and steady-state viscous terms to find  $\epsilon_{VE}(t)$ . We then multiply by a Shepp-Logan-type high-pass filter [83] and then compute the Fourier transform, which yields a stable estimate of  $s \tilde{\epsilon}_{VE}(s)|_{s=i\omega}$  in the presence of noise. The loss compliance spectrum for a second-order Voigt model is displayed on a semi-log plot in Fig 2.1b. Curve parameters are given in the caption.

Fig 2.1b shows the Nyquist frequency to be  $f_N = \omega_N / 2\pi \simeq 1.5$  Hz, requiring a frame rate of at least 3 Hz to faithfully record creep with  $T_{\ell} \geq 3$  s. To visualize the lowest fre-

quency peak at  $\omega_2$  in this example, corresponding to  $T_2 = 100$  s, the acquisition time should be  $(2\pi)/\omega_2 > 628$  s, preferably longer. Acquiring data for shorter times truncates the spectrum at low frequencies without distorting higher frequency values, but creates difficulties in determining model order from data as described below. In-vivo breast imaging techniques allow patient acquisition times between 20 s and 200 s. Acquisitions in hydrogel samples are often on the order of 2500 s.

The two peaks in the frequency spectrum arise from  $L = 2$  roots (non-zero poles of Eq (2.6)) at  $s = -1/T_\ell$ ; both are real and negative. They correspond to spectral peaks at  $\omega_\ell = 1/T_\ell$ , [84], of height  $D_\ell/2$ , and -6 dB peak width  $\Delta\omega_\ell = 2\sqrt{3}/T_\ell$ . The latter property shows that  $T_\ell$  must be widely separated to resolve their peaks on the frequency axis. The pole at  $s = 0$  from the steady-state viscosity term must be eliminated for the Fourier transform to exist. Poles of the model uniquely determine the time-varying properties of the material.

*Retardation Spectra:* It is attractive to adopt a discrete model for compliance, e.g., Eq (2.6). Low-order models with few components that correspond to specific structural and biochemical features yield the diagnostic imaging parameters we seek. However, data from tissues [77] and gels [53] suggest broad continuous distributions of retardance times  $\tau$ . Schwarzl and Staverman [82] proposed a technique for estimating continuous spectra  $L(\tau)$  from creep data. To facilitate direct comparisons with Fourier spectra, we plot  $\tilde{L}(\omega) = L(\tau)|_{\omega=1/\tau}$ . The two forms of  $L$  are reflections of each other about the ordinate followed by a translation along the logarithmic abscissa.

$L(\tau)$  is introduced by considering the Laplace transform of Eq (2.8) for a step stress stimulus and a continuous distribution of compliance.

$$\tilde{D}(\mathbf{x}, s) = \frac{D_0(\mathbf{x})}{s} + \int_0^\infty d\tau \frac{D_s(\mathbf{x}, \tau)}{s(1+s\tau)} + \frac{1}{s^2\eta_0(\mathbf{x})}. \quad (2.11)$$

Where,  $D_s(\mathbf{x}, \tau)$  is the sampled compliance function obtained when the discrete sum is converted into an integral as shown in [85]. Substituting  $L(\tau) = \tau D_s(\tau)$  and noting that  $d \ln \tau = d\tau/\tau$  and  $\tau = \tau(\mathbf{x})$ , the inverse Laplace transform of Eq (2.11) for  $t > t_0$  is

$$D(\mathbf{x}, t) = D_0(\mathbf{x}) + \int_{-\infty}^\infty d \ln \tau L(\mathbf{x}, \tau) [1 - \exp(-(t - t_0)/\tau)] + \frac{(t - t_0)}{\eta_0(\mathbf{x})}. \quad (2.12)$$

A method for estimating  $L$  from creep compliance estimates  $\hat{D}_{VE}$  was described by Tschoegl [79]:

$$L(\mathbf{x}, \tau) = \lim_{k \rightarrow \infty} \frac{(-1)^{k-1}}{(k-1)!} \mathcal{D}_t^{(k)} \hat{D}_{VE}(\mathbf{x}, t) \Big|_{t=k\tau}. \quad (2.13)$$

$\mathcal{D}_t^{(k)} = \mathcal{D}_t(\mathcal{D}_t - 1)(\mathcal{D}_t - 2) \dots (\mathcal{D}_t - k + 1)$  is a factorial-like derivative and  $\mathcal{D}_t = d/d \ln t$  is the derivative operator. The first and second order approximations are

$$\begin{aligned} L^{(1)}(\mathbf{x}, \tau) &= \frac{d}{d \ln t} \hat{D}_{VE}(\mathbf{x}, t) \Big|_{t=\tau} \\ L^{(2)}(\mathbf{x}, \tau) &= \left[ \frac{d}{d \ln t} \hat{D}_{VE}(\mathbf{x}, t) - \frac{d^2}{d(\ln t)^2} \hat{D}_{VE}(\mathbf{x}, t) \right] \Big|_{t=2\tau}. \end{aligned} \quad (2.14)$$

The  $k$ -th-order estimate  $L^{(k)}(\tau)$  is found by first filtering creep data with a low-pass polynomial filter using Matlab 7<sup>©</sup>. Specifically  $\mathbf{P}(:, j) = \text{polyfit}(\log(t), \mathbf{y}, N(j))$ , where  $\mathbf{P}$  is a  $(N + 1) \times 12$  matrix of polynomial coefficients and  $\mathbf{y} \triangleq \hat{D}_{VE}(\mathbf{x}, n\Delta t)$  time samples. As the polynomial order is increased from  $4 \leq N(j) \leq 15$ , the frequency response of the  $j$ th filter is plotted from the magnitude of the function  $\text{freqz}(\mathbf{P}(:, j), Z)$ ,

where  $Z$  is a vector of ones. The lowest-order filter spectrum maximally flat in the stop band and with a smooth transition region is selected by visual inspection to represent the data. Filter order depends on the bandwidth of the VE response: short duration time constants require higher order polynomial filters. The derivatives of Eq (2.13) are computed analytically from the polynomial representation.

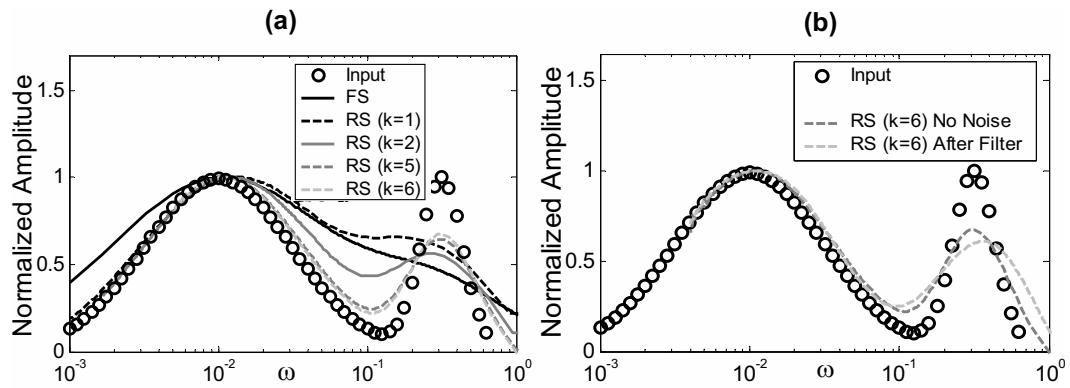


Figure 2.2: (a) Retardation spectra from simulated data. Plotted are  $\tilde{L}(\omega) = L(\tau)|_{\tau=1/\omega}$  for comparison with the Fourier spectrum. Creep data were generated from Eq (2.12) for  $\epsilon_0 = \sigma_a/\eta_0 = 0$  assuming a broadband, bi-modal input as given by the circle points (Input). Estimated retardation spectra (RS),  $\tilde{L}^{(k)}(\omega)$  for  $k = 1, 2, 5, 6$ , are compared to the Fourier spectrum (FS),  $\check{D}(\omega)$ , computed from the same data. (b)  $\tilde{L}^{(6)}$  estimates without noise in the creep data and with noise (signal-to-noise ratio = 32.2 dB). An 9-th order polynomial filter was applied to the noisy data before estimation.

To develop stopping rules for selecting  $k$  in Eq (2.13), we generated noiseless creep data assuming a log-normal input distribution of retardance times [79]. The input function  $\tilde{L}(\omega)$  is represented by the open circles in Fig 2.2. Clearly it is difficult to describe the input distribution of  $\tau$  from its Fourier spectrum  $\check{D}(\omega)$  of Fig 2.2a even though the ratio of peak frequencies is 30. Conversely, retardation spectral estimates approach the input distribution as  $k$  increases. Narrow distributions require large  $k$  values to minimize bias. However,

estimates become unstable as  $k$  increases, placing greater emphasis on filter design.

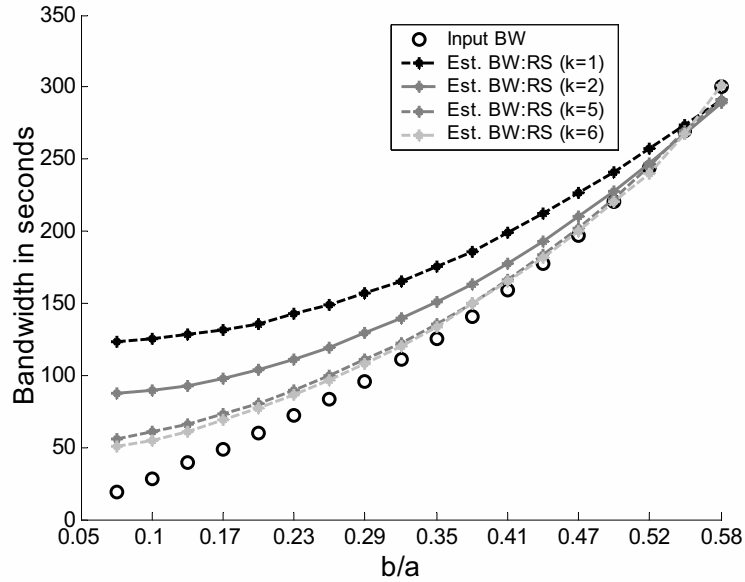


Figure 2.3: Limitation of  $L^{(k)}(\tau)$  for representing retardance time distributions. The abscissa is  $b/a$  from the log-normal input distribution  $L(\tau) = \exp(-(\ln \tau - a)^2/2b^2)$ . The ordinate is the full-width-at-half-maximum bandwidth of retardance spectral estimates. Circles denote the exact output bandwidth for the input distribution, while the curves are bandwidths for  $k$ th-order estimates using noiseless creep data. Results suggest that the  $L^{(6)}(\tau)$  represents bandwidths of log-normal distributions above 150 s with acceptable bias error.

The effects of measurement noise are shown in Fig 2.2b. Adding white Gaussian noise with signal-to-noise ratio 32.2 dB (typical of rheometer data described below) introduces bias particularly at high frequency. Fig 2.3 predicts the amount of bias introduced as the width of the log-normal input distribution increases. The data suggest that a 150 s bandwidth can be estimated with acceptable bias by a sixth-order estimate,  $L^{(6)}(\tau)$ .

### 2.1.3 Shear Stress and Strain

The unconfined boundaries of arbitrarily-shaped, heterogeneous media subjected to uniaxial stress stimuli in imaging experiments can violate the assumptions leading to Eq (2.3). To study the effects, we compare parameters from the carefully controlled geometry of standard rheometer measurements to those from creep imaging experiments. Our interest is with average properties, so the positional dependence is ignored for these non-imaging measurements.

The constitutive equation is calculated in the Laplace domain from Eq (2.3):

$$\tilde{\epsilon}_{12}(s) = \frac{1}{2} s \tilde{J}(s) \tilde{\sigma}_{12}(s) . \quad (2.15)$$

Bulk compliance terms are negligible in rotational shear measurements. For a step shear stress,  $\sigma_{12} = \sigma'_a u(t - t_0)$ , and assuming the Voigt model in shear, the observed creep in the time domain is

$$\gamma_{12}(t) = \gamma_{(12)0} + \sum_{m=1}^M \gamma_{(12)m} [1 - \exp(-(t - t_0)/T_m)] + (t - t_0) \frac{\sigma'_a}{\eta'_0} , \quad \text{for } t > t_0 . \quad (2.16)$$

Measurable shear creep is related to the corresponding strain tensor via  $\gamma_{12} = 2\epsilon_{12}$  [79]. Also  $\gamma_{(12)m} = \sigma'_a J_m$  for  $0 \leq m \leq M$  and  $\eta'_0$  is the steady-state shear-flow viscosity coefficient. To account for the geometry of the cone-plate viscometer, the ratio  $\gamma_{12}(t)/\sigma_{12}(t) = \lambda\varphi/\Gamma$ , where  $\varphi$  is the angular displacement,  $\Gamma$  is the applied torque, and  $\lambda = 2\pi R^3/3\phi$  is a geometric factor that depends on the radius of the cone,  $R = 30$  mm, and the angle between the cone and plate,  $\phi = 4^\circ$ .

Compression and shear measurements may be compared through Eqs (2.8) and (2.16).

Compressive and shear creep compliances are, respectively,

$$\begin{aligned} D(t) &= \epsilon_{11}/\sigma_a = D_0 + \sum_{\ell} D_{\ell}(1 - \exp(-t'/T_{\ell})) + t'/\eta_0 \\ J(t) &= \gamma_{12}/\sigma'_a = J_0 + \sum_m J_m(1 - \exp(-t'/T_m)) + t'/\eta'_0, \end{aligned} \quad (2.17)$$

for  $t' = t - t_0 > 0$ . From Eqs (2.4) and (2.5) we have  $D(t) = J(t)/3 + B(t)/9$ . Thus model parameters for the two experiments may be compared directly only for “incompressible media” where bulk compliance  $B(t)$  is negligible. Bulk compliance can be related to compressive compliance and Poisson’s ratio in the Laplace domain:  $s\tilde{B}(s) = 3s\tilde{D}(s)(1 - 2s\tilde{\nu}(s))$ , where  $s\tilde{\nu}(s) = -\tilde{\epsilon}_{22}(s)/\tilde{\epsilon}_{11}(s)$ . We can then use limit theorems [79] to find in the time domain  $B(\infty) = 3D(\infty)(1 - 2\nu(\infty))$  at  $s \rightarrow 0$  and  $B(0) = 3D(0)(1 - 2\nu(0))$  at  $s \rightarrow \infty$ .

## 2.1.4 Uniaxial Compressive Strain: Stress Relaxation and Relaxation Spectra

Stress relaxation experiments are conducted in which samples are stimulated with a uniaxial step strain while stress is measured over time. This non-imaging technique provides spectral data under confined boundary conditions that could not be obtained using creep measurements with our instruments.

Analogous to Eq (2.3), the generalized viscoelastic Hooke’s law for stress relaxation is [79]

$$\tilde{\sigma}_{ij}(s) = \left( s\tilde{K}(s) - \frac{2}{3}s\tilde{G}(s) \right) \tilde{\Delta}(s)\delta_{ij} + 2s\tilde{G}(s)\tilde{\epsilon}_{ij}(s), \quad (2.18)$$

where  $\tilde{\Delta}(s) = \tilde{\epsilon}_{11}(s) + \tilde{\epsilon}_{22}(s) + \tilde{\epsilon}_{33}(s)$ .  $\tilde{G}(s)$  and  $\tilde{K}(s)$  are shear and bulk moduli, respectively; they are analogous to the compliances  $\tilde{J}(s)$  and  $\tilde{B}(s)$  measured in creep. If the sample boundaries are confined in the manner described in Method B below, then there is only one nonzero strain tensor:

$$\tilde{\sigma}_{11}(s) = \left( s\tilde{K}(s) + \frac{4}{3}s\tilde{G}(s) \right) \tilde{\epsilon}_{11}(s) = s\tilde{M}(s)\tilde{\epsilon}_{11}(s). \quad (2.19)$$

Eq (2.19) relates the measurable compressive longitudinal wave modulus  $\tilde{M}$  for the confined sample to fundamental relaxation moduli  $\tilde{K}$  and  $\tilde{G}$  in the Laplace domain [79].

Alfrey's rules [79] describe how to select a Maxwell model for  $\tilde{M}(s)$  that is conjugate to the Voigt model of Eq (2.6):  $s\tilde{M}(s) = M_0 + \sum_n M_n sT_n/(1 + sT_n)$ . Applying a uniaxial step strain stimulus,  $\epsilon_{11}(t) = \epsilon_a u(t - t_0)$ , the time-varying wave modulus is

$$M(t) \triangleq \frac{\sigma_{11}(t)}{\epsilon_a} = M_0 + \sum_{n=1}^N M_n \exp(-t'/T_n) \quad \text{for } t' = t - t_0 > 0, \quad (2.20)$$

where  $T_n$  are discrete relaxation time constants. Unfortunately, it is not easy to relate  $T_n$  directly to retardance time constants  $T_\ell$  for this geometry.

If the sample boundaries are unconfined, all three strain tensors are nonzero. The axial stress tensor is

$$\tilde{\sigma}_{11}(s) = \frac{9s\tilde{K}(s)s\tilde{G}(s)}{3s\tilde{K}(s) + s\tilde{G}(s)} = s\tilde{E}(s)\tilde{\epsilon}_{11}(s). \quad (2.21)$$

Applying the same step strain stimulus, the compressive relaxation modulus is

$$E(t) \triangleq \frac{\sigma_{11}(t)}{\epsilon_a} = \sum_{r=1}^R E_r \exp(-t'/T_r) \quad \text{for } t' = t - t_0 > 0. \quad (2.22)$$

$E(t)$  may be compared to creep compliance  $D(t)$  in the Laplace domain by  $E(s)D(s) = s^{-2}$ . Alternatively  $\int_0^t E(\tau)D(t - \tau)d\tau = t$ , suggesting  $D(t)E(t) \leq 1$  [53]. When  $\nu \simeq 0.5$ ,

$D(t)E(t) \simeq 1 \simeq G(t)J(t)$ . From Eq (2.22), the elastic (Young's) modulus is defined as  $E_0 \triangleq \sigma_{11}(t_0)/\epsilon_a = \sum_r E_r$ .

Similar to the methods described in Section 2.1.2 for retardation spectra, relaxation spectra  $H(\tau)$  and  $\tilde{H}(\omega)$  may be estimated from stress relaxation data [53, 79].  $H(\tau)$  is the distribution of relaxation times that determines the time dependence of a modulus. For confined samples, a continuous distribution of relaxation times is modeled as  $\tilde{M}(s) = M_0/s + \int_{-\infty}^{\infty} d \ln \tau H_M(\tau) \tau / (1 + s\tau)$  [79], and similarly for  $H_E(\tau)$ . Depending on context,  $H(\tau)$  refers to either  $H_M$  or  $H_E$ .

### 2.1.5 Gelatin Model

The above set of measurement parameters was explored by selecting animal-hide gelatin hydrogels for experimentation. Gelatin gels have an extensive literature of mechanical measurements [51, 52, 53, 54, 46, 55, 56, 86], are simple to construct, are elastically uniform within the resolution of the ultrasonic imaging system, and manifest essential tissue-like material features.

At room temperature and pressure, gelatin gels are lightly cross-linked amorphous polymers surrounded by layers of structured water. Depending on the stress stimulus, the strain response can have both solid and fluidic features. The peptide structure and molecular surface charges determine the viscoelastic behavior; consequently, the properties vary with pH, salt concentration, thermal and mechanical histories. Gelatin gels have lower material strength than the connective tissues from which they derive because the collagen is dena-

tured. Chemical and thermal stresses that break down the natural type I collagen superstructure during processing is only partially reconstituted during gelation and with many fewer covalent bonds [45]. While fragments of the original triple  $\alpha$ -helix structure reform, most of the protein molecules remain as peptide chains that are randomly tangled among the sparse helical fragments. (See Fig 2.4 from [46].) The molecular weight of the protein molecules is generally above 125 kDa, suggesting a matrix of relatively long and interconnected peptide chains. Unlike natural connective tissue collagen, there is no polysaccharide gel surrounding these chains [10]. Yet there are many reactive ionic groups exposed that adsorb water molecules.

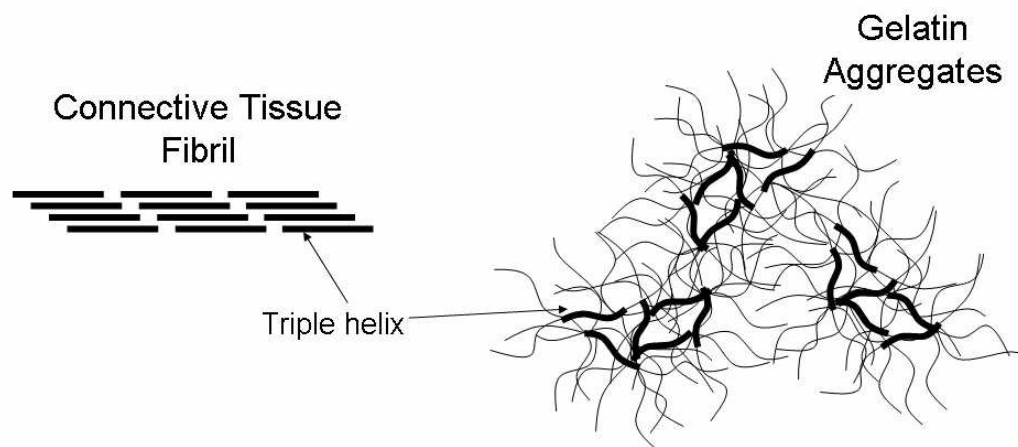


Figure 2.4: Illustration of collagen structures in connective tissue (fibril) and in gelatin (aggregates).

Desiccated gels retain about 10% water that is tightly bound to the charged residues. In this role, water forms stabilizing intramolecular hydrogen bonds [46]. Increasing hydration adds layers of water molecules more viscous than free water because of its polar attraction

to the charged protein backbone [87]. Near the highest hydration levels that still yield gels, structured water layers are added with increasingly weaker binding forces. The outermost layers remain bound under a load if the resistance to flow  $\eta_0$  is greater than the applied forces  $\sigma_a$ . From Eqs (2.8) and (2.16), gels may be considered VE solids when  $\sigma_a/\eta_0 \ll 1$  (curve b in Fig 2.1a). Otherwise they exhibit the viscous flow of rheodictic materials (curve a).

Gelation is initiated within molten gelatin near sites of the randomly located  $\alpha$ -helices [46]. When the temperature falls below about 30°C, polymerization is nucleated, and aggregates of hydrogen-bonded protein molecules form. Material strength increases with gelatin concentration because the aggregate bond density increases. Hydrogen bonds, which break and reform under a load, are a source of *viscoelastic creep*,  $\epsilon_{VE}(t)$ . The distribution of adhesive force strengths in the polymer determines the retardation spectrum. Covalent bonding among sparse helical fibrils [88] as well as the strong intra-molecular bonds both contribute to the initial *elastic response*,  $\epsilon_0$ . The covalent-bond density can be increased to stiffen gels by adding aldehydes [86]. Thus melting temperature is increased and temporal stability improved as is required for tissue-like imaging phantoms.

### 2.1.6 Gelatin Sample Preparation

To each 100 ml of deionized water we add 13 ml of n-propanol and 6.5 g (12.4 g) of 275-bloom, animal-hide gelatin (Fisher Scientific, Chicago, IL) to arrive at a 5.5% (10%) gelatin concentration. The solution is heated at 60°C until visually clear (~30 min) before adding

0.3 ml of formaldehyde (37% w/w). The hot solution is poured into a rigid container and quiescently cooled. Although gelatin congeals in hours, it continues to cross link for many days. Samples are stored at room temperature 1-5 days before conducting measurements. The elastic modulus  $E_0$  of gelatin is known to increase linearly with  $\log(\text{time})$  [57]. “Stiff” samples are 10% gelatin by weight and “soft” samples are 5.5% gelatin; both are above the critical gelation concentration [89]. Since  $E_0$  is proportional to the square of gelatin concentration [57, 89], 10% gels are roughly 3 times stiffer than the 5.5% gels.

Samples made for compression measurements are either 5 cm cubes or cylinders of diameter 15 mm and height 15 mm (via 10 cc syringes). Cubic gel samples are removed from the molds before measurement to free the boundaries from confinement. Cylindrical gel samples remain in the syringe as uniaxial compressions are applied under confined boundary conditions using the syringe piston. Shear measurements are made on samples formed in the rheometer as described in the next section. Indenter measurements are made near the axis of cylindrical samples of diameter 60 mm and height 6 mm that are removed from their containers.

Two types of commercially available gelatin are studied. Type A gelatin (pH 6) involves acid processing of collagen-rich media whereas Type B gelatin (pH 5) is obtained from alkaline processing. Type A preserves more of the natural collagen structure but contains impurities that affect mechanical properties. Type B gelatin is a purer form of collagen molecule, yet it undergoes greater denaturation so that fewer fibrils reform, and the reconstituted structure is less similar to native connective tissues.

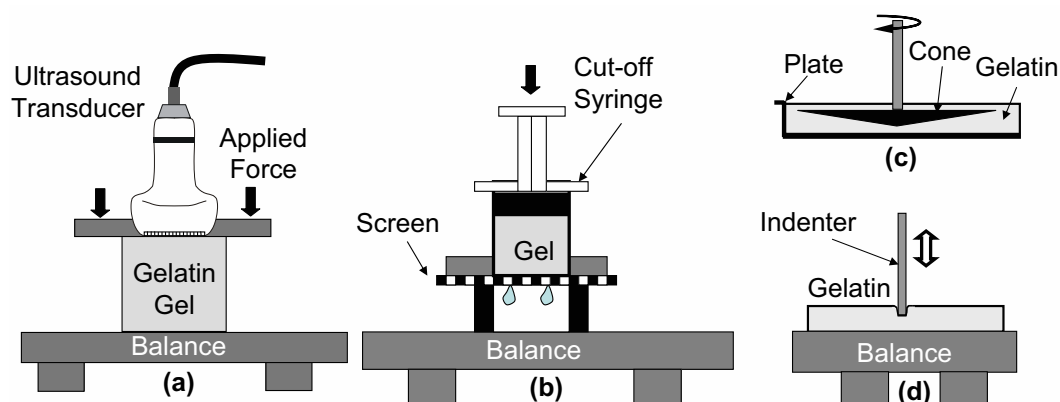


Figure 2.5: Illustrations of four viscoelastic experiments. (a) Measurement method A applies uniaxial stress or strain stimuli to unconfined gelatin samples to estimate compressive relaxation modulus  $E(t)$  or compressive creep compliance  $D(t)$ . It is also the ultrasonic strain imaging technique. (b) Method B applies uniaxial strain to estimate the compressive wave modulus  $M(t)$  for rigidly confined sample boundaries. (c) Method C is a cone-plate rheometer applied to estimate shear creep compliance  $J(t)$ . (d) Method D applies an indenter to gelatin samples to estimate the elastic modulus  $E_0$ . All positions are computer controlled with sub-micron accuracy, and forces are measured with a precision of 0.01 g.

### 2.1.7 Viscoelastic Measurement Techniques

All gelatin measurements are made at ambient room temperature and pressure.

*Method A – Uniaxial Compression in Unconfined Samples.* A flat plate compresses the top surface of a cubic gel sample downward as the sample rests on a digital force balance (Denver Instruments Co., Model TR-6101, Denver CO). See Fig 2.5a. A motion controller (Galil Inc., Rocklin CA) is programmed to apply a small preload to establish contact. Then a short-duration ( $\sim 1$  s) ramp stress is applied along the direction normal to the sample surface to initiate creep measurements. The final force is held constant over time by using the balance output as feedback. Sampling the balance output at 3.4 samples/s, the motion con-

troller adjusts the compressor position within  $0.1 \mu\text{m}$  so the applied force remains constant during the experiment as the sample creeps. The position of the compressor indicates displacement for creep estimates. The effects of the ramp stimulus relative to a step stimulus are discussed in Appendix A.

For a cubic sample of height  $h$ , we measure displacement  $\Delta h$  and force  $F$  [N] = mass [kg]  $\times 9.81$ . These quantities are converted to true stress  $(1 + \Delta h/h)F/A_0$  [Pa] and true strain  $\ln(1 + \Delta h/h)$ , where  $A_0$  is the unloaded sample area contacting the balance. Mineral oil is applied to all exposed sample surfaces to minimize desiccation and allow boundaries to freely slip under a load.

Several gelatin samples are constructed from each preparation. If a sample is used more than once to repeat an experiment, we follow the rule of resting samples more than twice the acquisition time of the previous experiment (Appendix B). A typical creep acquisition is 2500 s. Those samples are rested 2 hours between measurements.

Method A is often used to acquire time sequences of axial strain images  $\epsilon_{11}(\mathbf{x}, t)$  by flush mounting a linear array transducer into the compression plate [90], as shown in Fig 2.5a. We can also apply strain stimuli to estimate stress relaxation and complex compliance/modulus parameters, or we can modify the technique to estimate lateral strain for Poisson's ratio estimates. In the latter case, samples are submerged in a water-alcohol solution without the force balance, and a step strain  $\epsilon_{11}(t) = \epsilon_a u(t - t_0)$  is applied. The transducer in Fig 2.5a is rotated  $90^\circ$  to scan the sample from the side and measure true lateral strain  $\epsilon_{22}(t) = \ln(1 + \Delta w(t)/w)$ . A sample of width  $w$  will expand a time-

varying distance  $\Delta w(t)$  when compressed from above and held. Therefore Poisson's ratio is  $\nu(t) = -\ln(1 + \Delta w(t)/w)/\ln(1 + \epsilon_a)$  for  $t > t_0$ .

*Method B – Uniaxial Compression in Confined Samples.* Method B is illustrated in Fig 2.5b.

Cylindrically shaped samples encased in rigid plastic are compressed uniaxially with a step strain to measure stress relaxation. There is a porous bottom surface that allows fluids to pass but not the gelatin. After preparation in a sealed syringe, the end is removed and a moist gauze and fine screen are attached to the expose gelatin surface before mounting. A 1 s compressive ramp displacement is applied from above with the motion controller and held constant while measuring the force. Displacement and force are converted to true stress and strain as shown above. Eq (2.20) describes the wave modulus for confined samples.

Originally the goal was to measure creep in confined samples. However method B apparatus is unable to generate artifact-free creep data, so we settled for stress relaxation data. Comparisons are made using the analysis in Section 2.1.4 and are discussed below.

*Method C – Cone-Plate Rheometer Measurements.* Method C is illustrated in Fig 2.5c.

We measured shear compliance under the strict boundary conditions of a Haake cone-plate rheometer (Thermo Electron Corp., Model RS150, Waltham MA) to validate compressive compliance estimates. Comparisons were made by applying the analysis of Section 2.1.3.

Molten gelatin was poured into the rheometer plate at approximately 30°C so that it covered the edges of the cone. The sample was closed to outside air and cured 1-4 days before measurements. This preparation eliminated slippage at surfaces when the sample

was sheared. A short duration ramp shear stress at either  $\sigma'_a = 3$  Pa or 30 Pa was applied and held while strain was recorded for times up to 3000 s at a rate of 3 samples/s. Eq (2.16) represents data acquired by these measurements. The rheometer was also capable of harmonic stimuli at frequencies between 0.0001 Hz and 15 Hz.

*Method D – Indentation Methods.* Method D is illustrated in Fig 2.5d. Indentation is a widely accepted method for estimating the elastic modulus. Sixty-millimeter-diameter gel samples were placed on the force balance. A flat, 3-mm-diameter cylindrical indenter was pressed into the sample surface by a programmable amount using a known sinusoidal displacement stimulus at a frequency of 0.02 mm/s while measuring the applied force on the balance. Ten cycles were recorded for each sample at 3 surface locations near the center. Displacement and force measurements were used to calculate elastic modulus using the methods of Hayes et al. [91].

### 2.1.8 Data Processing

The digital balance samples force with a variable time interval due to limitations of the instrument. However a time stamp for each sample is available. The average sampling frequency is 3.4 samples/s. Creep data are interpolated to 10 samples/s and then downsampled a factor of 5 to facilitate curve fitting; the final sampling interval is  $\Delta t = 0.5$  s.

VE parameters are estimated by fitting creep data, e.g., curve b in Fig 2.1a, to an  $L$ th-order Voigt model, where  $L = 1, 2$  or 3. Fitting is achieved using optimization techniques using Matlab's Optimization Toolbox, LSQCURVEFIT, where  $D(t)$  from Eq (2.17) is the

function that is fit to the measurements  $\hat{D}[n\Delta t] = \hat{\epsilon}[n\Delta t]/\sigma_a$ . The unbounded Levenberg-Marquardt optimization option is selected. Monte Carlo tests showed the algorithm quickly converges if the initialization parameters are close to the true values and the number of fit parameters is minimized.

We first estimate steady-flow viscosity in a pre-processing step so it can be subtracted from the data before curve fitting. The estimate  $\hat{\eta}_0^{-1}$  is found by computing the derivative  $\dot{D}(t) = (d\hat{\epsilon}/dt)/\sigma_a$  over the measurement time, identifying the time at which  $\dot{D}(t)$  becomes constant with time, and then averaging subsequent values:  $\hat{\eta}_0^{-1} = \sum_n \dot{D}[n\Delta t]/N_\Delta$  for the  $N_\Delta$  points where  $t = n\Delta t > 2T_{max}$ . Eliminating the steady-state viscosity term before model fitting speeds convergence.

### 2.1.9 Goodness of Fit and Model Order

Results from fitting  $N'$  pre-processed creep compliance data points to a Voigt model of order  $L$  with fit parameters  $\theta = (\epsilon_0, \epsilon_1, T_1, \dots, \epsilon_L, T_L)$  are evaluated by computing the  $\chi^2$  value [92],

$$\chi_L^2 = \sum_{n=1}^{N'} \frac{\left(\hat{D}[n\Delta t] - D[n\Delta t; \theta]\right)^2}{\text{var}_D}. \quad (2.23)$$

For a third-order model,  $\theta$  has dimension  $2L + 1 = 7$ . Also,  $\text{var}_D$  is the variance of  $\hat{D}(t)$  estimates.  $\chi^2$  has  $\xi = N' - (2L + 1)$  degrees of freedom. We compute the probability  $Q(\chi^2; \xi)$  that the observed chi-square exceeds  $\chi^2$  by chance assuming the measurement errors are normally distributed.  $Q(\chi^2; \xi)$  were computed using the incomplete gamma function [92]. We select  $L$  by finding the lowest order model for which  $Q > 0.2$ . Curve

fitting in the time domain favors long response times, so  $Q$  plays an essential role in helping us determine model order.

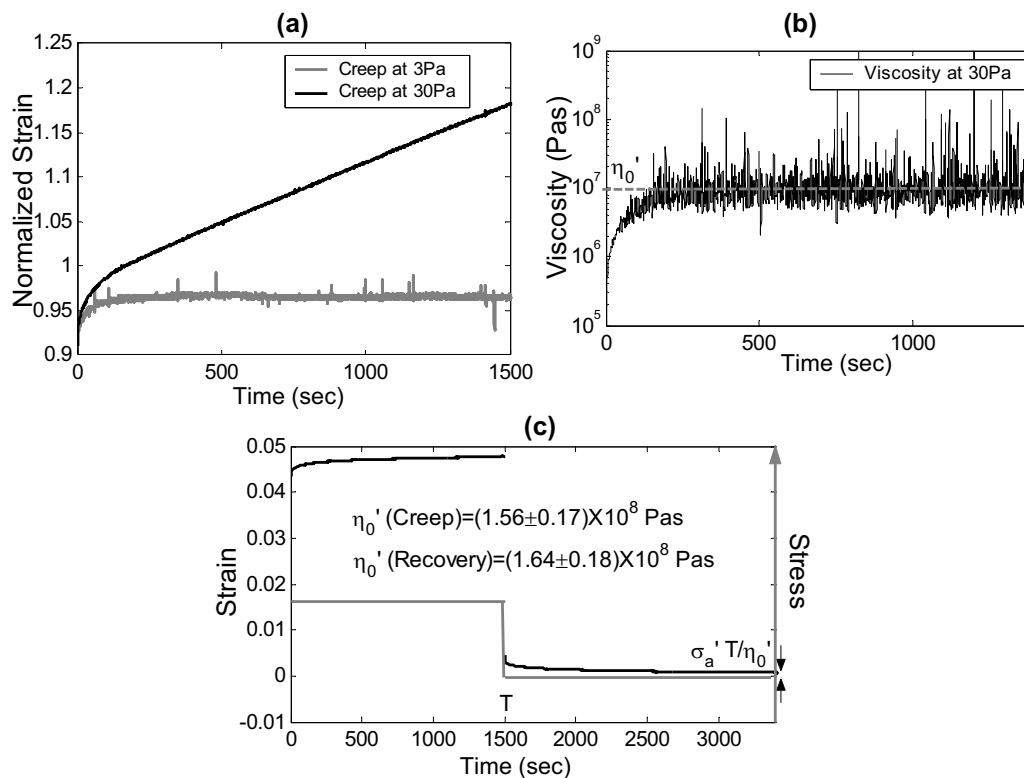


Figure 2.6: (a) Shear creep measured with applied step stresses of  $\sigma_a' = 3$  and 30 Pa using Method C and Type B gelatin (5.5%). (b) Viscosity estimates (Section 2.1.3) versus time for creep data at 30 Pa. Steady-state values were attained beginning at  $\sim 600$  s. (c) Example of shear creep recovery curve for Type A gelatin at  $\sigma_a' = 100$  Pa. Values calculated from the creep and recovery phases are reported separately.

## 2.2 Results

### 2.2.1 Viscosity

Shear creep experiments (Method C) were conducted to estimate the steady-state shear-flow viscosity coefficient,  $\eta'_0$ . Fig 2.6a shows there is a constant equilibrium strain for the step stress amplitude  $\sigma'_a = 3$  Pa, indicating no fluid flow. However, there is a linearly increasing strain in the same samples for the  $\sigma'_a = 30$  Pa stimulus, indicating that flow occurs. Using the 30 Pa data, we estimate viscosity versus time in Fig 2.6b to find the steady-state value of  $\eta'_0 \sim 10^7$  Pa s for Type B gelatin. A creep recovery method [53] was also applied, Fig 2.6c, to Type A gelatin (5.5%) at 100 Pa shear stress to find  $\eta'_0 \sim 10^8$ . Estimates from the creep and recovery phases of Fig 2.6c are approximately equal as expected.

Gelatin gels are rheodictic only when sufficiently stressed. They behave like a VE solid ( $\eta'_0 \rightarrow \infty$ ) at 3 Pa and like a VE polymer saturated in a viscous fluid at stresses above 30 Pa. Viscosity measurements in gelatin gels are constant above a stress threshold, although the values depend on gelatin concentration and type. A power-law dependence of  $\eta'_0$  on gelatin concentration has been observed by others [89].

### 2.2.2 Linearity

Unconfined gelatin samples were strained uniaxially with the harmonic stimulus  $\epsilon_{11}(t) = \epsilon_a \sin(\omega_0 t)$ , where  $\omega_0 = 2\pi \times 0.03$  mm/s, to generate the stress-strain curves of Fig 2.7a. Data shown are from the ninth cycle. Considering strain above 0.01, the on-load halves of

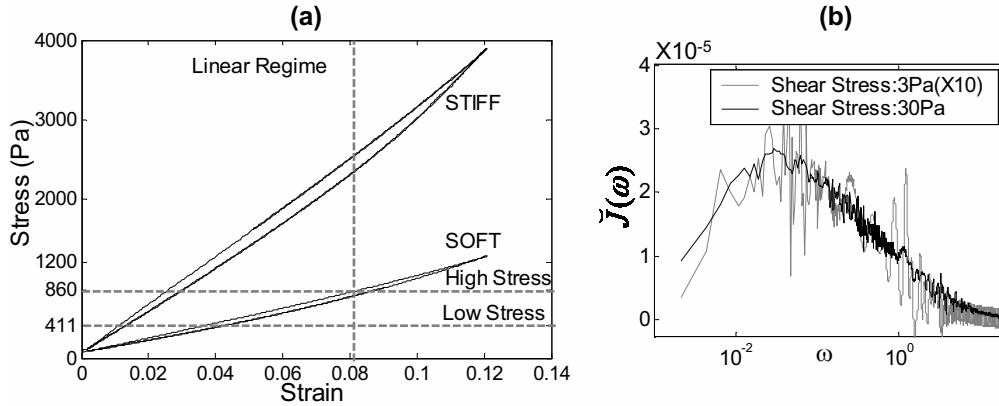


Figure 2.7: Demonstrations of linearity. (a) Stress-strain curves for stiff (10%) and soft (5.5%) Type A gelatin using unconfined samples and uniaxial harmonic stimuli (Method A). The two stress levels indicated were used in subsequent creep measurements. (b) Shear creep Fourier spectra for Type B gelatin (Method C).

each curve (top lines) are linear with a correlation coefficient  $r^2 = 0.9999$  for stresses up to 0.86 KPa for the soft gel and up to 3 KPa for the stiff gel. As expected for linear media, no significant change in resonance times (retardance or relaxation) was observed at these stress levels.

To examine linearity in shear, we measured shear creep spectra at  $\sigma'_a = 3$  Pa and 30 Pa using Method C. The 3 Pa spectral values were multiplied by 10 and plotted with the 30 Pa spectrum in Fig 2.7b. Visual agreement between the two curves indicates a linear VE creep response in this shear stress range despite the higher noise levels in the 3 Pa data.

### 2.2.3 Poisson's Ratio

Applying the step strain  $\epsilon_{11}(t) = \epsilon_a u(t-t_0)$  to a 5.5% gelatin cube and measuring  $\epsilon_{22}(t)$  across the entire sample width, we estimated  $\nu(t)$  as described for Method A in Section

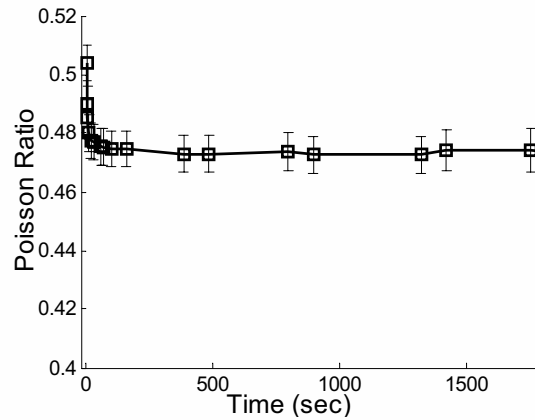


Figure 2.8: Poisson’s ratio estimates versus time,  $\nu(t)$ . Error bars denote one standard deviation computed by propagating displacement measurement errors.

2.1.7. The results are shown in Fig 2.8. Initially, the sample responds incompressibly; i.e., the  $\nu(0) \simeq 0.5$  within the measurements uncertainty. Within 100 s, however,  $\nu(t)$  has fallen to an equilibrium value of 0.473, such that the ratio of equilibrium bulk and compressive compliances increases from zero to  $B(\infty)/D(\infty) = 3(1 - 2\nu(\infty)) = 0.162$ . Consequently, creep model parameters obtained in compression and those in shear cannot be directly compared.

## 2.2.4 Effects of Acquisition Time

The longest duration resonance time determines the total required acquisition time. In gelatin gels, data must be acquired up to an hour to visualize the entire bandwidth. However, as acquisitions lengthen, the importance of eliminating the steady-state viscosity term increases. We summarize in Fig 2.9 the effects of acquisition time on contrast and retardance time estimates with and without eliminating the viscosity term. Results suggest

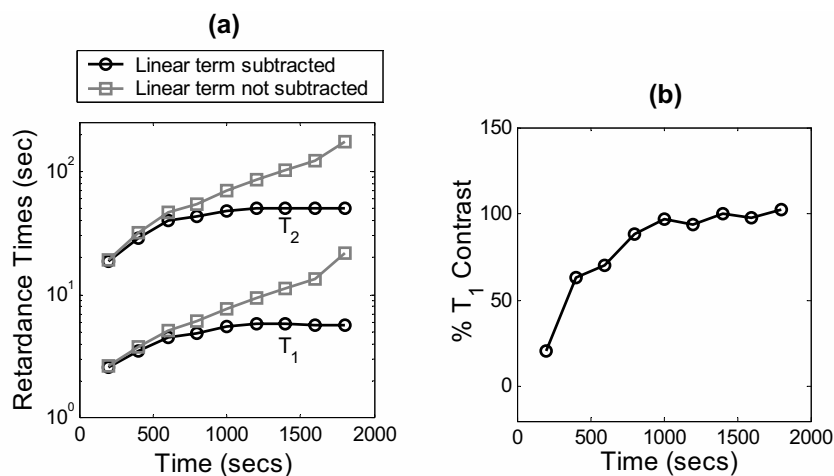


Figure 2.9: (a) Dependence of  $T_\ell$  on acquisition time, and the effect of eliminating steady-state viscosity (linear term in Eq (2.17)).  $T_1$  and  $T_2$  estimates for a third-order Voigt model are shown. (b) Variation of  $T_1$  contrast over acquisition time is shown.

that the acquisition time must exceed twice the value of the longest response time constant. Failure to eliminate even the weak viscosity term of these gelatin gels introduces bias. Furthermore, decreased acquisition times causes a decrease in contrast.

### 2.2.5 Validation

In Fig 2.10, measurements from different experimental geometries are compared. One of the advantages of using standard rheological models is the opportunity to interconvert some parameters from one experiment into another. Elastic modulus estimates  $E_0$  measured using five techniques in compression and shear are plotted in Fig 2.10a: Method A with step stress (CR), step strain (SR) and harmonic stress (OSC) stimuli, and Methods C and D. Mean values of  $E_0$  agree within 6%. Figs 2.10b and c display estimates of equi-

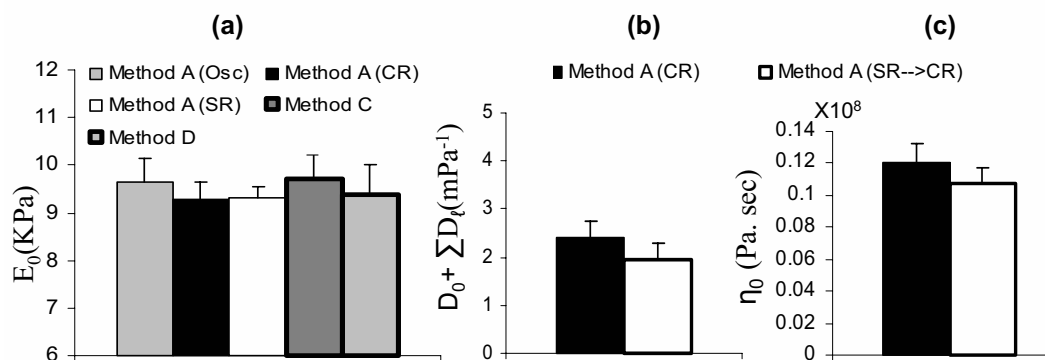


Figure 2.10: Comparisons of measurements made using different methods. Samples were all type A gelatin aged 3 days. (a) Elastic modulus; (b) equilibrium compliance; and (c) steady-state viscosity under compression. Error bars are standard deviations that indicate uncertainty between repeated measurements.

librium compliance and steady-state viscosity from step stress (CR) and strain stimuli of Method A after the response from step strain is converted to an equivalent step stress response (SR  $\rightarrow$  CR) under the assumption  $D(t)E(t) \simeq 1$ . No significant differences were found (Student T-test;  $\alpha = 0.05$ ).

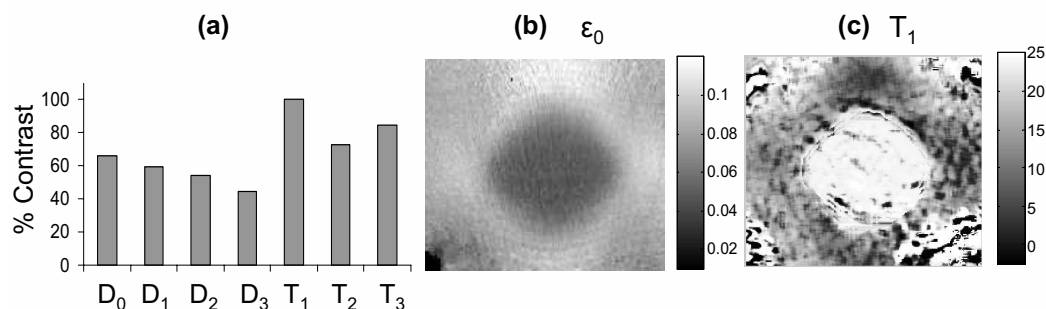


Figure 2.11: (a) Contrast between 10% and 5.5% homogeneous gelatin samples for seven compliance parameters. (b) Example  $\epsilon_0$  image for a composite sample consisting of 5.5% gel background with a 10% gel inclusion. (c) Example  $T_1$  image.

## 2.2.6 Image Contrast

Viscoelastic measurements of gelatin, modeled as third-order discrete processes, are characterized by eight parameters. Which of these parameters are best for imaging? In practice, the answer depends on the conditions and reasons for obtaining the image. Yet we can illustrate the point by estimating parametric contrast for different gelatin concentrations that simulate conditions of a fibrotic lesion.

For two homogeneous phantoms with gelatin concentrations of 5.5% and 10%, contrast magnitude for parameter  $X$  is  $C_X = |(X_{\text{stiff}} - X_{\text{soft}})/X_{\text{soft}}|$ . Fig 2.11 displays percent contrast values for seven of the eight parameters characterizing a third-order compliance model.

Table 2.1 shows that viscoelastic amplitudes  $D_1, D_2, D_3$  are at least an order of magnitude lower than the elastic amplitude  $D_0$ , and yet the contrasts are quite similar. Assuming  $E_0$  increases with the square of gelatin concentration [57, 89] and  $D_0 = 1/E_0$ , we can estimate  $D_0$  contrast as  $|(10^{-2} - 5.5^{-2})/5.5^{-2}| = 0.69$ . The estimate is close to the measured value of 0.65 found in Fig 2.11a. Since  $D_0$  is the largest of the amplitude parameter contrasts and its greater amplitude provides a superior signal-to-noise ratio,  $D_0$  is a good candidate for imaging.

In practice, we image strain  $\epsilon_0(\mathbf{x}) = D_0(\mathbf{x})\sigma_a(\mathbf{x})$ . If  $\sigma_a(\mathbf{x}) = \sigma_a$  is constant throughout the volume, then elastic strain images are proportional to the compliance distribution. However it is well known that stresses in heterogeneous media vary with position [93]. For example, Fig 2.11b is an  $\epsilon_0$  image of a 5.5% gelatin block into which a stiff cylindrical in-

Table 2.1: Viscoelastic parameters for 5.5% gelatin acquired by fitting measurements to model functions. First column lists the discrete viscoelastic model order. Second column contains compressive compliance [ $\text{kPa}^{-1}$ ] and retardance time [s] constants from data of Fig 2.12a. Third column contains wave modulus [kPa] and relaxation time [s] constants from Fig 2.12b. Fourth column contains shear compliance [ $\text{kPa}^{-1}$ ] and retardance time constants from Fig 2.12c. Fifth column contains compressive relaxation modulus [kPa] and relaxation time constants from Fig 2.12d.  $Q$  is the probability from  $\chi^2$  goodness-of-fit test.

MO	Fig 2.12a		Fig 2.12b		Fig 2.12c		Fig 2.12d	
2	$D_0 = 0.109$	$T_1 = 26.8$	$M_0 = 307$	$T_1 = 13.7$	$J_0 = 0.908$	$T_1 = 9.8$	$E_1 = 0.46$	$T_1 = 22$
	$D_1 = 0.005$	$T_2 = 338$	$M_1 = 47.9$	$T_2 = 198$	$J_1 = 0.024$	$T_2 = 69.5$	$E_2 = 0.47$	$T_2 = 302$
	$D_2 = 0.006$		$M_2 = 77.6$		$J_2 = 0.027$			
	$Q = 0$		$Q = 0$		$Q = 0.34$		$Q = 0$	
3	$D_0 = 0.107$	$T_1 = 5.5$	$M_0 = 307$	$T_1 = 1.5$	$J_0 = 0.904$	$T_1 = 2.8$	$E_1 = 0.36$	$T_1 = 3.5$
	$D_1 = 0.004$	$T_2 = 49.8$	$M_1 = 65.3$	$T_2 = 53$	$J_1 = 0.015$	$T_2 = 16.0$	$E_2 = 0.32$	$T_2 = 40$
	$D_2 = 0.004$	$T_3 = 369$	$M_2 = 38.6$	$T_3 = 237$	$J_2 = 0.017$	$T_3 = 69.7$	$E_3 = 0.43$	$T_3 = 310$
	$D_3 = 0.006$		$M_3 = 61.3$		$J_3 = 0.024$			
	$Q = 0.65$		$Q = 0.48$		$Q = 0.41$		$Q = 0.30$	

clusion of 10% gelatin [27] is placed. Strain in the regions surrounding the inclusion vary because the local stresses are nonuniform.

$T_1$  and either  $T_2$  or  $T_3$ , depending on available acquisition times, are also reasonable choices to represent fluid and matrix responses of gelatin. An example  $T_1$  image is shown in Fig 2.11c. Lesion areas are brighter indicating that mechanisms take longer due to the increased collagen density when compared to softer background areas.  $\epsilon_0$ ,  $T_1$  and  $T_2$  are the three parameters currently used for viscoelastic imaging [90]. The measurements of Fig 2.11 should be repeated to select parameters for imaging biological tissues.

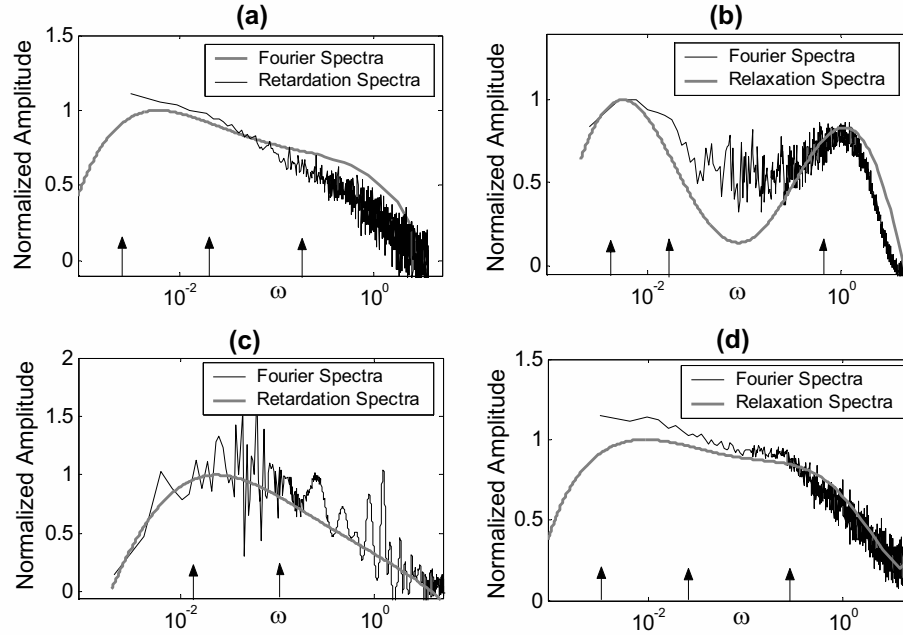


Figure 2.12: Normalized Fourier, retardation, and relaxation spectra. (a) Unconfined type A gelatin samples (aged 3 days) loaded uniaxially at  $\sigma_a = 860$  Pa are measured for 2000 s using Method A. (b) Confined type A gelatin samples (aged 1 day) strained uniaxially at  $\epsilon_a = 0.02$  are measured for 2500 s using Method B. (c) Type B gelatin samples (aged 1 day) sheared at  $\sigma'_a = 3$  Pa are measured for 3000 s in a rheometer using Method C. (d) Unconfined type A gelatin samples (aged 3 days) strained uniaxially at  $\epsilon_a = 0.08$  are measured for 2000 s by combining Methods A and B. Arrows indicate frequencies corresponding to the resonance times given in Table 2.1. Spectral amplitudes are uniformly reduced across the bandwidth as samples age.

### 2.2.7 Viscoelastic Spectra

Fig 2.12 displays Fourier spectra with corresponding resonance time distributions for four experiments. Specifically, we plot  $\check{D}(\omega)$  and  $\tilde{L}^{(3)}(\omega)$  in part (a),  $\check{M}(\omega)$  and  $\tilde{H}^{(5)}(\omega)$  in part (b),  $\check{J}(\omega)$  and  $\tilde{L}^{(3)}(\omega)$  in part (c), and  $\check{E}(\omega)$  and  $\tilde{H}^{(3)}(\omega)$  in part (d). The notation  $\tilde{L}^{(3)}$  indicates the approximation to Eq (2.13) converges at  $k = 3$ . The Fourier spectral bandwidth in each case is less than 10 rad/s.

Table 2.1 lists parameters estimated by curve fitting the data in Fig 2.12 to model func-

tions. The  $\chi^2$  probabilities in Table 2.1 show that a third-order model is required for uniaxial compression (Figs 2.12 a,b) to meet the goodness-of-fit criteria for accepting a discrete model representation, i.e.,  $Q > 0.2$ . In shear, Fig 2.12c, a second order Voigt model was found sufficient. Resondance times  $T$  for acceptable model fits are indicated in the plots by arrows at the corresponding frequencies  $\omega = 1/T$ .

The spectrum of the confined gelatin sample in compression, Fig 2.12b, is clearly bimodal. The high-frequency spectral peak corresponds to the fastest relaxation time constant, and the low-frequency peak corresponds to the two slowest relaxation times constants.

The spectrum of the unconfined sample in compression, Fig 2.12a, could be bimodal, however, the poles of the Voigt model appear more uniformly distributed along the log-frequency axis. The spectrum of the sheared sample, Fig 2.12c, appears unimodal and skewed. The two poles suggest a second-order Voigt model.

Fig 2.12 increases confidence that creep and stress relaxation spectra may be compared: the creep response of Fig 2.12a is a very similar to the stress relaxation response of Fig 2.12d. Spectral similarity suggests that relaxation and retardation times are similarly distributed even if resondance times from the Voigt and Maxwell models may not be easily related.

## 2.3 Discussion

These data allow us to address a few fundamental questions regarding elasticity imaging. Can we interpret properties of the polymeric molecular structure from viscoelastic parameters? If so, which parameters are most promising for imaging and how should we measure them. The conclusions apply to biological tissues only if gelatin gels are a reasonable model, which has yet to be tested.

Regarding interpretation, there is a rich literature on molecular theories of polymer dynamics for standard measurement geometries based on spectral data similar to Fig 2.12. Ferry [53] shows that relaxation and retardation spectra have two maxima when the molecular weight of weakly cross-linked polymers is greater than a threshold value. We see two broad peaks in gelatin spectra near  $\omega = 1$  and 0.01. The high-frequency peak may be from frictional forces, i.e., electrostatic and hydrogen bonds, that resist local deformation as polymer fibers are straightened. Short-range movement of collagen molecules in viscous fluids delays the viscoelastic response only a short time as weak bonds reversibly stretch, dissociate, and associate. The low-frequency peak of the bimodal spectra may be from dragging fully extended peptide chains of relatively high molecular weight through the tangled polymer matrix. Ferry refers to this as “entanglement coupling”. Because these movements occur over a large spatial scale, longer response delays are expected.

Tschoegl [79] also addresses the dynamic behavior of weakly cross linked polymers like gelatin gels. He refers to it as pseudo-arrheodictic because the frictional forces between matrix fibers that retard strain in creep experiments can appear as delayed fluid flow. When

the magnitude of frictional forces varies over time, a portion of the VE response is delayed, which generates a bimodal spectrum. The Ferry and Tschoegl descriptions are consistent if one considers that the time required for fibers to be straightened before they are dragged through the matrix could be the source of the characteristic delay. In that case, spectral peak frequencies are expected to depend on the molecular weight and surface charge density of the matrix fibers. A working hypothesis for biological tissues is that disease states alter properties of the extracellular matrix – the natural polymer of the body – to generate disease specific contrast in images of viscoelastic parameters.

In both short duration (fluid) and long duration (matrix) responses of gelatin, frictional forces from bending peptide chains and their attraction to the surrounding structured fluids vary in strength given the randomness of the matrix geometry. Thus there are not two response times as expected from discrete modeling but two distributions of times as observed from the spectra of Fig 2.12a,b,d. The observation that  $L^{(k)}$  and  $H^{(k)}$  were found to converge suggests continuous distributions of response times are reasonable to assume.

Confining samples as in Fig 2.12b forces fluids to flow before the matrix can respond [94]. In the unconfined samples of Figs 2.12a,d, however, these processes can begin simultaneously. We see from Table 2.1 that response times for the high frequency peak, 3.5 s and 5.5 s for the unconfined samples, decreases to 1.5 s in the confined sample, while changes in the low-frequency responses are less pronounced. Sample confinement appears to separate and narrow the distributions as expected from the Ferry and Tschoegl

descriptions.

In shear creep (Fig 2.12c), tensile forces are applied to the matrix instead of compression. Forces on the matrix fibers near the circumference of the cone-plate are much larger than those near the center of rotation. Consequently, even small rotations engage the matrix immediately. Since polymers resist tensile deformations more than comparable compressive deformations, the larger low-frequency matrix response observed compared to the high-frequency fluid response is expected. Thus the skewed, unimodal appearance of the spectrum in Fig 2.12c may reflect an increased relative weighting of the low-frequency response.

Clearly low-order discrete viscoelastic models do not provide physical descriptions of polymers. Rather they are parsimonious summaries that help guide selection of imaging parameters. Our burden is to show those parameters are related to essential biological processes. We are concerned that apparently bimodal spectra require third-order discrete models to meet the  $\chi^2$  criteria. At this time, we recommend using spectra to observe the number of modes, and then averaging time constants detected within each mode. For the spectrum of Fig 2.12a, where the  $\chi^2$  criterion suggests a third-order model, we would nevertheless average time constants corresponding to the two lowest frequency poles and therefore report  $T_1 = 5.5$  s and  $T_2 = 209.5$  s.

Given the interpretation above, it seems that images of elastic strain  $\epsilon_0$ , and the retardance times  $T_1$  and  $T_2$  form a concise feature space for strain imaging investigations. The frame rate of current ultrasound systems easily provides sufficient temporal resolution to

sample the viscoelastic response bandwidth without aliasing. The challenge for viscoelastic parameters is to acquire data over a sufficient time duration to sample the low-frequency spectral response and estimate steady-state viscosity,  $\eta_0$ . The longest response time for gelatin is less than 400 s, so acquisitions of 800 s are sufficient when  $\eta_0$  is large. Even though the steady-state viscosity of gelatin is relatively high, it competes with viscoelastic responses and therefore must be eliminated before analyzing the VE response to minimize parameter biases. The threshold for rheodictic strain responses in gelatin is low, less than 30 Pa.

A different approach to viscoelastic modeling that is gaining momentum models the constitutive equation as a fractional derivative [79, 95]. Instead of exponential time dependencies, strain retardation (or stress relaxation) is modeled as algebraic decays [96, 97]. Mathematically,  $\epsilon_{VE}(\mathbf{x}, t) = D_1(\mathbf{x})\mathcal{D}^\alpha\{\sigma(\mathbf{x}, t)\}$ , where  $\mathcal{D}^\alpha$  is the fractional derivative operator applied to the stimulus and  $0 < \alpha < 1$ . The fractional derivative result can form a concise feature representation by the two parameters:  $D_1(\mathbf{x})$  and  $\alpha(\mathbf{x})$ . In fact [95] shows that there is also a molecular basis for interpreting these parameters in polymer solutions. However the interpretation in cross-linked polymeric solids with arrheodictic behavior, like gelatin and soft connective tissues, is still empirical in the sense that  $\alpha$  is a characteristic parameter not directly connected to molecular structures.

The creep response in gelatin is well represented by linear viscoelastic theory for applied stresses up to 3 kPa, although the range depends on gel stiffness. The literature for some biological tissues shows a lower threshold for nonlinear responses [77]. The question

of interpreting VE parameters for images obtained during large, nonlinear deformations is open [98]. Anecdotal evidence from imaging [75, 27] shows there is little change in contrast even for large compressions where nonlinear responses are clearly expected. While interpretation of parameters in terms of polymer structure may require linearity, detection of features in imaging based on contrast may not. Also, strain errors generated by violations of the linear assumption are relatively small compared with other sources of imaging errors. For example, strain variance increases as ultrasonic echo signals decorrelate during complex motions of heterogeneous media and from echo fields undersampled with respect to the bandpass of strain gradients [27]. In addition, strain is not directly proportional to compliance when the boundary conditions generate spatially variable local stresses. The generally large object contrast for many biological imaging tasks [24] and the use of Lagrangian coordinates to estimate strain [99] give images of viscoelastic parameters diagnostic value despite violations of assumptions that permit interpretation of results at the molecular scale.

## 2.4 Appendix A

**Ramp and hold stress stimulus.** Consider the first-order Voigt model in shear,  $s\tilde{J}(s) = J_0 + J_1/(1 + T_1s)$ , where we assume  $t/\eta'_0 \sim 0$  during the measurement time [79]. Let's

apply a ramp shear stress  $\sigma_{12}(t) = \sigma_a r(t_0; t_1)$  over the time interval  $(t_0, t_1)$ :

$$r(t_0; t_1) = \begin{cases} 0 & t \leq t_0 \\ t/(t_1 - t_0) & t_0 \leq t \leq t_1 \\ 1 & t \geq t_1 \end{cases} \quad (2.24)$$

In the Laplace domain,  $\tilde{\sigma}_{12}(s) = (\sigma_a/(s^2 t'))[1 - e^{-t's}]$ , where  $t' = t_1 - t_0$ . Combining this information with Eq (2.15) and taking the inverse Laplace transform yields shear creep for a ramp stress:

$$\gamma_{12}(t) = J_0 \sigma_a + J_1 \sigma_a \left( 1 + \frac{T_1}{t'} \exp(-t/T_1) (1 - \exp(t'/T_1)) \right) \quad \text{for } t \geq t_1. \quad (2.25)$$

In the limit of  $t' \rightarrow 0$ , we obtain the response to a step stress  $\gamma_{12}(t) = \gamma_{(12)0} + \gamma_{(12)1} (1 - \exp(-t/T_1))$ .

This can be extended to higher order models for a linear system via

$$\gamma_{12}(t) = \gamma_{(12)0} + \sum_{m=1}^M \frac{\gamma_{(12)m}}{t'} (t' + T_m \exp(-t/T_m) (1 - \exp(t'/T_m))) \quad \text{for } t \geq t_1. \quad (2.26)$$

Ramp stimuli reduce the magnitude of viscoelastic responses compared to a step stimulus, particularly at high frequencies, but do not bias retardance time estimates. Results for a compressive ramp stress stimulus yield equivalent effects. For example, Fig 2.1b compares bimodal spectra simulated with step and 1-s ramp stress stimuli.

## 2.5 Appendix B

**Sample Rest Period Analysis.** Whenever possible, parameter uncertainty was estimated using data from identical samples measured once each. Measurements were repeated

on the same sample only when necessary. We avoided repeated measurements on the same sample because viscoelastic responses are known to depend on deformation history. The following study tests how the rest time allowed between measurements affected estimates.

Fig 2.13 summarizes the results of a creep experiment conducted on two gelatin samples with identical properties using Method A where  $\sigma_a = 733$  Pa. Sample I was rested one hour between the first two measurements and then two hours between measurements 2 and 3. Sample II was rested two hours and then one. Resting one hour biased retardance times high by as much as a factor of two. Waiting 2 hours reduced biases significantly, although it is clear that the exact deformation sequence is important. It might seem reasonable to recommend three or four hour rests, except that cross linking also increases over time in gelatin. We recommend keeping the applied load as low as possible and allowing two hour rests between measurements of 3000 s, or at least twice the acquisition time for shorter duration measurements. Two hour rests are a compromise between the polymeric changes from deformation and those from curing.

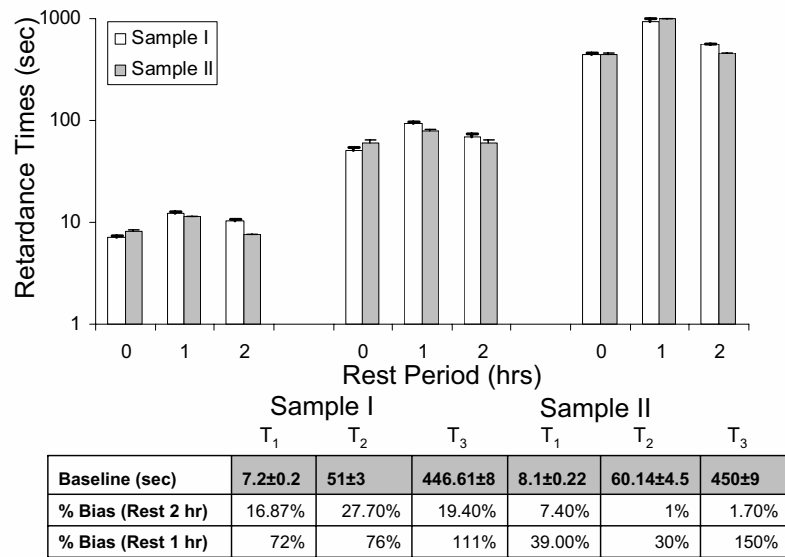


Figure 2.13: Effects of rest time on viscoelastic estimates. Top: Variation of  $T_1$  (left group),  $T_2$  (middle group), and  $T_3$  (right group) for a third-order Voigt model are shown for baseline measurements (0) and rest times of 1 and 2 hours. Error bars indicate fitting uncertainties. Bottom: Table showing initial baseline retardance times in seconds and percent biases for rest times of 1 or 2 hours between measurements.

## **Chapter 3**

# **Viscoelastic Imaging on Gelatin**

## **Hydropolymers**

There are several techniques that use phase-sensitive imaging modalities such as ultrasound and MRI to image mechanical properties of soft tissues [5]. The basis for their development is that disease processes alter tissue viscoelastic properties [100, 24]. Measurements of these properties may be made using external quasi-static [28] or dynamic [33, 63] excitations or using ultrasound generated radiation force [41, 62]. Studies on the breast have shown promising results for palpable lesions when differentiating benign versus malignant on the basis of elastographic contrast [73, 74, 30]. However, recent studies on early-stage non-palpable masses [75] show that elastic strain images can be non-specific if the mechanical response depends on the physiological [23] and cellular microenvironmental processes [64] of a specific patient. For example, literature on the ultrastructure

of extracellular matrix in breast lobules describes profound changes occurring during tumor formation [15]. These changes can be detected by imaging viscoelastic features in combination with elastic features.

In this chapter we propose a straightforward extension to ultrasonic quasi-static elasticity imaging by including time-varying strain information obtained during creep experiments. The imaging methods are developed using animal-hide gelatin hydrogels since they provide tissue-like mechanical properties [51, 52, 56, 86], are simple to construct, and are elastically uniform within the resolution of the ultrasonic imaging system. High molecular-weight gels consist of a matrix of relatively long and interconnected peptide chains whose structure and surface charges determine the viscoelastic behavior [53]. Consequently, mechanical properties of gelatin gels vary with pH and other alterations to ion concentration in a manner similar to breast stroma. Gelatin is also sensitive to thermal and mechanical histories. While gelatin is derived from type I collagen also found in breast stroma, there are ultrastructural differences that change the viscoelastic responses of the two media. The collagen in gelatin is denatured, giving it a relatively lower material strength, and there is no polysaccharide gel surrounding the polymer chains [10].

We showed that a short ramp-and-hold stress stimulus combined with carefully timed RF acquisitions to estimate time-varying strain can describe the spatial distribution of viscoelastic properties in gelatin (Chapter 2) [1] and breast tissue [101] in the low-frequency bandwidth of quasi-static deformations ( $<1.5$  Hz). Despite structural differences, there are enough similarities between breast stroma and gelatin gels creep responses to suggest

gelatin is a reasonable physical model. The average creep response in gelatin is well represented by linear viscoelastic theory; it can have both solid and fluidic features depending on the nature of the stress stimulus. The distribution of creep retardance times is continuous, broadband and bi-modal (Chapter 2) [1], consistent with the responses expected from lightly cross-linked polymers [53]. We hypothesize that the bi-modal spectrum comes from quick, short-range movement of collagen molecules within viscous fluids, and slower and longer-range entanglements among the polymer fibers. Within a few seconds after applying the stimulus, weak inter-fiber bonds reversibly stretch while some dissociate and re-form. Fully extended peptide chains then appear to be dragged through the tangled polymer matrix (“entanglement coupling” [53]). Both processes delay the full strain response thus producing viscous creep. There is, in addition, inelastic fluid movement from unbound water that contributes to creep. While small, its effect must be eliminated to reduce the bias for viscoelastic measurements (Chapter 2) [1]. Within the low bandwidth of the stress stimulus, creep responses are considered too complex to model directly using conventional rheological models. Often ladder models [79] or fractional differentiation [95] are employed to relate macroscopic observations to molecular theories describing material structure.

In this chapter, we investigate the role of a low-order discrete Voigt model as a concise parametric summary of the observed viscoelastic behavior. Specifically we explore the possibility of representing the continuous, bimodal spectra of creep retardance times by a second-order Voigt model. The time constants of the model become the data mapped into

retardance time images. All spectroscopic imaging methods face the same problem – how can a spectrum of data available for each pixel be parameterized to form one or two images without sacrificing essential information?

We also address the important issues of stimulus uncertainty and acquisition time duration on image contrast, parameter bias and noise. These considerations are particularly important for clinical applications where stress stimuli are applied freehand and the available acquisition time may be limited by breath-hold time. Experiences with gelatin provide a framework for future tissue investigations.

## 3.1 Methodology

### 3.1.1 Constitutive Equations for Viscoelastic Imaging

Constitutive equations reveal how material properties of the medium interact with applied mechanical stimuli to generate responses. In imaging experiments, stress  $\sigma(\mathbf{x}, t)$  is often the stimulus, strain  $\epsilon(\mathbf{x}, t)$  is the response, and compliance  $D(\mathbf{x}, t)$  defines material properties of the medium that relate the two. All three quantities can vary in space,  $\mathbf{x}$ , and time,  $t$ . In a creep experiment, the stress field is suddenly applied in time, as given by the weighted unit-step function  $\sigma_a(\mathbf{x}) u(t - t_0)$ , where  $u(t) = 1$  for  $t \geq 0$  and 0 otherwise. The linear constitutive equation becomes

$$\epsilon(\mathbf{x}, t) = D(\mathbf{x}, t)\sigma_a(\mathbf{x})u(t - t_0). \quad (3.1)$$

Compliance may be broken down into the sum of three terms describing time-independent elastic, time-varying viscoelastic and purely viscous responses, respectively,  $D(\mathbf{x}, t) = D_0(\mathbf{x}) + D_{ve}(\mathbf{x}, t) + D_v(\mathbf{x}, t)$  for  $t > t_0$ . The elastic response  $D_0(\mathbf{x})$ , which is assumed to be the only significant term in strain imaging using quasi-static stimuli [28, 27, 81], is inversely related to the elastic modulus. In this study the viscous response,  $D_v = (t - t_0)/\eta_0$ , is estimated and then eliminated from the data before estimating viscoelastic parameters. In gelatin gels, the steady-state compressive-flow viscosity  $\eta_0$  is  $O(10^7)$  Pa·s (Chapter 2) [1].

This report is focused on the viscoelastic response,  $D_{ve}$ . It is often modeled in the polymer-mechanics literature as a continuous distribution of exponentially increasing strains each with retardance time  $\tau$  weighted by the distribution  $L(\tau)$  [53, 79, 82]. The expression is

$$D_{ve}(\mathbf{x}, t) = \int_{-\infty}^{\infty} d \ln \tau L(\mathbf{x}, \tau) [1 - \exp(-(t - t_0)/\tau)] , \quad (3.2)$$

where  $d \ln \tau = d\tau/\tau$ . Since  $D_{ve}(\mathbf{x}, t)$  varies spatially in heterogeneous media, each position can have its own  $L(\mathbf{x}, \tau)$  distribution that form a basis for viscoelastic imaging.

$D_{ve}$  summarizes material properties of the medium that determine the amplitude and duration of the delayed strain in a creep response. Frictional forces from weak collagen cross links are rheologically modeled in Eq (3.2) by Voigt units [79] that produce exponential growth terms. Randomness in the polymer structure generates a large range of cross-link energies that give a broad, continuous distribution of exponential time constants  $\tau$ . Each is weighted by a corresponding compliance amplitude to give  $L(\tau) = \tau D'_{ve}(\tau)$ . In

(Chapter 2) [1], we approximated retardance-time distributions  $L$  from time-varying strain data using methods described by Tschoegl [79].

If a stress relaxation experiment (strain stimulus, stress response) is used instead of creep, relaxation-time distributions  $H(\tau)$  are found with similar techniques. Finally, we wish to point out that some texts [53, 79] plot the distributions  $L(\tau)$  and  $H(\tau)$  as spectra  $\tilde{L}(\omega)$  and  $\tilde{H}(\omega)$  by simply assuming  $\omega = 1/\tau$ . In this chapter we represent everything in  $\tau$ .

Fig 3.1a is an example of a relaxation distribution  $H(\tau)$  for gelatin in a confined measurement geometry as taken from (Chapter 2) [1]. Fig 3.1b is a retardation distribution  $L(\tau)$  also for gelatin in an unconfined measurement geometry. Both distributions are bimodal although clearly the peak locations and modal widths depend on the boundary conditions.

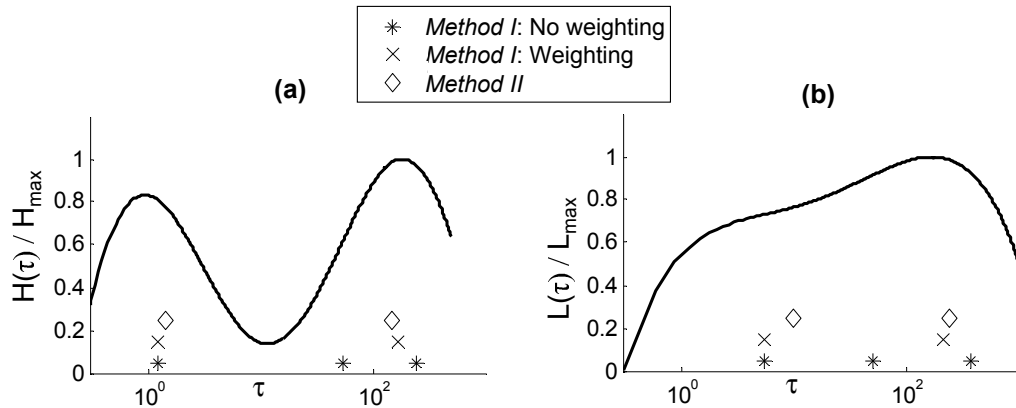


Figure 3.1: (a) Normalized  $H(\tau)$  distribution for gelatin compression in a confined geometry. (b) Normalized  $L(\tau)$  distribution for gelatin compression in an unconfined geometry similar to imaging experiments. Both curves are reproduced from (Chapter 2) [1]. Markers along the  $\tau$  axes indicate estimates of peak response times by applying *Method I* with and without weighting and *Method II* as described in Section 3.1.2

### 3.1.2 Parameterizing Creep Data for Imaging

Given that each mode in the distribution corresponds to a different molecular-scale process and is roughly symmetric about its peak, it seems reasonable to reduce dimensionality by estimating parameters associated with the two modal peaks. We do this by approximating the continuous distributions in Eqs (3.1) and (3.2) with low-order discrete Voigt units [1, 79]. For  $t > t_0$ , the  $P$ th-order model is

$$\epsilon_{ve}(\mathbf{x}, t) = D_{ve}(\mathbf{x}, t)\sigma_a(\mathbf{x}) = \sum_{\ell=1}^P \epsilon_{\ell}(\mathbf{x}) [1 - \exp(-(t - t_0)/T_{\ell}(\mathbf{x}))]. \quad (3.3)$$

Candidates for imaging parameters are viscoelastic strain amplitudes  $\epsilon_{\ell}$  and retardance time constants  $T_{\ell}$ . Since we often cannot measure the applied stress everywhere in the field while imaging, we settle for strain  $\epsilon_{\ell}$  rather than intrinsic compliance estimates. However  $T_{\ell}$  generate more contrast than  $\epsilon_{\ell}$  in gelatin (Chapter 2) [1], thus retardance time constants are selected as imaging parameters in this study. Two methods for estimating viscoelastic parameters are described next.

#### 3.1.2.1 Method I: $\chi^2$ Model Fitting.

Previously we described a  $\chi^2$ -based data fitting technique for choosing the model order  $P$  and estimate parameters from Eq (3.3) (Chapter 2) [1]. Time-varying strain measurements sampled on the interval  $T$  consist of signal  $\epsilon_{ve}$  and white-Gaussian noise  $w$ ;  $\hat{\epsilon}[n] = \epsilon_{ve}[n] + w[n]$  for  $t_0 \leq nT \leq (N - 1)T + t_0$ . At each location in the medium  $\mathbf{x}$  and

Table 3.1: Algorithm for Method I

1. Estimate  $L(\tau)$  from the time-varying strain data of a creep experiment.
2. Record the number of peaks in  $L(\tau)$  as the number of modes  $M$ .
3. Model the strain response using Eq (3.3) and compute  $\chi^2$  and  $Q$  estimates via Eq (3.4).
4. The order of the model is the lowest value of  $P$  for which  $Q > 0.1$ . `Matlab` function `LSQCURVEFIT` is used for fitting.
5. If  $P > M$ , identify the peaks associated with each distribution mode and compute the weighted mean  $T_m = \sum_{\ell}(\epsilon_{\ell}T_{\ell}) / \sum_{\ell} \epsilon_{\ell}$  as the time constant for the mode.
6. For stress-relaxation data, substitute  $H(\tau)$  for  $L(\tau)$ .

for  $P = 1, 2, 3, \dots$ , we compute

$$\chi_P^2 = \sum_{n=1}^N \frac{(\hat{\epsilon}[n] - \epsilon_{ve}[n; \theta])^2}{\text{var}(\hat{\epsilon}[n])}. \quad (3.4)$$

The variance of each samples is  $\text{var}(\hat{\epsilon}[n])$ .  $\epsilon_{ve}[n; \theta]$  is the sampled model function of Eq (3.3) that depends on  $2P$  fit parameters  $\theta = (\epsilon_1, T_1, \dots, \epsilon_P, T_P)$ . We then compute the probability  $Q(\chi_P^2; \xi)$  that the observed chi-square value exceeds the expected value by chance, where  $\xi = N - 2P$  is the number of degrees of freedom. We select  $P$  from the lowest order model for which  $Q > 0.1$ . Values greater than 0.1 suggest the model is an acceptable representation of the data given that the errors are normally distributed. The algorithm for estimating time constants for each mode in the retardation distribution using *Method I* is outlined in Table 3.1.

### 3.1.2.2 Method II: Hankel-SVD Method.

There are several algorithms available for modeling sampled data  $s[n]$  as a linear combination of exponents in noise  $w[n]$  [103]. Described briefly below is a state-space approach

Table 3.2: Algorithm for Method II

1. Place the strain measurements in the proper form and rearrange into the Hankel matrix  $\mathbf{S}$  of Eq (3.5).
2. Apply the HLSVD-PRO algorithm [102]. Select  $R = 2^n$  such that  $n$  equals the value that minimizes  $(\tau_{max}/(5T)) - 2^n$ . Also set  $P = M$  and truncate the data duration at  $nT = 2\tau_{max}$  to compute  $\mathbf{U}'$ .  $\tau_{max}$  is the largest value of  $\tau$  at which  $L(\tau)$  peaks.
3. Apply Eqs (3.7) and (3.8) to compute retardance time values  $T_\ell$  for  $1 \leq \ell \leq M$ .

called the Hankel-SVD method that is used in MR spectroscopy. The assumption is that data can be modeled using  $s[n] = \sum_{\ell}^P s_{\ell} z_{\ell}^{n-1} + w[n]$  with, in our case, damped exponents  $z_{\ell} = \exp(b_{\ell}T)$ . Creep data are modified to fit the form using  $s[n] = \hat{\epsilon}[N] - \hat{\epsilon}[n]$ , assuming the viscous compliance term  $D_v$  has been eliminated,  $(N-1)T > 2(T_{\ell})_{\max}$ , and  $b_{\ell} = -1/T_{\ell}$ .

The data samples  $s[n]$ ,  $0 \leq n \leq N-1$ , are arranged into a matrix of dimension  $(N-R) \times (R+1)$  with Hankel structure,

$$\mathbf{S} = \begin{pmatrix} s[0] & s[1] & \cdots & s[R] \\ s[1] & s[2] & \cdots & s[R+1] \\ \vdots & \vdots & \ddots & \vdots \\ s[N-R-1] & s[N-R] & \cdots & s[N-1] \end{pmatrix}, \quad (3.5)$$

where we choose  $P \leq R \leq N/2$  but typically  $R \leq N/3$ . (See Table 3.2 for details.) The rank of  $\mathbf{S}$  equals the prediction order  $R+1$ .

$\mathbf{S}$  is decomposed into its singular values [104] via

$$\mathbf{S} = \mathbf{U}\mathbf{\Lambda}\mathbf{V}^{\dagger}, \quad \text{where} \quad \mathbf{\Lambda} = \begin{pmatrix} \mathbf{D} & \mathbf{0} \\ \mathbf{0} & \mathbf{W} \end{pmatrix}. \quad (3.6)$$

$\mathbf{V}^\dagger$  is the conjugate transpose of  $\mathbf{V}$ .  $\mathbf{U}$  and  $\mathbf{V}$  are unitary matrices of order  $(N - R) \times (N - R)$  and  $(R + 1) \times (R + 1)$ , respectively, and  $\mathbf{\Lambda}$  is a diagonal matrix containing singular values  $\lambda_1 \geq \dots \geq \lambda_{R+1}$ . The task is to partition  $\mathbf{\Lambda}$  into a  $P \times P$  signal-space matrix  $\mathbf{D}$  and a  $(R + 1 - P) \times (R + 1 - P)$  noise-space matrix  $\mathbf{W}$ . Signals are noisy and  $P$  is unknown, so the model order is often estimated by locating the largest difference between two successive singular values. However, our immediate task is to estimate values for  $\tau$  corresponding to peaks in the  $L(\tau)$  distribution. To locate peaks, we set the size of the signal space to equal the number of modes,  $P = M$ , which for gelatin is 2.

Noise is suppressed by truncating the Hankel matrix:  $\mathbf{S}' = \mathbf{U}'\mathbf{D}\mathbf{V}'^\dagger$ , where  $\mathbf{U}'$  is of order  $(N - R) \times P$  and  $\mathbf{V}'$  is  $(R + 1) \times P$ .  $P$  is also the order of the discrete Voigt model in Eq (3.3).  $\mathbf{U}'$  provides a relationship between the singular values in  $\mathbf{D}$  and the corresponding eigenvalues  $\mathbf{Z} = \text{diag}(z_1, \dots, z_\ell, \dots, z_P)$ . The latter are poles of the model in Eq (3.3) from which  $T_\ell$  are found.

Define  $\mathbf{U}'_{\text{top}}$  to be  $\mathbf{U}'$  with the top row removed,  $\mathbf{U}'_{\text{bot}}$  to be  $\mathbf{U}'$  with the bottom row removed,  $\mathbf{u}$  is the bottom row of  $\mathbf{U}'$ , and  $\mathbf{I}$  is the identity matrix. Then [105]

$$\mathbf{Z}' = \left( \mathbf{I} + \frac{\mathbf{u}\mathbf{u}^\dagger}{1 - \mathbf{u}^\dagger\mathbf{u}} \right) \mathbf{U}'_{\text{top}}^\dagger \mathbf{U}'_{\text{bot}} . \quad (3.7)$$

The relation between  $\mathbf{Z}$  and  $\mathbf{Z}'$  is  $\mathbf{Z}' = \mathbf{Q}\mathbf{Z}\mathbf{Q}^{-1}$ . Although we don't know  $\mathbf{Q}$ , it can be shown that the eigenvalues of  $\mathbf{Z}'$  from Eq (3.7) equal those for the diagonal matrix  $\mathbf{Z}$  that we seek. From the eigenvalues of  $\mathbf{Z}'$ ,  $z_\ell = \exp(-T/T_\ell)$ , we find

$$T_\ell = -\frac{T}{\ln z_\ell} , \quad \text{for } \ell \leq P . \quad (3.8)$$

A more computationally efficient algorithm HLSVD-PRO was used in this study as obtained from the authors [102]. It uses the Lanczos algorithm to speed SVD computation [106] with extensions that exploit the orthogonality among the Lanczos vectors. *Method II* procedures are summarized in Table 3.2.

### 3.1.3 Simulations

Our initial investigation of the two methods for parameterizing continuous  $L(\tau)$  distributions was through Monte-Carlo simulations of creep experiments. Assuming that  $L(\tau)$  follows a log-normal distribution [79], we generated a single-mode, broadband input function  $L(n\Delta\tau)$  as illustrated by the points in Fig 3.2. From Eqs (3.1) and (3.2), we computed measurement signals  $\hat{\epsilon}(t)$  and added independent noise realizations. Signal-independent, zero-mean, white Gaussian noise (WGN) was added to generate strain-data simulations with the high signal-to-noise ratio (SNR) of 40 dB, representative of non-imaging techniques (Chapter 2) [1], and low SNR = 15-20 dB representative of imaging results. Values were calculated using  $\text{SNR (dB)} = 10 \log_{10}(\rho^2/(1 - \rho^2))$ , where  $\rho$  is the correlation coefficient between noisy and noiseless data [107]. SNR was varied by changing the amplitude of the WGN. We also varied the width of the  $L(\tau)$  distribution between 70-500 s in the simulations.

*Method I* was applied to data simulated from the broadband, unimodal input distribution where we set the peak value for  $L(\tau)$  at  $\tau = 100$  s. As seen in Fig 3.2, the best fit gave a bi-modal estimate. Such performance is typical of  $\chi^2$  methods, because they add terms

to the model as needed to achieve the best fit. Nevertheless, a weighted mean of the two peaks gives a value of 123 s, which is reasonably close to the input peak value.

*Method II*, conversely, reduces the size of the signal space according to prior information about the number of distribution modes. Therefore *Method II* is able to estimate one peak value at 103.5 s despite the fact this all-pole technique under-estimates the bandwidth.

The spectral bandwidth may be more accurately determined by increasing  $P$ .

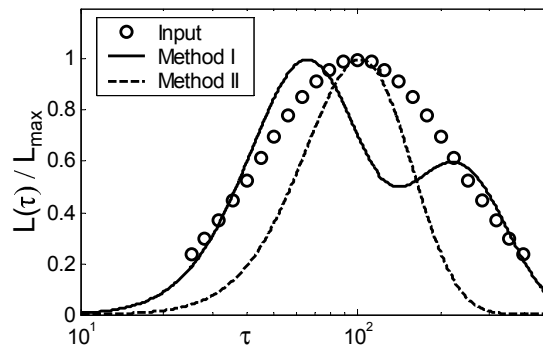


Figure 3.2: Points marked (o) are the log-normal retardation spectra input into the simulation (peak value is 100 s and the bandwidth is 220 s). The lines are estimates of the spectrum from Eq (3.3) fit to the data using *Method I* (solid line) and *Method II* (dashed line).

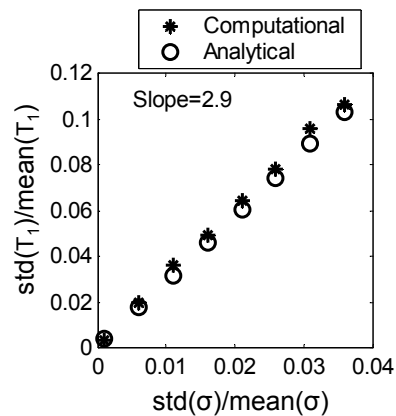


Figure 3.3: The coefficient of variation for  $T_1$  is plotted versus that for the input stress. Predicted values (analytical) and those estimated from simulation (computational) are shown.

### 3.1.4 Retardation-Time Error Analysis

The following section describes how strain uncertainties propagate into errors in retardation time constant estimates  $T_\ell$ . Strain errors can be significant when the applied stress  $\sigma_a$  is not the constant we assume. Uncertainty in  $\sigma_a$  becomes very important when stress is applied by hand as in clinical applications. We now show how stress errors propagate into  $T_\ell$  errors for *Method I*.

Consider the discrete viscoelastic model representation of Eq (3.3) while dropping the spatial notation and setting  $t_0 = 0$  for convenience. The data fits the model best when the  $\chi^2$  metric of Eq (3.4) is minimized; i.e.,

$$\frac{\partial \chi_P^2}{\partial \theta} = -2 \sum_{n=1}^N \frac{(\hat{\epsilon}[n] - \epsilon_{ve}[n; \theta])}{\text{var}(\hat{\epsilon}[n])} \frac{\partial}{\partial \theta} \epsilon_{ve}[n; \theta] = 0 . \quad (3.9)$$

This equation can be solved analytically for the first-order strain model, where  $D_v \simeq 0$ ,

$$\hat{\epsilon}[n] = \epsilon_0 + \epsilon_1 [1 - \exp(-nT/T_1)] , \quad (3.10)$$

by linearizing the equation and arranging terms. We find

$$y[n] = c + m(nT) , \quad (3.11)$$

where  $y[n] = \ln(\epsilon_0 + \epsilon_1 - \hat{\epsilon}[n])$ , the intercept is  $c = \ln(\epsilon_1)$ , and the slope is  $m = -1/T_1$ .

According to the method of least squares [108], the maximum likelihood estimates of  $m$  and  $c$  are obtained by minimizing  $\chi^2$  with respect to each parameter. These can be written

as

$$\begin{aligned}\frac{\partial \chi_1^2}{\partial c} &= -2 \sum_{n=1}^N \frac{(y[n] - c - mnT)}{\text{var}(y)} = 0 \\ \frac{\partial \chi_1^2}{\partial m} &= -2 \sum_{n=1}^N \frac{nT (y[n] - c - mnT)}{\text{var}(y)} = 0\end{aligned}\quad (3.12)$$

The pair of simultaneous equations can be solved using Gaussian elimination to give an equation for  $m$  in terms of the data  $y$  and its variance  $\text{var}(y)$  [108]:

$$m = \frac{\sum_n \frac{1}{\text{var}(y)} \sum_n \frac{nTy[n]}{\text{var}(y)} - \sum_n \frac{nT}{\text{var}(y)} \sum_n \frac{y[n]}{\text{var}(y)}}{\sum_n \frac{1}{\text{var}(y)} \sum_n \frac{(nT)^2}{\text{var}(y)} - \left(\sum_n \frac{nT}{\text{var}(y)}\right)^2}.\quad (3.13)$$

Using the propagation of error and Eq (3.13), we find [108]

$$\text{var}(m) = \text{var}(y) \left(\frac{\partial m}{\partial y}\right)^2 = \frac{\sum_n \frac{1}{\text{var}(y)}}{\sum_n \frac{1}{\text{var}(y)} \sum_n \frac{(nT)^2}{\text{var}(y)} - \left(\sum_n \frac{nT}{\text{var}(y)}\right)^2}.\quad (3.14)$$

Since  $m = -1/T_1$ , then  $\text{var}(T_1) = \text{var}(m)/m^4$ .

The last step is to relate strain measurement variance  $\text{var}(y)$  to stress stimulus variance  $\text{var}(\sigma)$ . In Eq (3.1), we assumed  $\sigma(t) = \sigma_a$  for  $t > t_0$  was a constant. We now assume  $\sigma(t)$  is a normally distributed random variable  $\mathcal{N}(\sigma_a, \text{var}(\sigma))$  for  $t > t_0$ . From the definition of  $y$  above,

$$\text{var}(y) = \text{var}(\epsilon_0) \left(\frac{\partial y}{\partial \epsilon_0}\right)^2 + \text{var}(\epsilon_1) \left(\frac{\partial y}{\partial \epsilon_1}\right)^2 + \text{var}(\hat{\epsilon}) \left(\frac{\partial y}{\partial \hat{\epsilon}}\right)^2,\quad (3.15)$$

where the covariances in this case are zero. Since  $\epsilon_\ell = D_\ell \sigma_a$ , the variance in strain constants on the right side of Eq (3.15) can be related to stress variance via  $D_\ell$ , where we assume compliance is a deterministic property of the media. Consequently,

$$\text{var}(y) = \frac{\text{var}(\sigma)(D_0^2 + D_1^2) + \text{var}(\hat{\epsilon})}{(\epsilon_0 + \epsilon_1 - \hat{\epsilon})^2}.\quad (3.16)$$

Tests of Eq (3.16) using Monte Carlo simulations show that the uncertainty in the parameter  $T_1$  varies linearly with the input stress variance. The predictions of Eq (3.16) are compared with simulations in Fig 3.3. Thus closed form expressions may be obtained for simple models that can be linearized. For higher-order models, computational methods are required.

### 3.1.5 Gelatin Sample Preparation

A 5-cm cubic block of gelatin was prepared with a 0.8-cm-diameter cylindrical inclusion centered in the block as illustrated in Fig 3.4. The gelatin manufacturing process was described previously [57]. 26 ml of propyl alcohol and 13.5 g of type A, 275 bloom, animal-hide, gelatin (Fisher Scientific, Chicago, IL) were added to 200 ml distilled water to arrive at a 5.5% gelatin concentration by weight. The solution was heated at 60°C for ~30 min until visually clear before adding 0.3 ml of formaldehyde to increase collagen cross linking. 9.1 g of graphite powder was added to the molten gelatin and thoroughly mixed to provide tissue-like ultrasonic absorption and backscatter. For the inclusion, 20 g of gelatin powder (8% concentration by weight) was used. Since Young's modulus for gelatin gels is proportional to the square of concentration [57, 89], the inclusion was approximately  $(0.08/0.055)^2 = 2.1$  times stiffer than the background. Samples were stored at room temperature four days before measurements.

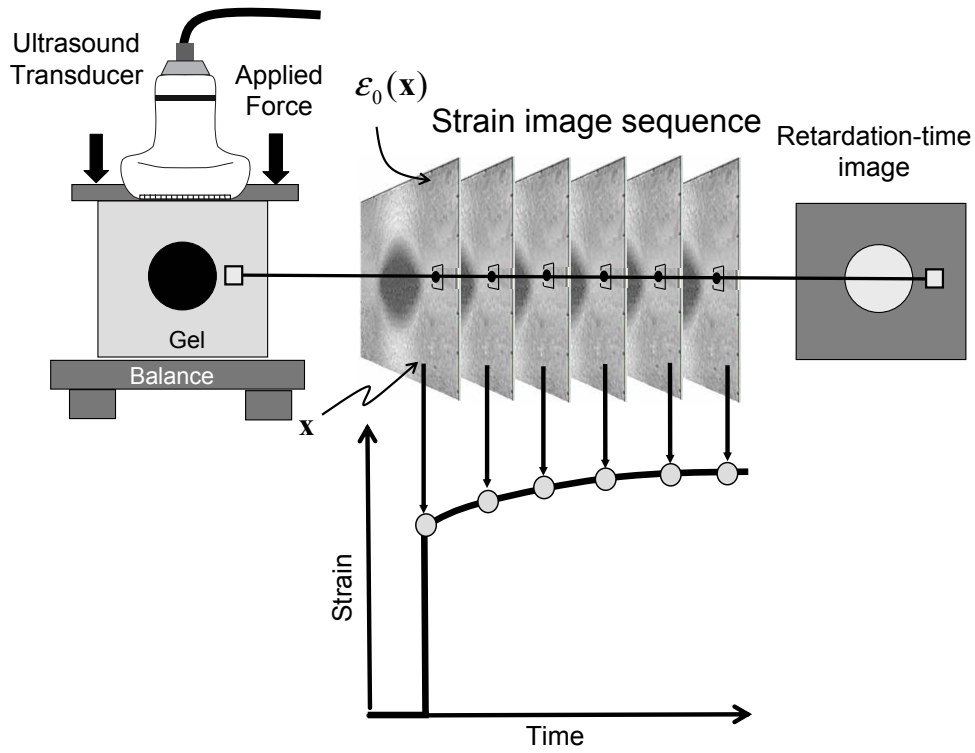


Figure 3.4: Imaging viscoelastic properties of a gelatin phantom. The object (left) is compressed from above and held while the ultrasound system records a series of RF echo frames from which a sequence of strain images (center) is computed. Pixels from the strain-image sequence are fit to viscoelastic models to compute  $T_\ell$  images (right).

### 3.1.6 Imaging Viscoelastic Properties

Data were acquired for imaging viscoelastic properties of gelatin phantoms by suddenly applying a force to the top surface of the cubic phantom while recording RF echo frames. Stress was applied using either a precise motion controller system or with free-hand techniques as described below.

### 3.1.6.1 Computer controlled stress.

A linear array transducer (Siemens Antares VF10-5 transmitting at 8 MHz) is flush mounted to a compression plate and positioned with a computer controlled motion system (Galil Inc., Rocklin CA) as depicted in Fig 3.4. A small pre-load is applied to establish contact with the phantom. Then a short-duration ( $\sim 1$  s) ramp stress of amplitude 500 Pa is applied along the direction normal to the top surface and held to initiate creep measurements. Using feedback from the balance (Denver Instruments Co., Model TR-6101, Denver CO), the final force is held constant over time. The effects of the ramp stimulus relative to a step stimulus are discussed in (Chapter 2) [1]. Mineral oil is applied to all exposed sample surfaces to minimize desiccation and allow contact boundaries to freely slip under a load.

Echo frames are recorded synchronous with the transducer motion at a rate between 1-4 fps for up to 2000 s. The URI feature of the Antares provides digitized RF-echo frames that can be triggered using an external waveform generator connected to the ECG trigger feature on the Antares. Since on-board memory is limited, multiple acquisitions bursts of 300 s were acquired and aligned using the time stamp on a recorded frame. An RF echo-data frame acquired just prior to applying the load at  $t = t_0$  becomes the reference to which subsequent RF frames acquired at discrete times  $t[n] = nT$  are recorded and strain images produced using constant reference multi-resolution cross correlation strain imaging techniques [27].

The sequence of strain images was analyzed using *Method I* to form parametric images of elastic strain  $\epsilon_0$ , retardance times  $T_\ell$ , viscous strain constant  $\sigma_a/\eta_0$ , and  $\chi^2$  from Eq

(3.4). Though  $\eta_0$  for gelatin is very large (Chapter 2) [1], the term cannot be neglected for the long acquisition times we employed.

### 3.1.6.2 Freehand stress.

Freehand experiments were the same as the motion controlled system described above except that forces were applied to the phantom by operators holding the transducer. Three operators participated by applying a constant force of approximately 5 N for 120 s with and without the help of force feedback. When feedback was permitted, operators were asked to keep a force plot constant while watching a real-time display.

## 3.1.7 Acquisition and processing parameters

Parameters such as ultrasonic frame rate, strain acquisition time, stress ramp time, and applied stress  $\sigma_a$  each have an effect on target contrast. We studied the effects of frame rate for gelatin previously (Chapter 2) [1] and found that frames rates  $\geq 1$  fps are adequate to sample the highest frequencies in the creep-response bandwidth of gelatin,  $\omega_{\max} \simeq 4$  rad/s. Acquisition time determines the frequency resolution and therefore the lowest measurable frequency. A 2000-s acquisition gives  $\omega_{\min} \simeq 0.003$  rad/s.

## 3.2 Results

Fig 3.5 shows Monte-Carlo simulation results for creep data generated via Section 3.1.3. A unimodal, log-normal  $L(\tau)$  distribution with mean 100 s and variable bandwidth

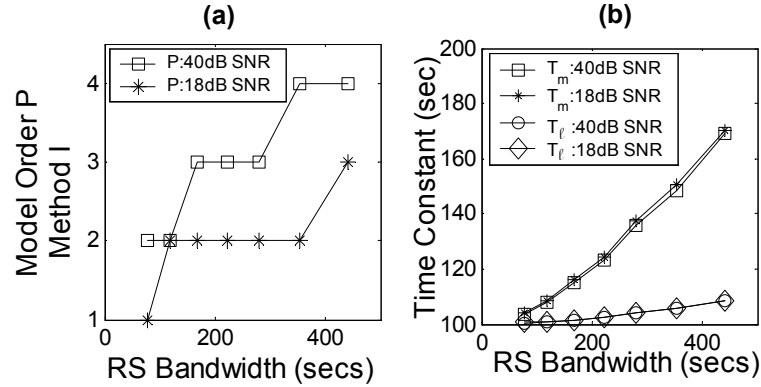


Figure 3.5: (a) Model order estimates from *Method I* for two SNR values, 18 dB and 40 dB, and varying  $L(\tau)$  bandwidth. (b) Corresponding values for  $T_m$  (*Method I*) and  $T_\ell$  (*Method II*). The input peak value is 100 s.

was input into the simulator. Results were measured for strain SNR equal to 18 dB and 40 dB, simulating imaging and non-imaging conditions, respectively. Although the model order for *Method I* varied with SNR, the weighted mean retardance time,  $T_m$ , did not vary appreciably with SNR. The mean retardance time for *Method I* increased with  $L(\tau)$  bandwidth much more than for *Method II*. With  $P = 1$ , *Method II* gave a bias in  $T_\ell$  less than 15% and also showed no significant dependence on strain SNR.

Methods I and II were next used to parameterize the experimental gelatin distribution in Fig 3.1. *Method I* yielded a  $P = 3$  model order for both cases although the number of peaks observed was two, consistent with the simulation results shown in Fig 3.5 for high SNR data.  $T_m$  values calculated for the second mode coincided with spectral peaks. *Method II* estimates for  $P = 2$  yielded values close to *Method I*  $T_m$  values with some overestimation of  $T_1$ . This is because of the restriction placed on the signal space, i.e., forcing  $P = 2$ . If more flexibility was given,  $P > 2$ , values coinciding with the peaks were obtained in addition to other low-medium amplitude poles. Assessing the importance of

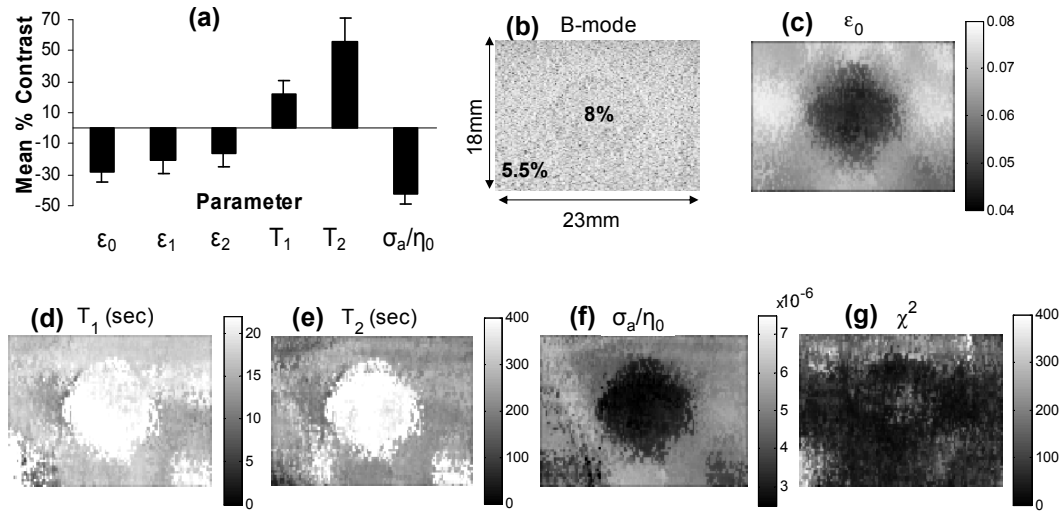


Figure 3.6: (a) *Method I* Mean % contrast for parametric images. Error bars denote 1 standard deviation of the mean. *Method I* images: (b) B-mode image showing 0.8 cm inclusion, (c) elastic strain image  $\epsilon_0$ , (d)  $T_1$  image, (e)  $T_2$  image, (f)  $\sigma_a/\eta_0$  image, and (g)  $\chi^2$  map using Eq (3.4).

each pole then becomes challenging.

Fig 3.6 shows parametric images obtained experimentally using *Method I* and the composite phantom. A uniaxial compression of 533 Pa was applied to the top of the phantom and held for 2000 s.  $P = 2$  was found per pixel for this imaging data (SNR = 15-20 dB). The elastic, viscoelastic and viscous components were estimated simultaneously. Since the  $\chi^2$  map displays low values and is relatively uniform, it seems the discrete model function of Eq (3.3) is representative of the creep data.

### 3.2.1 Retardance Time Images

Fig 3.6a shows a plot of the mean contrast for parametric images calculated from three separate acquisitions. Contrast for parameter  $X$  between the inclusion and background

regions is found from spatial averages of the parameter,

$$C_X = (\bar{X}_i - \bar{X}_b) / \bar{X}_b . \quad (3.17)$$

The mean contrast and standard deviation of the mean for three data sets with unequal uncertainties are [108]

$$\bar{C}_X = \frac{\sum_{k=1}^3 (C_X / \text{var}(C_X))_k}{\sum_{k=1}^3 1 / \text{var}(C_X)_k} \quad \text{and} \quad \text{std}(\bar{C}_X) = \left( \sum_{k=1}^3 1 / \text{var}(C_X)_k \right)^{-1/2} \quad (3.18)$$

Parameters  $\epsilon_0$ ,  $T_1$ ,  $T_2$  and  $\sigma_a / \eta_0$  provided the greatest target contrast for the phantom.

To check for consistency of our data with that in the literature, we made two comparisons. First, the measured value for elastic strain contrast  $\bar{C}_{\epsilon_0}$  was used to estimate strain contrast transfer efficiency for comparisons with predictions for this phantom geometry [109]. The contrast transfer efficiency is defined as  $\text{CTE (dB)} = 20(|\log(\bar{C}_{\epsilon_0} + 1)| - |\log(C_{E_0} + 1)|)$  where  $C_{E_0}$  is the Young's modulus contrast. We found that  $\bar{C}_{\epsilon_0}$  in Fig 3.6c is -0.305 as computed from Eq (3.17). Also since Young's modulus is proportional to the square of gelatin concentration, as described in Section 3.1.5,  $C_{E_0} = (0.08^2 - 0.055^2) / 0.055^2 = 1.11$  for our phantom. Therefore  $\text{CTE} = -3.3$  dB, which is close to the prediction of -3.1 dB reported by [109].

Another experimental study suggested that the viscosity of gelatin gels varies with gelatin concentration according to the power law  $\eta_0 \propto \text{Conc}^{1.1}$  [51]. The predicted contrast for our phantom, therefore, is  $(0.08^{1.1} - 0.055^{1.1}) / 0.055^{1.1} = 0.51$ , and the contrast observed from Fig 3.6f is 0.43. Given that there could be a loss of efficiency in transferring viscosity contrast into an image, as there is for strain, the agreement is reasonable.

Elastic strain patterns surrounding a stiff inclusion, as in Fig 3.6c, are strongly influenced by boundary conditions when quasi-static stress stimuli are applied. Stress concentration effects on strain patterns are well understood [110, 93]. However, the background patterns in the  $T_1$  and  $T_2$  images of Fig 3.6d,e are different, and in our broader experience they seem less dependent on boundary factors. The central bright regions in retardance time images are consistent with the inclusion region creeping slower than the background region because the higher density polymer increases the fluid viscosity and provides more inter-fiber hydrogen-bonded cross links [53].

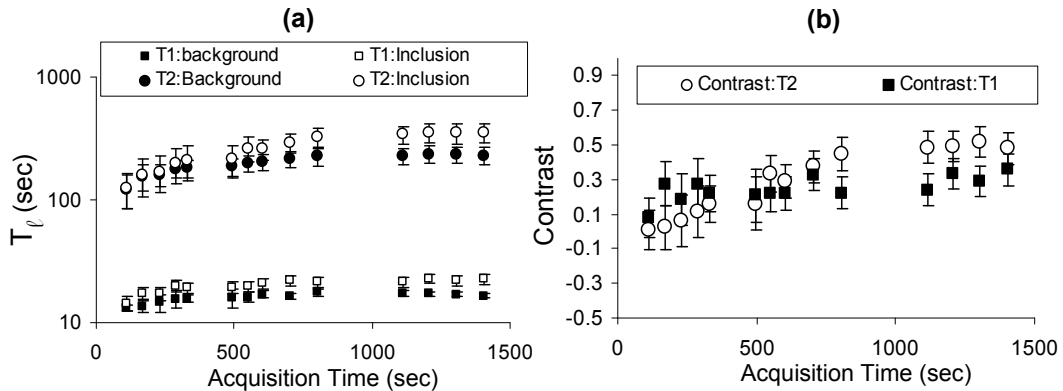


Figure 3.7: (a) Variation in retardance time estimates with acquisition time for *Method I* and a gelatin phantom. (b) Variation in retardance-time contrast with acquisition time.

### 3.2.2 Acquisition Time

Images in Fig 3.6 were estimated using *Method I* from data acquired over 1400 s, ensuring the parameters have stabilized. At shorter acquisition times, Fig 3.7a shows that parameters are underestimated. For gelatin, stable retardance times require acquisition times as large as 800 s. Since  $T_1$  and  $T_2$  are estimated simultaneously, stabilization times

are similar.

More importantly for imaging, we investigated the contrast in  $T_\ell$  images for gelatin phantoms; see Fig 3.7b.  $T_1$  image contrast stabilizes quickly for acquisition times greater than 120 s. However  $T_2$  contrast is negligible below about 300 s. It grows to 40% when the acquisition time  $T_a > 4T_2$ . The results need to be repeated for tissue imaging to guide scanning techniques. However preliminary results have shown that  $T_1$  in normal breast tissue is on the order of 3 s and  $T_2$  is of order 60 s [101], and the viscoelastic amplitudes  $\epsilon_1$  and  $\epsilon_2$  are several times greater than for gelatin. Together these findings help explain why we have been able to obtain  $T_1$  images in breast patient studies with 20 s acquisitions but not  $T_2$  [90].

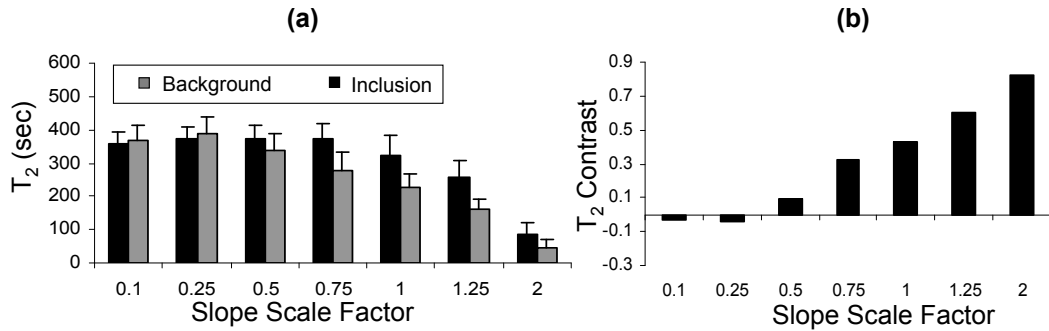


Figure 3.8: (a)  $T_2$  background and inclusion estimates at different scaled  $\sigma_a/\eta_0$  values (b) Corresponding contrast values.

### 3.2.3 Linear Viscous Creep

To generate the data in Fig. 3.7, we first eliminated the linear viscous term,  $\sigma_a/\eta_0$ , from the strain sequence of each pixel prior to estimating viscoelastic parameters. (See Fig. 3.6f.) Significant biases occurred if  $\sigma_a/\eta_0$  estimates were ignored or inaccurate. Fig. 3.8a shows

$T_2$  values estimated when the linear term was scaled up or down by the factor indicated on the abscissa. Underestimation of  $\sigma_a/\eta_0$  affects the background region surrounding the inclusion to a greater degree, resulting in a loss of  $T_2$  contrast, Fig. 3.8b. Overestimation of  $\sigma_a/\eta_0$  preserves contrast but underestimates  $T_2$  thus increasing image noise. Consequently,  $\sigma_a/\eta_0$  errors greatly affect  $T_2$  estimates.

The effects of  $\sigma_a/\eta_0$  on  $T_1$  can be less pronounced as seen in Fig. 3.9. Solid points are obtained when compensating for the linear term exactly and open points are uncompensated. No significant differences were found for acquisition times  $< 90$  s indicating that the linear term can be ignored. This is the range of most clinical imaging [75]. We assumed a first-order discrete model for these gelatin phantom measurements, resulting in stable  $T_1$  values for  $20 \text{ s} \leq T_a \leq 50 \text{ s}$  and biased estimates for longer acquisition times (Fig. 3.9). Unbiased estimates for acquisition times  $>90$  s are found by switching to a second-order model, as we did in Fig. 3.7a.

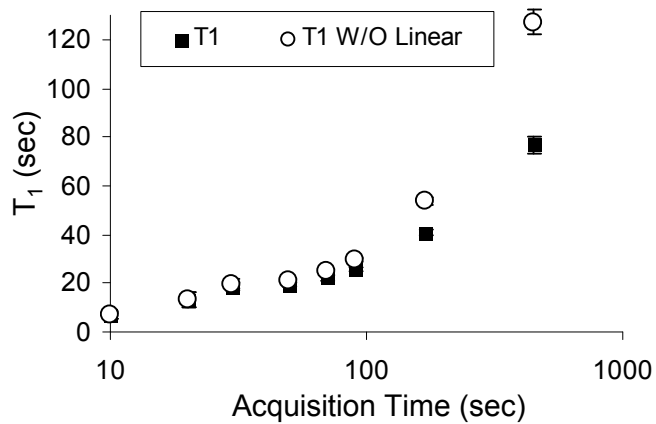


Figure 3.9:  $T_1$  variation over short acquisition times with and without compensating for linear viscous creep.

### 3.2.4 Stress variance

For all the data above, precise stresses were applied using a computer-controlled motion system. However, for a clinical setting, stresses need to be applied freehand. Fig 3.10a gives two examples of hand-held stress applied to a gelatin sample over time with and without the help of force feedback. With feedback, the stresses in the hold phase are steady except for the random variability seen. With no feedback, stresses are maintained for the first 60 s, after which some drift occurs.

Stress application errors were further quantified by measuring the variance of two volunteers attempting to hold an ultrasonic transducer while applying a constant 6 N force to the gelatin phantom (see Fig 3.10b). Volunteer 1 had no training and Volunteer 2 practiced more than 10 hours before measurement. Clearly both training and feedback can reduce the variance in the stress stimulus.

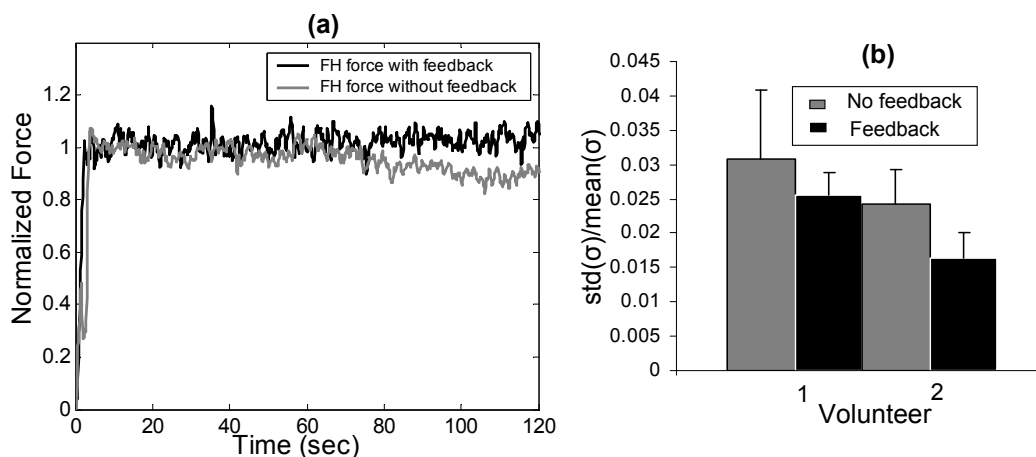


Figure 3.10: (a) Freehand force applied over time to a gelatin sample with and without feedback. (b) Relative stress variability as recorded from two volunteers that apply forces with and without feedback.

### 3.3 Discussion

The creep response from gelatin gels has been modeled as a sum of exponentials where the time constants are continuously distributed and bimodal, e.g., Fig. 3.1. The model agrees with experimental creep measurements and therefore suggests that a very broad range of retardance times delay the full strain response at each location in the medium. Therefore, as with any spectroscopic imaging technique, we have a very high dimensional feature space that must be reduced to a few key features to form images. Ferry [53] and Tschoegl [79] suggest that the bimodal distributions from gels reflect mean times at which two different internal structures relax. Our approach to viscoelastic imaging is to represent creep data as a second-order discrete Voigt model with two characteristic retardance times corresponding to the peaks of the bimodal retardance distribution.

Estimating viscoelastic properties in this manner is an ill-posed inverse problem. For example, we have generated broadband  $L(\tau)$  distributions as inputs into Monte Carlo simulations of creep data in noise (forward problem) and then attempted to estimate the distribution from the simulated data (inverse problem). Depending on the quality of our initial guesses at parameters using least squares methods (*Method I*, Table 3.1), the bandwidth of  $L(\tau)$ , and the strain SNR, the quality of the parametric estimates was highly variable. Limiting our interest to the peaks of the distribution (instead of attempting to back out the entire distribution) yields acceptable parametric precision and accuracy for imaging applications. *Method II* offers the advantage of providing SVD filtering for the strain data and model-based exponential estimation that can efficiently detect retardation times at or near

the distribution peaks. However, it too is sensitive to parametric initialization and requires the operator to select operational parameters (See Table 3.2). Considering the differences in computational load and the resulting parametric errors, this early stage of development provides no clear advantage of one method over the other.

A different approach to viscoelastic modeling that is gaining momentum models the constitutive equation as a fractional derivative [79, 95]. Instead of exponential time dependencies, strain retardation (or stress relaxation) is modeled as algebraic decays [111]. Mathematically, we use  $\epsilon_{ve}(\mathbf{x}, t) = D_1(\mathbf{x})\mathcal{D}^\alpha\{\sigma(\mathbf{x}, t)\}$  in place of Eq (3.3), where  $\mathcal{D}^\alpha$  is the fractional derivative operator applied to the stimulus and  $0 < \alpha < 1$ . The fractional derivative result is simplified in the Laplace domain as  $\tilde{\epsilon}_{ve}(\mathbf{x}, s) = D_1(\mathbf{x}) s^\alpha \tilde{\sigma}(\mathbf{x}, s)$ , and has the desirable feature of concise representation by two parameters:  $D_1(\mathbf{x})$  and  $\alpha(\mathbf{x})$ . Since both can vary with position, they are natural imaging parameters. As Schiessel and Blumen [111] show, the ladder models of a continuous retardation distribution are interpreted as series equations approximated by a fractional derivative. There is also a molecular basis for interpreting these parameters in polymer solutions [95]. However the interpretation in cross-linked polymeric solids with arrheodictic behavior, like gelatin and soft connective tissues, is still empirical in the sense that  $\alpha$  is a characteristic parameter not directly connected to molecular structures. Our proposal is to use  $T_1$  and  $T_2$  from second-order Voigt units (Eq (3.3)) as parameters describing, respectively, short-range fluidic structure and long-range entanglements of the polymer.

Our experience with viscoelastic imaging suggests that stimulus variability is a major

source of noise when applying freehand stimuli; that is, when applying a force to a sample by manually pressing the transducer into its surface. The results of Fig 3.3 and Eq. 3.16 show that  $T_1$  variability is linearly related to stress stimulus variability. Also, Fig. 3.10 provides an estimate of stress errors in free hand stress applications. Comparisons with predicted values indicate  $<12\%$  errors in  $T_1$  estimates.

The analysis of viscoelastic imaging developed in this chapter and the results in gelatin phantoms provide a framework for investigating creep properties of breast tissues for linear deformations. Images of elastic strain  $\epsilon_0$ , retardation times  $T_\ell$ , and linear viscous response  $\sigma_a/\eta_0$  form a concise feature set for investigation and may be interpreted in terms of the underlying polymeric structure.

## Chapter 4

# Viscoelastic Imaging on In-vivo Breast

## Tissue

Alteration of tissue mechanical properties due to disease has motivated the development of clinical elasticity imaging techniques [100, 5, 24] using phase sensitive modalities such as ultrasound or MRI. If tumor specific changes of the extra-cellular matrix is exploited, differential diagnosis of cancers is possible. For instance, during the formation of an infiltrating ductal carcinoma (IDC), mutated cancer cells transform local stromal cells (fibroblasts) through molecular signaling causing them to change phenotype and deposit large amounts of collagen and fibronectin that together stiffen tumors (*Desmoplasia*). This is accompanied by edema caused by a decrease in proteoglycan molecule [15] concentration, leaky vasculature and poorly functional lymphatics. Benign tumors on the other hand, such as fibroadenomas also stiffen due to increase in collagen production by normal

fibroblasts but are normal tissue, hence are associated with a proportional increase in proteoglycan content [15], resulting in tumors with different viscoelastic properties (stiff and viscous).

Mechanical properties of breast tumors can be measured by applying either external static [28] or dynamic [33, 63] excitations or using ultrasound-based radiation force [41, 62] methods. Data on the breast using external static methods has been limited to palpable masses, showing encouraging results for differentiating benign versus malignant on the basis of elastographic lesion contrast and size [73, 74, 30]. Malignant tumors most frequently appear significantly stiffer than surrounding tissue and larger than their sonograms; primarily from desmoplasia and edema. However, more recently, we explored [75] elasticity or strain on non-palpable masses and found that strain can be non-specific and can vary appreciably due to the dependence of tissue mechanical properties on the physiology [23] and tumor microenvironment [64] of a specific patient. Up till now, no measurements have been reported on the breast for quasi-static stimuli, i.e., viscoelastic properties of breast tissue to an external step-like stress stimulus has not been explored. We believe that by imaging viscoelastic properties in addition to just elastic properties, measured using static methods, the feature space for diagnosis can be broadened, making it possible to exploit more cancer-related changes. Other viscoelastic measurements on the breast using static or dynamic internal radiation force methods [63, 62] have shown differences in viscosity in addition to elasticity for malignant and benign masses indicating that tumor specific changes could be measured. These methods, however, require sophisticated instrumentation, high-intensity

pulses and may not be readily adopted as a screening procedure. Furthermore, it is unknown which type of stimulus (quasi-static, dynamic or radiation force) offers information that is most diagnostic and discriminative. Thus, we wish to determine whether simple external quasi-static methods can offer useful information about breast viscoelasticity.

In this chapter, we develop the science of in-vivo breast viscoelastic imaging using free-hand quasi-static stimuli from data acquired from 3 volunteers. First the feasibility of applying stimulus free-hand is addressed following measurements of breast tissue linearity, viscoelastic creep and creep-recovery. Particularly, aspects pertaining to stimulus effects and acquisition time are discussed. Imaging methods developed for tissue-mimicking hydrogels such as gelatin (Chapter 2 and 3) [1, 112] are used in breast studies and comparison between the two media are done where relevant. Gelatin was used previously in development of the imaging science primarily because of its tissue-like mechanical and acoustic properties [51, 52, 56, 86, 58, 57], simplicity and elastic uniformity within the resolution of the ultrasonic imaging system. Its creep response to quasi-static stimuli was well represented by linear viscoelastic theory up to large deformations and comprised of both solid and fluid polymeric features. Gelatin's creep retardance spectra was continuous and bi-modal with spectral bandwidth suggesting ultrasonic frame rates  $> 1$  fps and acquisition times  $> 2000$  s to sample its response effectively. We wish to understand/measure these criteria with in-vivo breast such that systematic future clinical measurements of time-varying mechanical behavior of breast masses could be conducted for possible differentiation/characterization. We also briefly summarize our recent clinical findings for a pilot

clinical study at the UC, Davis medical center.

## 4.1 Methodology

### 4.1.1 Volunteer Studies

#### 4.1.1.1 Positioning and data acquisition

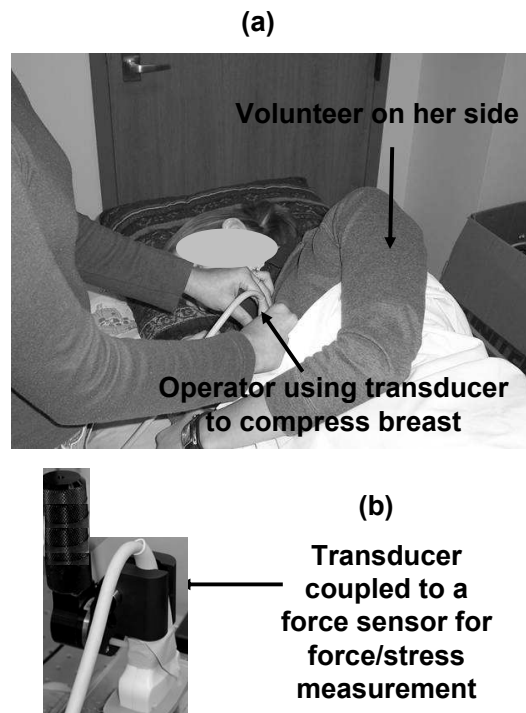


Figure 4.1: (a) Volunteer positioning for long-duration echo frame acquisitions (b) Coupling of transducer and force sensor when force measurement is made.

In gelatin studies (Chapter 2, 3) [1, 112], at least 2000 s of data was required so as to sufficiently sample the medium's response bandwidth. Shorter times resulted in underestimation of model parameters and inaccurate estimation of flow terms (Chapter 2) [1]. To

measure/understand the response bandwidth in breast tissue, the first step is to acquire data for as long as possible. One major disadvantage we face in doing so is the inability to use precise lab stress controllers to apply stimuli. Forces have to be applied freehand. Practice on large blocks of gelatin have revealed that it is possible to apply a quasi-static (ramp-and-hold) stimulus freehand quite accurately up to 200 s after some training and with the aid of a real-time force display (Chapter 3) [112]. Even if force application is possible freehand, data acquisition time is still severely limited by breath-hold time ( $<20$  s) of a volunteer if scanning is done with her lying supine (current protocol in clinical elasticity imaging). However, if the volunteer is rolled on her side while she is breathing shallowly, acquisition time is limited by the operators ability to maintain a steady force. This new position can allow for long acquisition times with minimal artifacts.

Fig 4.1a shows the positioning technique we use for data acquisition. Important aspects of the position is that the volunteer is completely on her side with her fore-arm folded below her breast for a boundary support. The operator compresses the breast in a direction parallel to the chest wall.

Tissue compression is applied using the transducer surface attached to a small rectangular compression plate manually or through a force sensor (ATI Industrial Automation, Apex, NC) mounted to the transducer (see Fig 4.1b) for comparison. The sensor measures the actual force applied to the breast in Newtons in the axial direction. 3 volunteers were asked to participate in the in-vivo studies.

Applying the positioning technique above, we conducted a variety of experiments.

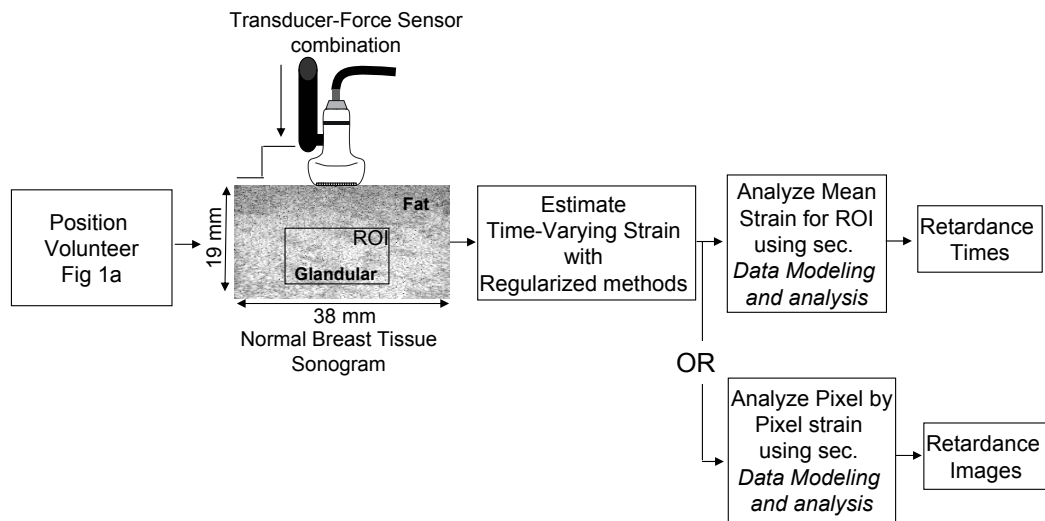


Figure 4.2: General protocol used for volunteer studies.

#### 4.1.1.2 Linearity Testing:

We applied freehand compressions to the breast using the transducer-sensor combination with a force between 1-20 N and recorded RF frames synchronously at 5 fps using the Siemens Antares system with Ultrasound Research Interface (URI) controlled by the ECG trigger. Sampling rate of the sensor is 10 samples /sec. Fig 4.2 shows the general protocol used. RF echo data obtained were then converted into displacement and strain images using an optical flow algorithm [59]. Strain estimates were then averaged over the  $1 \text{ cm} \times 2 \text{ cm}$  glandular breast region indicated and synchronized with the applied forces to plot a Force-Strain curve. Glandular regions are chosen as they are the primary sites of neoplastic growth and are regions where most often tumors grow. For comparison with breast, a similar force-strain experiment was done on a 5 cm square homogeneous gelatin

block and mapped alongside breast tissue results. The gel was manufactured according to the guidelines in (Chapter 2) [1].

#### **4.1.1.3 Creep Measurement:**

The above experiment helps to identify the range of linear responses in the breast if any. To measure creep, we apply ramp and hold stimuli freehand to the breast. Ramp time was  $\sim 1$  s and the force was held for up to 200 s during which time RF echo frames were recorded at 2 fps. Protocol in Fig 4.2 was then used to generate mean strain curves for the indicated glandular region. Measurements were repeated at least 3 times per volunteer. Larger loads were also applied to address differences.

#### **4.1.1.4 Imaging Creep:**

The above protocol of applying stresses and estimating strains was done with one small variation. No particular ROI's were selected and analysis was done pixel-pixel on the entire acquired region.

#### **4.1.1.5 Creep Recovery Measurement:**

The recovery of the tissue was also measured after creep by applying an initial free-hand load for about 100 s and later relieving it and holding it at baseline for another 100 s. Ramp times during compression and release were  $\sim 1$  s and data was analyzed according to Fig 4.2.

#### 4.1.1.6 Stimulus effects:

Effective force application could be achieved when the real time display of the force sensor was watched carefully especially during the hold phase. We investigated the changes in breast creep characteristics when feedback was not used or alternate feedback methods such as watching the real-time sonogram display was used with and without the sensor attachment to assess the importance of the force sensor.

### 4.1.2 Data Modeling and Analysis

#### 4.1.2.1 Constitutive Models

In the above imaging experiments, stress,  $\sigma(\mathbf{x}, t)$ , is the stimulus and strain,  $\epsilon(\mathbf{x}, t)$ , is measured, hence, compliance,  $D(\mathbf{x}, t)$ , is the material properties that relate the two. All three quantities can vary in space,  $\mathbf{x}$ , and time,  $t$ . If the stress field is suddenly applied in time, as given by the weighted unit-step function  $\sigma_a(\mathbf{x}) u(t - t_0)$ , where  $u(t) = 1$  for  $t \geq 0$  and 0 otherwise. The linear constitutive equation becomes

$$\epsilon(\mathbf{x}, t) = D(\mathbf{x}, t)\sigma_a(\mathbf{x})u(t - t_0). \quad (4.1)$$

Compliance may be broken down into the sum of three terms describing time-independent elastic, time-varying viscoelastic and purely viscous responses, respectively,  $D(\mathbf{x}, t) = D_0(\mathbf{x}) + D_{ve}(\mathbf{x}, t) + D_v(\mathbf{x}, t)$  for  $t > t_0$ .  $D_0(\mathbf{x})$ , is the elastic response commonly measured for breast elasticity imaging using static stimuli [73, 30, 75], is inversely related to the elastic modulus. The purely viscous response,  $D_v = t/\eta_0$ , depends on the compressive-

flow viscosity coefficient  $\eta_0$  and the magnitude of the applied stimulus  $\sigma_a$  (Chapter 2) [1]. If significant, it is estimated and eliminated prior to any further processing.

$D_{ve}$  is often modeled in the polymer-mechanics literature as a continuous distribution of exponentially increasing strains each with retardance time  $\tau$  weighted by the distribution  $L(\tau)$  [53, 79, 82]. The expression is

$$D_{ve}(\mathbf{x}, t) = \int_{-\infty}^{\infty} d \ln \tau L(\mathbf{x}, \tau) [1 - \exp(-(t - t_0)/\tau)] , \quad (4.2)$$

where  $d \ln \tau = d\tau/\tau$ .

Hence,  $D_{ve}$  summarizes material properties of the medium that determine the amplitude and duration of the delayed strain in a creep response. Each time constant  $\tau$  is weighted by a corresponding compliance amplitude to give  $L(\tau) = \tau D'_{ve}(\tau)$ . Since  $D_{ve}(\mathbf{x}, t)$  varies spatially in heterogeneous media, each position can have its own  $L(\mathbf{x}, \tau)$  distribution that form a basis for viscoelastic imaging. We can approximate retardance-time distributions  $L$  from time-varying data using methods described by Tschoegl [79].

#### 4.1.2.2 Parameterizing Creep Data

Since creep data from polymers (Chapter 2) [1, 53] and biological tissues [77] reveal broad continuous distributions of retardance times, we need to extract meaningful parameters from the data that parameterize retardance distributions. Estimating parameters that line up with spectral peaks in the typically uni- and bimodal distributions that correspond to different molecular-scale processes seems to be a reasonable method for reducing dimensionality to just one or two parameters. We estimate discrete  $\tau$  values associated with peaks

Table 4.1: Algorithm for Data Parameterization

1. Estimate  $L(\tau)$  from the time-varying strain data of a creep experiment.
2. Record the number of peaks in  $L(\tau)$  as the number of modes  $M$ .
3. Model the strain response using Eq (4.3) and compute  $\chi^2$  and its probability  $Q$  estimates via equations developed in (Chapter 2, 3) [1, 112].
4. The order of the model is the lowest value of  $P$  for which  $Q > 0.1$ . Matlab function LSQCURVEFIT is used for fitting.
5. If  $P > M$ , identify the peaks associated with each distribution mode and compute the weighted mean  $T_m = \sum_{\ell}(\epsilon_{\ell}T_{\ell})/\sum_{\ell}\epsilon_{\ell}$  as the time constant for the mode.

in  $L$  by approximating the continuous distribution in Eq (4.2) with low-order discrete Voigt units (Chapter 2) [1, 79]. Since, spatially varying stresses,  $\sigma(\mathbf{x}, t)$ , is normally unavailable, we work with  $\epsilon(\mathbf{x}, t)$  instead of  $D(\mathbf{x}, t)$ . Specifically, for  $t > t_0$ , the  $P$ th-order discrete model is

$$\begin{aligned}\epsilon_{ve}(\mathbf{x}, t) &= D_{ve}(\mathbf{x}, t)\sigma_a(\mathbf{x}) \\ &= \sum_{\ell=1}^P \epsilon_{\ell}(\mathbf{x}) [1 - \exp(-(t - t_0)/T_{\ell}(\mathbf{x}))].\end{aligned}\quad (4.3)$$

Candidate parameters are viscoelastic strain amplitudes  $\epsilon_{\ell}$  and retardance time constants  $T_{\ell}$ , the latter corresponding to values of  $\tau$  at peaks of  $L$ . Using a statistical  $\chi^2$  model fitting method (details in (Chapter 3) [112]) that is based on spectral peak detectability, we fit breast creep data to the above equation for increasing Voigt model order  $P$  and pick the lowest order that satisfies a statistical  $\chi^2$  fitting criteria (Chapter 3) [112]. The specific algorithm used is reproduced from (Chapter 3) [112] and highlighted in Table-4.1. To obtain retardance time images, the above method is applied pixel-by-pixel.

#### **4.1.2.3 Effects of acquisition time**

Our experiences with gelatin hydro polymers guides the manner in which we process data. For instance, plotting the estimates over acquisition time ensures stability of values, model order correctness and also assesses whether the entire response bandwidth of the breast was sampled. We have shown previously, (Chapter 3) [112], that short acquisition times of  $<800$  s for long time gelatin data causes underestimation in parameters and contrast. We determine the effects of acquisition time on the breast creep data acquired.

#### **4.1.3 Pilot Patient Study**

The methods developed for volunteers were then applied on patients in a pilot UC, Davis elasticity/viscoelasticity study. Patients that present with suspicious breast masses on mammograms and sonograms were recruited and consented according to IRB guidelines. The scanning protocol involved the patient being supine or propped up slightly as necessary, while the breast mass was located by an experienced sonographer. This position often allowed for best lesion visibility but significantly reduced acquisition times. A quick compression was applied free-hand using a linear array transducer attached to a small compression plate and held for as long as the patient could hold her breath.

For cases wherein the lesion was visualized clearly while the patient was on her side, the acquisition times were increased. Strain and retardance time-constant images were estimated and interpreted based on histological information available after a biopsy.

## 4.2 Results

### 4.2.1 Volunteer Results

**Linearity Testing:** The constitutive equations developed in Sec. *Data Modeling and Analysis* has the inherent assumption of linearity. Hence it was important to determine the stimulus range that gives a linear response in breast tissue. Example freehand compressions of different amplitudes using force sensor attachment (see Fig 4.1b) applied for the purpose of linearity testing are shown in Fig 4.3. Strain estimated from these forces according to Fig 4.2 are then plot in a force-strain curve.

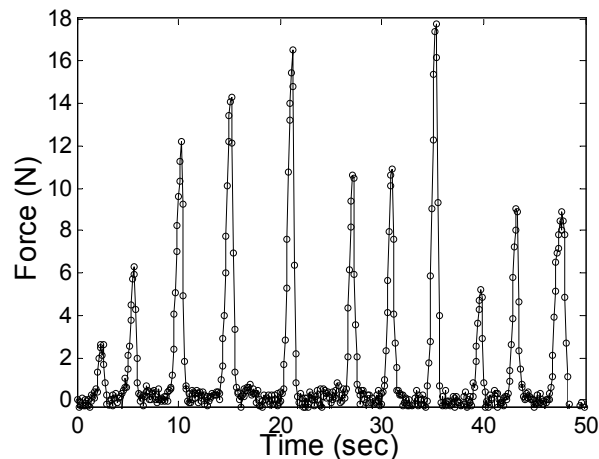


Figure 4.3: Freehand force application to breast using transducer-sensor combination for linearity testing.

Fig 4.4 shows results from two linearity experiments conducted on a volunteer breast. The response is clearly nonlinear over the 20 N range of force when compared with gelatin that is linear over the same range. Curves from the two experiments are not significantly different from each other and can be well described by an exponential fit. Similar force-

strain behavior was seen by [113]. If we focus on the range of forces between 2 and 5 N or 0.01 - 0.04 strain, we find the breast response to be approximately linear. For example, see the expanded view in Fig 4.5 where the correlation coefficient for a linear fit is  $R^2=0.82$ .

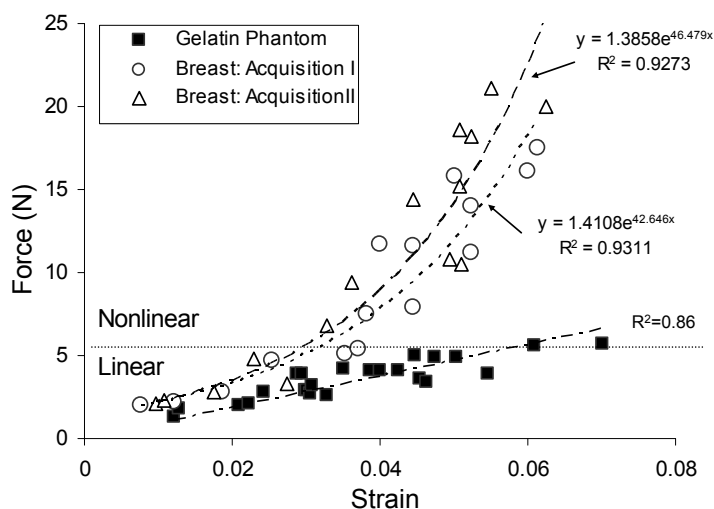


Figure 4.4: Force-strain curves for 2 breast tissue acquisitions. Mean strain was calculated for the region-of-interest indicated in Fig 4.2.

**Creep Measurements:** Based on the linearity results, we applied freehand ramp and hold stresses with a total applied force  $<5$  N to the breasts of volunteers to estimate creep curves. Fig 4.6a, b shows an example of free-hand force application using the force sensor attachment (see Fig 4.1b) and estimated creep curves. From the results, clearly it is possible to apply a ramp and hold force that is steady for up to 200 s. In this case force feedback from a real-time display was used.

As long as the applied force was less than 5 N, the creep data was arrheodictic, i.e., strains reached steady state around 100 s. Arrheodicticity in gelatin was noted only at extremely small stresses (3 Pa (Chapter 2) [1]). Parameterizing this data using the guidelines

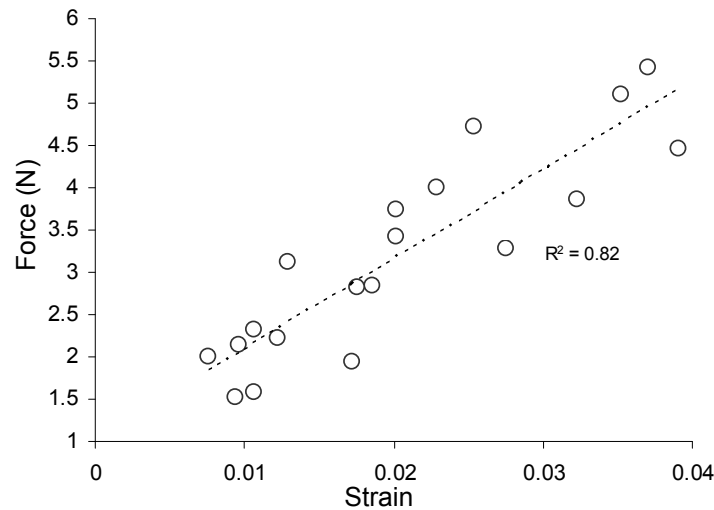


Figure 4.5: Force-strain curves for forces between 2-5 N for visualization of the linear regime of breast tissue.

from Table-4.1. yields two retardance time constants of 4.24 and 26 s, indicating that creep responses in normal breast tissue is short lived. Gelatin time constants were on the order of 1-10 s and 100-700 s. One important thing to note is that the amplitude of the creep is equal to or larger than the elastic amplitude. In gelatin the ratio was less than 0.1. Consequently the SNR for creep measurements is significantly larger in breast tissue than in gelatin. Creep curves obtained from other acquisitions with the same volunteer showed similar characteristics with average values for  $T_1=3.2\pm 0.8$  s and  $T_2 = 42\pm 28$  s. Thus we need 1-2 minutes of acquisition time to sample the entire response bandwidth of breast tissue.

Fig 4.7a, b show example creep curves when the applied force  $>5$  N (larger loads). We see a non-settling of the curves and a possible engaging of rheodicticity (a linear viscous term) at rates 0.01% and 0.03% strain/sec. Due to non-linear effects, the linear slope value

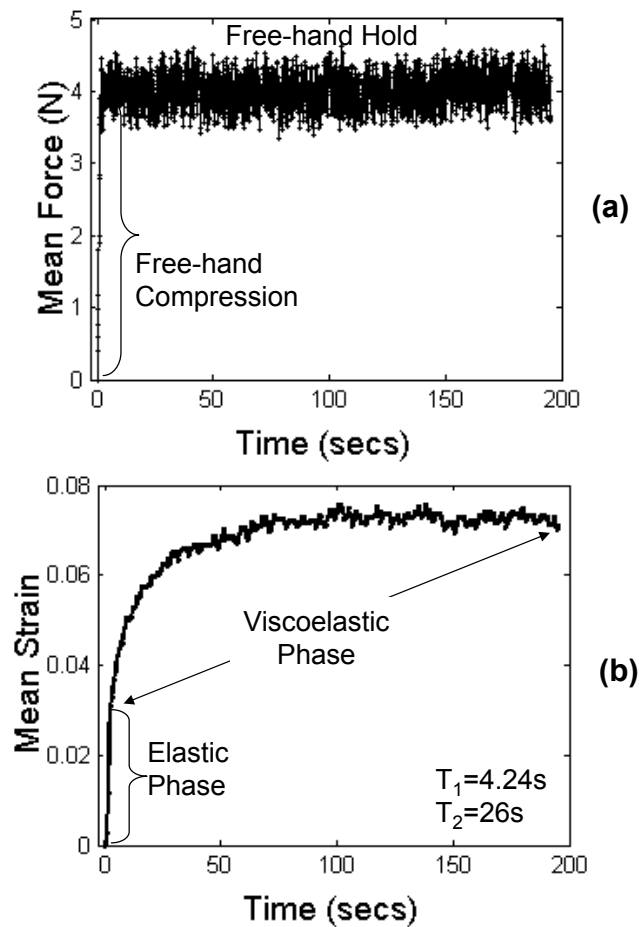


Figure 4.6: (a) Ramp and hold freehand force applied to the breast for up to 200 s. (b) Creep response over time.

varies with applied stress. For gelatin, rheodicticity engaged at stresses  $> 30$  Pa (Chapter 2) [1] with viscous slope values being invariant to the applied stress. These values varied only with gelatin concentration (change in stiffness). The oscillation seen on the curves is due to volunteer breathing motion. This regular motion however does not distort the curve significantly.

#### Creep Recovery Measurements:

The recovery characteristics after creep resembles the behavior of solid cross-linked

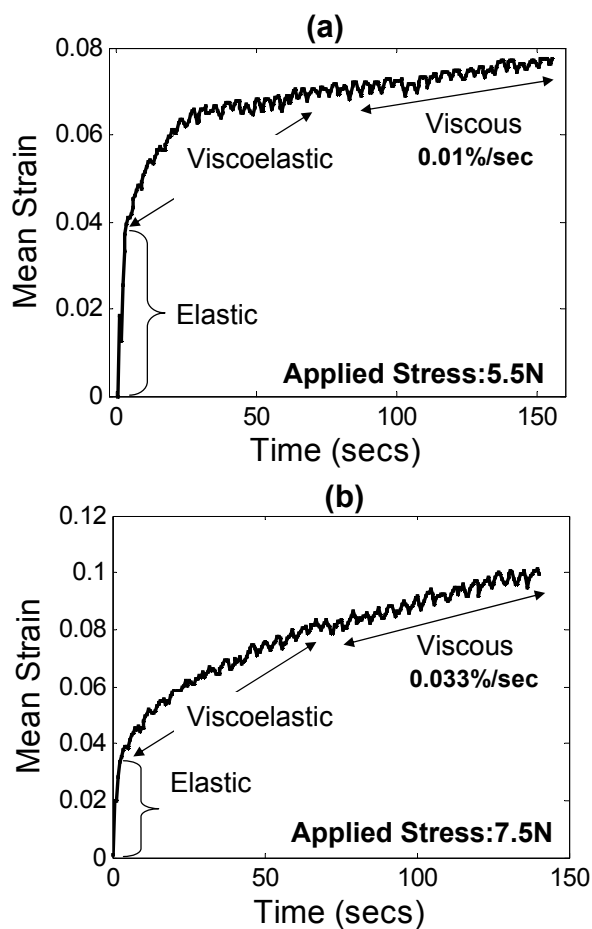


Figure 4.7: Creep response over time for (a) 5.5 N and (b) 7.5 N applied force.

polymers [53]. Fig 4.8 shows force and strain curves obtained from a such an experiment. A ramp force is applied, then held for  $\sim 100$  s, brought back to about zero and held in that position for again  $\sim 100$  s. The creep curve settles around 90 s and is almost completely recoverable in the relaxation phase showing strong similarities between breast tissue and other hydro polymers solids.

#### Stimulus effects:

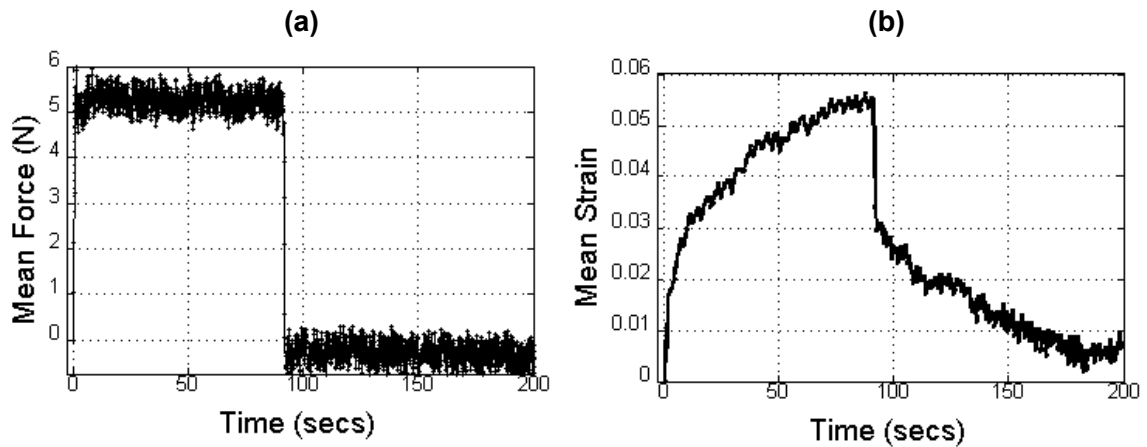


Figure 4.8: (a) Creep-Relaxation experiment applied to the breast over 200 s. (b) Creep-Relaxation response over time.

For Fig 4.6, the real-time force display was watched closely during force application. Given the high SNR obtained for breast creep curves (see Fig 4.6b), we wish to determine the impact of systematic stimulus errors on the response. For instance, when no feedback was used, input force varied but not substantially (see Fig 4.9a). This did not distort creep characteristics significantly. In fact, retardance time constants estimated still fell in the same range of times (see Fig 4.9b). On the other hand, if the real-time sonogram display on the ultrasound scanner was watched while applying the force, i.e., keep speckle steady on the monitor, the applied force was slightly under-compensated (see Fig 4.9c). Again this kind of stimulus application did not have a significant impact on the shape of the creep curve. Retardance times were estimated as 1.52 and 57 s. When the sensor was not used and only a transducer with plate was the compression device, the creep characteristics again did not get altered significantly (see Fig 4.9e). Hence, small systematic errors in force application do not significantly alter the creep response or our parameters of interest.

However larger errors that cause the tissue to move out of the plane will result in de-correlation errors.

### **Spectral Analysis:**

Creep data estimated from ramp and hold stimuli is used to generate retardance spectra,  $L(\tau)$ , according to guidelines in (Chapter 2) [1]; first to identify the number of modes which reflect breast tissue's prominent microstructural mechanisms occurring and secondly as a guide for data parameterization. Fig 4.10 show example spectra for breast tissue. This is mapped alongside spectra of gelatin reproduced from (Chapter 3) [112] for comparison. Closely comparing spectra there are similarities and differences. Breast spectra like confined gelatin spectra is also clearly bi-modal although deformation was done with no confinement. The spectral bandwidth is much narrower indicating mechanisms are short-lived and the entire response bandwidth can be accessed with much shorter acquisition times ( $\sim 100$  s). Bandwidths were much broader in gelatin and required 1400-2000 s of acquisition to access the entire bandwidth. Thus, although ultrastructurally breast tissue and gelatin are quite different their spectra have many similarities. The similarities in spectra could suggest similar underlying mechanisms supporting the theory of entanglement coupling proposed for high molecular weight, weakly cross-linked polymers with bi-modal behavior (Chapter 2) [1].

We next parameterize these retardance distributions using the method described in Table-4.1. Model order achieved for breast tissue is  $P = 2$  with  $T_\ell$  values approximately coinciding with the peaks. On the other hand, gelatin data yielded  $P = 3$ , but the weighted

mean of times indicated by ‘x’ coincided with peaks.

### **Effects of acquisition time:**

Looking at the breast spectra in Fig 4.10, it is clear that we acquire enough data, (200 s in this case), to sample the entire response bandwidth of breast tissue for the stimulus applied. In clinical situations, often only 10-20 s of data can be acquired due to lesion position, hence, acquisition times are severely limited. Hence we wish to address the variation of parameters and contrast over acquisition time for normal breast tissue to understand the loss of information for truncated acquisitions. We noted previously that shorter acquisition times underestimate parameters of interest as well as contrast for gelatin gels (Chapter 2, 3) [1, 112].

Fig 4.11a shows a sonogram of normal breast tissue with the top hypoechoic layer of fat and lower hyperechoic glandular layer. Fig 4.2 was the protocol used to generate the strain image series due to the applied ramp and hold stimulus. We next parameterize the data pixel by pixel using the guidelines in Table-4.1 to map retardance time images. Shown in Fig 4.11b is the  $T_1$  image for breast. Fat regions seem to relax faster than glandular region possibly due to the lower collagen content. Similar contrast was found with gelatin when a high concentration gel inclusion was embed in a low concentration gel background (Chapter 3) [112]. Fig 4.11c shows the variation of  $T_1$  and contrast over acquisition time for small regions selected in fat and glandular areas. Here contrast is defined as the difference in the time constant value between glandular and fat regions or  $(T_{1g} - T_{1f})/T_{1g}$ . We see that fat tissue has a shorter retardance time value of 7 s when compared to glandular tissue

that is 17 s. These values are stable after 30 s and 100 s respectively. At shorter times underestimation is seen. Contrast is stable and maximum around 50 s. Shorter times cause its underestimation as well.

#### 4.2.2 Patient Studies

We compare the above volunteer results to one case of a clinical acquisition (see Fig 4.12) and map  $T_1$  values in the lesion and background. The patient was supine on her back and asked to hold her breath for the length of the acquisition. The mass seen in the sonogram was histologically identified as a fibroadenoma. We see background values are stable very soon but lesion values continue to rise. Similarly, due to the truncated acquisition time, contrast is still rising and not stable yet. Hence  $T_1$  image contrast can be enhanced greatly if the acquisition time is increased.

Other interesting points to note are: (1) elastic strain contrast is subtle with size in the strain image similar to that of the sonogram and (2)  $T_1$  contrast is positive, i.e, we see brightening in the lesion area for this case. This subtlety in strain contrast with similar size for such benign masses was noted by other groups like Hall *et.al* [30] for palpable masses. However they also found significant strain contrast and larger sizes for malignant lesions, again for palpable masses. We [75] found that strain contrast actually could be non-specific for malignancies as seen in Fig 4.13. This figure is reproduced from [75]. Strain contrast varies from being very dark, to almost no contrast, to brightening. We believe that this variability is due to the dependence of strain contrast on the underlying

tumor-microenvironment and physiology of a particular patient. By the addition of retardance time images into the feature space of diagnosis, there could be better specificity for malignancies. For instance,  $T_1$  retardance images appear to lengthen for benign masses when compared the shortening seen in malignant lesions (see Figs 4.14 and Fig 4.15). Lengthening of the time constant was also noted with gelatin when a high concentration gel inclusion was placed inside a low concentration gel background (Chapter 3) [112]. We think that the contrast seen is consistent with the changes in the extra-cellular matrix that occur during the formation of these tumors. For instance, for benign tumors, there is an increased production of collagen with a proportional increase in proteoglycan content which causes increased structuring of water around collagen fibers increasing tissue viscosity. On the other hand, shortening in malignant lesions could be possibly due to edematous effects. Thus adding retardance time constant imaging to the feature space of elasticity imaging could help in diagnosis and differentiation of benign and malignant breast tumors.

### 4.3 Discussion

The use of external quasi-static stimuli is a relatively simple and safe way to engage a large amplitude, high SNR viscoelastic response in breast tissue. Some training with real-time visual aids allow for efficient free-hand stimulus application up to 200 s or more with the length of the data acquisition depending on volunteer comfort in the new side scanning position, operators ability to hold steady and the on-board memory of the ultrasound scan-

ner for the combination of parameters chosen (depth of penetration, frame rate and lateral resolution).

Stress/force stimuli that resemble step or pulse functions engage creep and creep recovery respectively. The window for linear responses is small, between 2-5 N, wherein linear viscoelastic modeling techniques can be used. In this range, breast creep closely resembles the response of solid polymers. Beyond 5 N, other components are noted in the response; a purely linear term possibly due to fluid flow appears to be added to the exponential curve at rates between 0.01-0.03 %strain/sec. This fluid behavior was noted in gelatin gels at significantly lower stresses.

Elimination of fluid effects is necessary before any spectra is taken allowing for comparisons between gelatin and breast. Fig 4.10 shows that both media present with two modes with breast spectra more similar to gelatin spectra with its boundaries confined. The clear modal separation indicates that underlying mechanisms occur one after another [94] with the high frequency mode representing short-range movements of collagen fibers in viscous fluids and the low frequency mode occurring due to the lateral movement of peptide chains through a tangled matrix. Since this bi-modality is a common feature to high molecular weight weakly cross-linked polymers [53], could the similar spectra we see for both media reflect similar underlying mechanisms for viscoelastic behavior?

Data parameterization using low-order rheological models allows extraction of values that line up with spectral peaks thus offering a summary of observed mechanical behavior and indicating mean times at which mechanisms occur. Other models such as the fractional

derivative model [95] or the QLV models [77] may very well fit the response, however, our main aim of modeling is to obtain a meaningful parameter set that reflects the underlying tissue structure - key to expanding the diagnostic feature space. Hence retardance times with the knowledge of elastic behavior offer a concise summary of observed behavior.

Creep measurements can be done with good repeatability and its high SNR offers some immunity to small systematic errors in force. For instance, if a sophisticated force sensor is unavailable, just the transducer attached to a small compression plate can be used to compress the tissue while using feedback from the real-time sonogram display. The newer scanning methods established for volunteers offer an opportunity to acquire echo data for longer duration with minimal breathing artifacts. The resultant increased temporal information when parameterized using linear rheological methods offers unbiased parameters that reflect the underlying structure of the tissue. This scanning position may be however feasible only for a sub-population of patients whose lesions can be visualized and compressed using this method.

In limited breast patient studies of nonpalpable lesions, only 10-15s of creep data was obtained. First-order models fit to the data yield average time constants for malignant lesions to be shorter than surrounding tissue. Opposite effects or lengthening of the time constant was noted in fibroadenomas. These were noted in cases when elastic strain in the nonpalpable lesions was variable and not discriminatory. Hence, clinical application of viscoelastic imaging may offer a unique manner in which tumors can be differentiated and characterized.

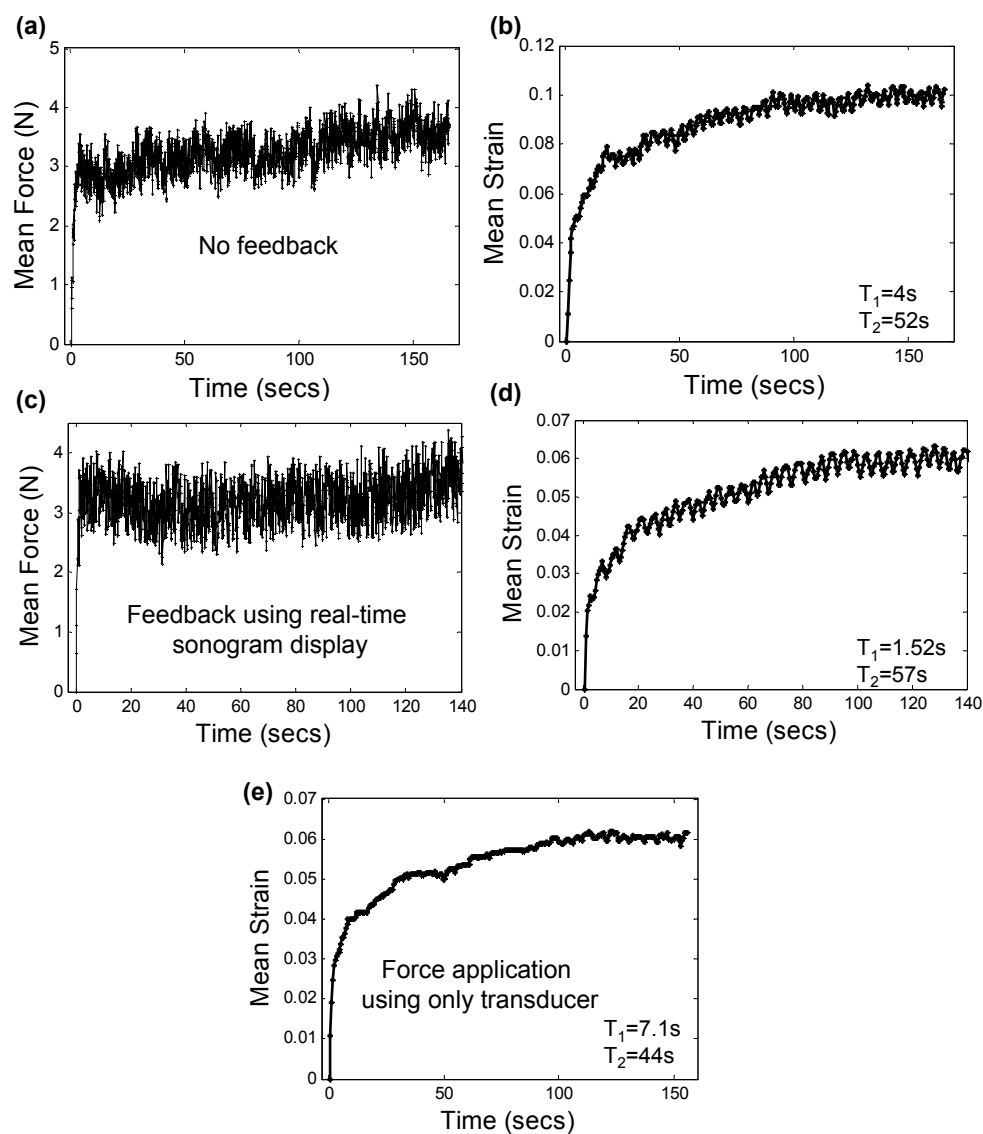


Figure 4.9: Freehand force applied to the breast with transducer-sensor combination. Plotted alongside are estimated creep curves. (a-b) no force feedback (c-d) real-time sonogram feedback (e) Creep estimated when only transducer with plate was used as the compression device.

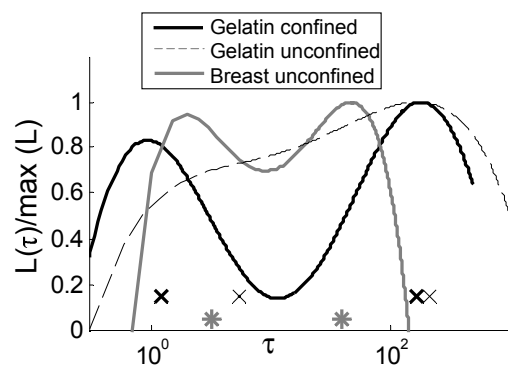


Figure 4.10: Retardance spectra for breast tissue. Spectra mapped alongside gelatin spectra reproduced from [20]. Markers on the  $\tau$  axis indicate retardance times in accordance to Table-4.1. '\*' indicates no weighting whereas 'x' indicates weighting.

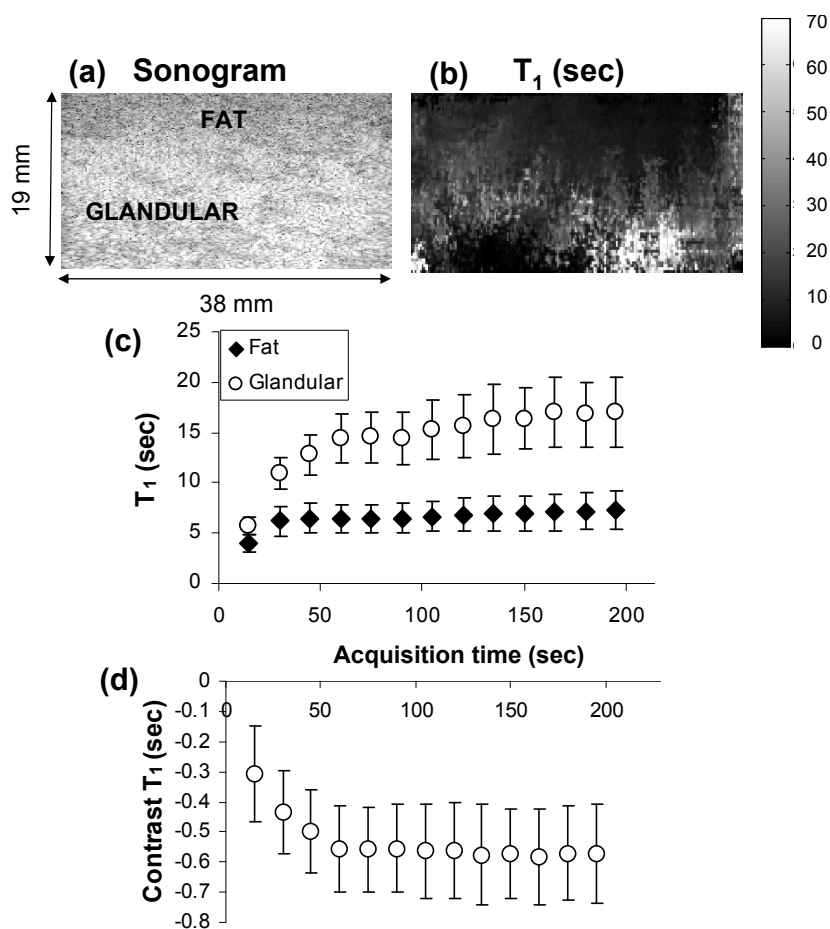


Figure 4.11: (a) Sonogram (b)  $T_1$  image of normal breast tissue. (c) Variation of retardance times in fat and glandular regions over acquisition time (d) Variation of contrast between glandular and fat regions over acquisition time.

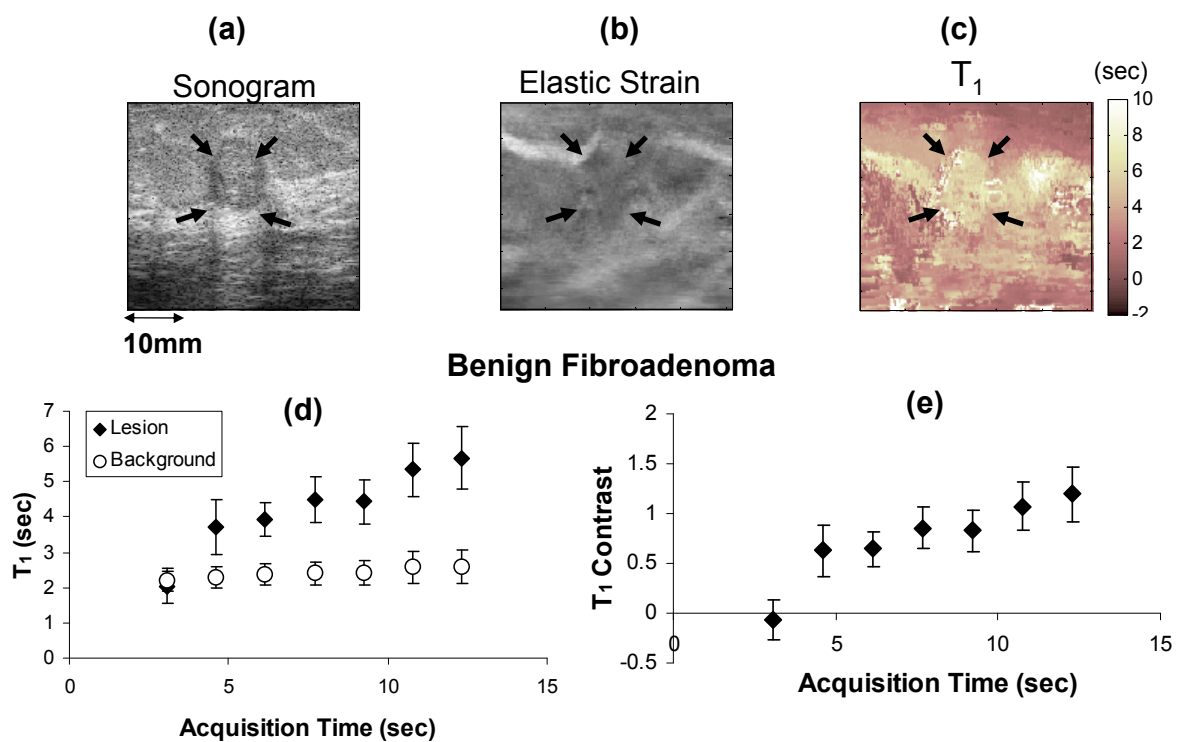


Figure 4.12: (a) Sonogram (b) Elastic strain  $\epsilon_0$  (c)  $T_1$  image (d) Variation of  $T_1$  over acquisition time for lesion and background areas (e) Variation of contrast over acquisition time. Mass histologically determined as a fibroadenoma.

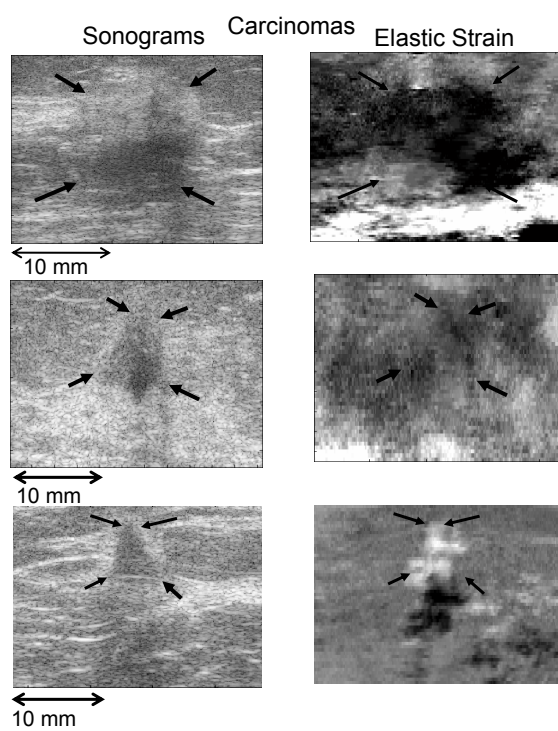


Figure 4.13: Sonograms and elastic strain  $\epsilon_0$  images of malignant carcinomas. Reproduced from Barakat *et. al.*

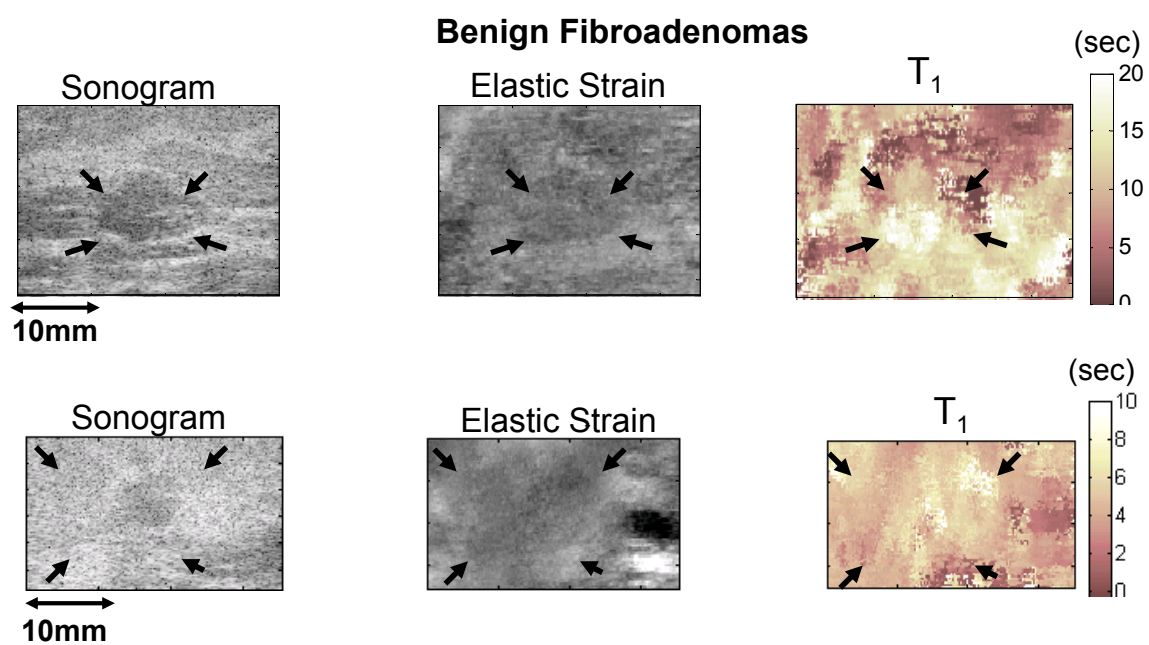


Figure 4.14: Sonogram, Elastic strain  $\epsilon_0$  and  $T_1$  images for 2 cases of benign fibroadenomas.

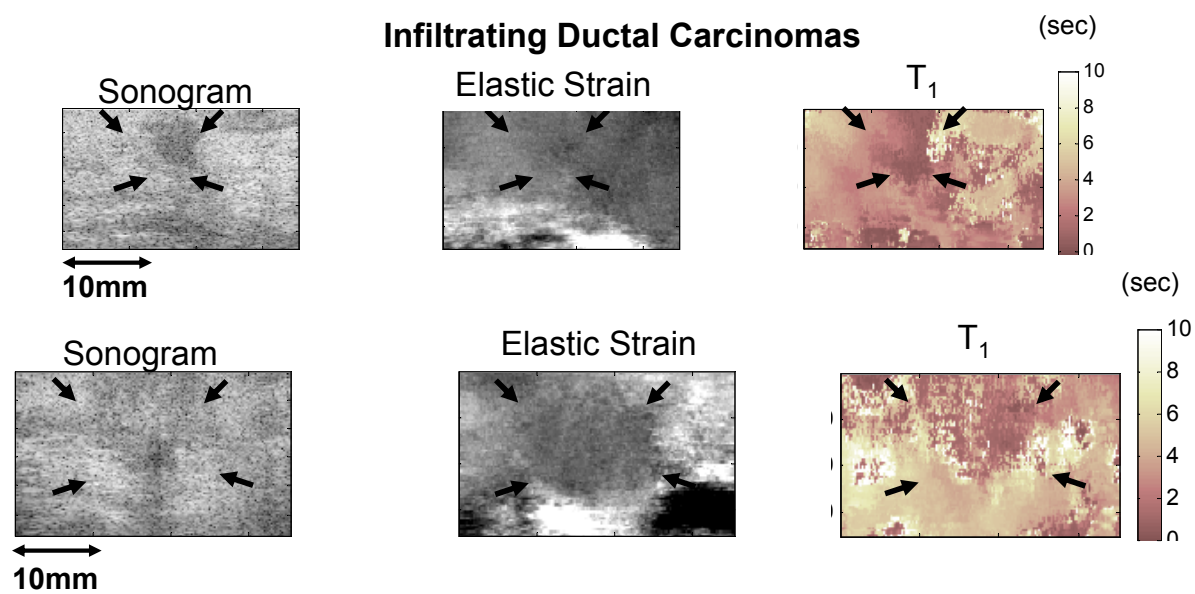


Figure 4.15: Sonogram, Elastic strain  $\epsilon_0$  and  $T_1$  images for 2 cases of malignant ductal carcinomas.

## **Chapter 5**

### **Overall Discussion and Conclusions**

In this dissertation, new ultrasound technologies that image mechanical or viscoelastic properties have been developed without contrast enhancement with the long term goal of enhancing cancer specific diagnostic information. Extensive testing and evaluation of the technique has been done with tissue-mimicking gelatin hydro-polymers and preliminary measurements on in-vivo breast tissue of volunteers and patients have been conducted. By applying an external-quasi static stimulus, that resembles a step function, displacements and strains were tracked precisely using ultrasound at diagnostic frequencies and at high resolution to reflect time varying viscoelastic features of a medium. Throughout this work, specific aims listed in Chapter 1 have been thoroughly investigated. In this chapter, results are discussed briefly in an overall discussion section for each specific aim and then conclusions are made.

## 5.1 Overall Discussion

### 5.1.1 Spectra and Data parameterization

In specific aim (1) the task was to describe a medium's response to a quasi-static stimulus using parameters that reflect underlying mechanisms and microstructure. The approach taken in this dissertation involved the use of continuous and discrete linear viscoelastic models. Representing viscoelastic responses of gelatin with continuous models allowed for continuous spectral determination. Spectra described the medium's response over a large bandwidth as a distribution of response times. This allowed for visualization of primary modes responsible for viscoelastic behavior. For instance, clear bi-modal spectra was seen with high molecular weight gelatin when confined geometries were used. These modes arise from short range movements of collagen peptide chains in the viscous fluid and from the slow movement of these chains in the matrix ('entanglement coupling'). In both short duration (fluid) and long duration (matrix) responses, mechanisms normally vary in strength due to underlying collagen matrix randomness giving rise to continuous distributions of response times rather than discrete events. Experiments with uniaxial unconfined or confined geometries were bi-modal with sample confinement appearing to separate and narrow the distributions. Shear measurements on the other hand, displayed a larger low frequency matrix response and highly attenuated fluid effects.

The spectra played a crucial role in guiding acquisition protocols. The frame rate of the ultrasound system was tuned such that sufficient temporal resolution was provided to

sample the medium's high frequency viscoelastic response bandwidth without aliasing. Length of data acquisition was also chosen to be long enough so that the low-frequency spectral response was sampled adequately. Long acquisition times also helped in accurate estimation of purely viscous terms for subsequent removal. With gelatin 2000s of data was acquired at a rate of 1-4 frame/sec for visualization of the entire response bandwidth.

Such continuous spectral responses that reflect underlying time-scales for mechanisms guide modeling of data. Given that high molecular weight gelatin presents with 2 modes for uni-axial measurements, two data modeling techniques (least square methods using  $\chi^2$  criteria (Method I)) and state-space methods (Method II)) were developed that used discrete rheological models; comprising of sums of exponentially rising terms with associated amplitudes. Parameters output by the least square techniques did depend on the quality of the initial guesses, spectral bandwidth and signal-to-noise ratio (SNR) of the data; normally exceeding the number of modes for high SNR data. By limiting interest to the peaks of the distributions, weighted averages of response times yielded values coinciding with peaks in the spectra. On the other hand, state-space methods were robust in the presence of noise due their SVD filtering step.

They used model-based exponential estimation techniques and efficiently detected response times at or near distribution peaks. Such methods were however sensitive to parametric initialization and required the operator to select operational parameters. Hence, both methods use low-order discrete rheological models and output parameters that coincided with spectral peaks; reflecting mean times for mechanisms occurring in the medium

for the quasi-static stimulus. Parameters do not directly provide physical descriptions of polymers but rather are parsimonious summaries of viscoelastic behavior that help establish a concise feature space for viscoelastic imaging.

Thus, spectral responses from high molecular weight gelatin hydro-polymers are continuous, bi-modal and associated with broad bandwidth where peak location and width of spectral modes depend upon boundary conditions. From spectral descriptions, retardance times  $T_1$  and  $T_2$  corresponding to spectral peaks in addition to elastic strain  $\epsilon_0$ , form a concise feature space for viscoelastic imaging of gelatin. These retardance times reflect mean times at which fluid based and matrix responses occurs in the medium due to the applied stimulus.

### **5.1.2 Viscoelastic measurements**

In specific aim (2) the task was to validate parameters obtained with quasi-static stress stimuli with other measurements with known geometries. Gelatin gels were subjected to shear and uniaxial (creep, stress relaxation, oscillatory and indentation) experiments. These gels were found to be linear over a large range of applied stresses when stress-strain uniaxial compressions were done, with the extent of linearity expanding for stiffer media. In shear, linearity was tested by determining whether spectra scaled by the stress increase; stresses below 30 Pa engaged linear responses. While comparing parameters, elastic strain or modulus estimates agreed within 6% among the 5 experiments. Equilibrium compliances and steady-state viscosity from creep and stress relaxation experiments were also not statisti-

cally significantly different from each other. Poisson's ratio experiments revealed that these gels behaved elastically initially, resembling an incompressible solid, i.e.,  $\nu(0) \simeq 0.5$ , but within 100 s, equilibrium value of 0.473 was achieved, indicating that bulk compliance effects could no longer be neglected. Consequently, retardance times in compression and shear could not be directly compared.

Shear creep experiments using a rheometer were particularly interesting for basic measurements given the gold-standard geometry with these devices. Stresses as low as 3 Pa could be applied to visualize polymer solid behavior (arrheodicticity or strain settling) in gelatin. This could not be visualized with other geometries. At 30 Pa, gelatin's behavior mimicked a viscoelastic polymer saturated in a viscous fluid due to the presence of a linear term in the data, representing purely viscous fluid flow in the polymer. Measurements of this linear term (or  $1/\text{steady-state viscosity}$ ) was constant above a stress threshold, although the values did depend on gelatin concentration and type of gelatin (A or B). In general, steady-state viscosity was measured as  $\sim 10^8$  Pas (or the slope of the compliance curve:  $\sim 10^{-8}$ ), indicating that unbound fluid motion was extremely small. However data fitting required rheological models to include this term for un-biased estimates. Creep-recovery experiments also confirmed the presence of this linear term by settling to a constant value during recovery. Values for viscosity during creep and recovery closely matched.

Thus gelatin gels can be modeled up to large stresses with linear viscoelastic theory. They have solid polymer features with fluid behavior at high stresses. Their instantaneous elastic behavior resembles an incompressible medium ( $\nu(0) = 0.5$ ,  $E = 3G$ ) after which

they behave as compressible media ( $\nu(\infty) = 0.473$ ,  $B \neq 0$ ). Their viscoelastic responses in confined and unconfined geometries can be modeled nicely using generalized Voigt and Maxwell units with experimental behavior agreeing closely with analytical derivations. Estimated instantaneous and steady state parameters could be compared among shear and uniaxial experiments, however, actually comparison of retardance times could not be done given the presence of bulk features at long times.

### **5.1.3 Sources of uncertainty affecting contrast**

In specific aim (3) the task was to quantify the sources of interference and uncertainty that alter contrast and parameter estimates. To model fibrotic tumors, a high gelatin concentration inclusion was placed in a low concentration gel surrounding medium. An imaging experiment involved a quasi-static stress stimulus and synchronous strain estimation using ultrasound at high frame rates and for long acquisition times. Each spatial location in the imaging sequence represented a continuous spectra resulting in a high dimensional problem. However, since our interest is primarily in spectral peak locations, least square methods were used to extract these values and were mapped into retardance time images. These images reflect mean times at which two different internal structures relaxed. Since the central inclusion differed in gelatin concentration from its background, strain and retardance time contrast was generated. Negative contrast for strain and viscosity was found and positive contrast for time images. Values of strain contrast scaled appropriately with changing gelatin concentration in accordance to contrast transfer efficiency curves reported

in the literature.

Three sources altered contrast - data acquisition time, estimation of the linear term and stimulus variability. Contrast and parameters were underestimated when data acquisition time was truncated. For gelatin,  $T_2$  images were more affected than  $T_1$ . In fact, 800 s of data was required for stable  $T_2$  contrast. Significant biases in  $T_2$  parameters occurred if the linear term was ignored or inaccurate with greater errors for soft regions (background) than stiff areas (inclusion). Up to 50% underestimation and 100 % overestimation could be tolerated to maintain  $T_2$  contrast. Effects of the linear term were less pronounced on  $T_1$  with no biases for short acquisition times,  $< 90$  s, indicating that it could be ignored in this range (clinical imaging acquisition time scales). For in-vivo tissue, magnitude of stress stimulus could be used to control the engaging of the viscous response, thereby decreasing errors due to its estimation. Furthermore, acquisition time data on tissue yielded steady contrast at 50 s, significantly shorter than gelatin. This decrease in the requirement of acquisition time is due to breast tissue's large amplitude, fast changing and short lived response when compared to gelatin. Hence, even 10 s of data will result in some contrast in breast tissue, however no significant contrast was seen in gelatin at these times. Another source of error is the stimulus random variability during freehand applications. Analytically this error was quantified to be linearly related to  $T_1$  uncertainty.  $T_1$  predicted errors were within 12-15% when training and feedback was used for free hand applications.

Thus, during imaging experiments spectral responses must be used to assess the required data acquisition time for stable parameters and contrast. Furthermore this long time

data also helps in efficient assessment of the linear term whose accuracy will maintain contrast. With freehand clinical experiments, good training and practice with force feedback will help reduce stress variability thereby decreasing retardance time errors.

#### **5.1.4 In-vivo feasibility and methodology**

In specific aim (4), the task was to establish in-vivo feasibility for viscoelastic imaging and develop acquisition methodology for volunteers and patients. The first task was to determine whether a quasi-static stress could be applied freehand. Large gelatin samples were used to practice on, and with adequate training and feedback, stresses could be maintained steady except for random variability due to hand motion for up to 200s. Similar results were also seen when experiments were done on volunteers in a new scanning position that allowed for maximum data acquisition with minimal breathing artifacts. Interestingly, this external quasi-static stimuli engaged a large amplitude ( $VE/E > 1$ ), high SNR viscoelastic response in breast tissue that closely resembled solid polymer behavior when forces  $<$  than 5 N were applied. The window for linear responses was narrow, between 2-5 N, consequently linear viscoelastic modeling techniques could be applied. Beyond 5 N, the linear term appeared in the data at rates between 0.01-0.03 %strain/sec. Gelatin gels required much smaller stresses to engage this behavior but was associated with small viscoelasticity ( $VE/E < 0.1$ ).

200 s of data was sufficient to visualize the spectral response bandwidth for breast for the stimulus. Spectra revealed a bi-modal response with clear peaks and narrower band-

width when compared to gelatin. Since this bi-modality was a common feature among both media and characteristic to high molecular weight weakly cross-linked polymers, similar underlying mechanisms could be responsible for viscoelastic behavior. Data parameterization using low-order rheological models estimated  $T_1$  and  $T_2$  as 4s and 26s for one case of acquisition indicating that times for mechanisms in breast tissue are much shorter than gelatin. In-vivo repeatability for creep measurements was high and small systematic errors in force was tolerable given the high SNR response.

Thus, with newer scanning methods established for volunteers, data acquisition time could be extended an order of magnitude thereby decreasing biases related to acquisition times. Initial clinical feasibility of the technique is encouraging showing differences in benign and malignant retardance time contrast. The contrast is consistent with ECM changes that occur during tumor formation. For instance, the shortening of  $T_1$  time constant in malignant cases could be consistent with edema present whereas long  $T_1$  values reflect increased viscosity consistent with upregulation of collagen and associated proteoglycan molecules. Thus viscoelastic imaging techniques using quasi-static stimuli may offer a unique manner in which tumors can be differentiated and characterized.

## 5.2 Conclusions

A novel method of imaging viscoelastic properties using external quasi-static stimuli has been developed by exploiting the unique capability of ultrasound for detecting tiny

motion. Technique requires no contrast enhancement, is safe, relatively simple, in-vivo feasible and maps a concise set of images - elastic strain,  $\epsilon_0$  and viscoelastic retardance time,  $T_\ell$ . Elastic strain is a measure of stiffness where as retardance times reflect time scales of underlying viscoelastic mechanisms due to the stimulus, hence images are indicative of the microstructure. Gelatin hydro-polymers is a good investigational medium for image development due to its simplicity, ease of manipulation and excellent ultrasonic and mechanical characteristics. Although, ultrastructurally gelatin and breast are different, similarities in spectral and viscoelastic responses at low loads allows it to be adopted as a physical model for breast. Sophisticated modeling techniques and spectral analysis developed for gelatin can then be applied to breast tissue once assumptions are tested. In gelatin, magnitude of viscoelasticity is approximately 10% of the visualized elastic response and retardance times are in the range of 1-15 s and 100-400 s, where values depend on boundary conditions, gelatin concentration and age of the sample. Retardance times are obtained using least square methods and are values that coincide with spectral peak locations to represent primary time scales for observed viscoelastic behavior. This method requires up to twice the approximate value of the time constant to provide stable contrast and values. In-vivo measurements using free-hand stimulus application is very feasible after operator receives adequate training and visual aids for force application. Furthermore, the magnitude of viscoelasticity in breast is on the order of the elastic response associated with large amplitude, high signal-to-noise ratio and quick settling ( $\sim 100$  s) with no fluid interferences when loads are kept low. This type of response allows for high tolerance to small system-

atic changes in stimulus application. Values of the time constants in breast are:  $3.2 \pm 0.8$  s and  $42.0 \pm 28$  s;  $T_2$  values significantly shorter than in gelatin. This allows for shorter acquisition times (50-100 s) to obtain stable values and contrast. While contrast can still be visualized between 10 - 15 s with current scanning techniques, newer side positioning techniques will increase data acquisition and information content an order of magnitude. Preliminary viscoelastic imaging on patients revealed similar strong responses with retardance time contrast indicating possible cancer specificity - shortening in malignant lesions and lengthening in benign masses. Thus viscoelastic imaging techniques using quasi-static stimuli could offer a unique manner of non-invasive cancer characterization and differentiation.

## Bibliography

- [1] M. Sridhar, J. Liu, and M. Insana, "Elasticity imaging of polymeric media," *ASME J. Biomech. Eng.* (In print).
- [2] *American Cancer Society* : <http://www.cancer.org>, 1599 Clifton Road NE, Atlanta, GA.
- [3] T. Kolb, J. Lichy, and J. Newhouse, "Comparison of the Performance of Screening Mammography, Physical Examination, and Breast Ultrasound and Evaluation of factors that influence them: an analysis of 27,825 patient evaluations," *Radiology*, vol. 225, pp. 165–175, 2002.
- [4] S. Fields and F. Dunn, "Correlation of echographic visualizability of tissue with biological composition and physiological state," *J Acoust Soc Am*, vol. 60, pp. 1409–1412, 1976.
- [5] J. Greenleaf, M. Fatemi, and M. Insana, "Selected methods for imaging elastic properties of biological tissues," *Annu. Rev. Biomed. Eng.*, vol. 5, pp. 57–78, 2003.
- [6] L. Franks and N. Teich, *Cellular and Molecular Biology of Cancer*. New York: Oxford University Press, 1997.
- [7] F. Lizzi, M. Ostromogilsky, E. Feleppa, M. Rorke, and M. Yaremko, "Relationship of ultrasonic spectral parameters to features of tissue microstructure," *IEEE Trans Ultrason Ferro Freq Contrl*, vol. 34, pp. 319–329, 1987.
- [8] M. Insana, R. Wagner, D. Brown, and T. Hall, "Describing small-scale structure in random media using pulse-echo ultrasound," *J. Acoust. Soc. Am.*, vol. 87, pp. 179–192, 1990.
- [9] M. Insana, L. Cook, M. Bilgen, P. Chaturvedi, and Y. Zhu, "Maximum-likelihood approach to strain imaging using ultrasound," *J Acoust Soc Am*, vol. 107(3), pp. 1421–34, 2000.
- [10] M. Stoeckelhuber, P. Stumpf, E. Hoefter, and U. Welsch, "Proteoglycan-collagen associations in the non-lactating human breast connective tissue during the menstrual cycle," *Histochem. Cell. Biol.*, vol. 118, pp. 221–230, 2002.

- [11] H. Lodish, A. Berk, P. Matsudaira, C. Kaiser, M. Krieger, M. Scott, S. Zipursky, and J. Darnell, *Molecular Cell Biology*. New York: W.H. Freeman and Co., 2004.
- [12] B. Elenbaas and R. Weinberg, "Heterotypic signaling between epithelial tumor cells and fibroblasts in carcinoma formation," *Exp Cell Res*, vol. 264, pp. 169–184, 2001.
- [13] W. Gordenne, F. Malchair, B. Nusgens, and C. Lapiere, "The composition of connective tissue in the normal and fibrocystic breast [article in French]," *J Gynecol Obstet Biol Reprod (Paris)*, vol. 14, pp. 27–31, 1985.
- [14] P. Carmeliet and R. Jain, "Angiogenesis in cancer and other diseases," *Nature*, vol. 407, pp. 249–257, 2000.
- [15] G. Losa and M. Alini, "Sulphated proteoglycans in the extracellular matrix of human breast tissues with infiltrating carcinoma," *Int. J. Cancer*, vol. 54, pp. 552–557, 1993.
- [16] P. Schedin and A. Elias, "Multistep tumorigenesis and the microenvironment," *Breast Cancer Research*, vol. 6, pp. 93–101, 2004.
- [17] P. Dayton, D. Pearson, J. Clark, S. Simon, P. Schumann, R. Zutshi, T. Matsunaga, and K. Ferrara, "Ultrasonic detection of alphavbeta3 expressing-cells with targeted contrast agents," *Mol. Imaging*, vol. 3, pp. 125–134, 2004.
- [18] D. Sipkins, D. Cheresch, M. Kazemi, L. Nevin, M. Bednarski, and K. Li, "Detection of tumor angiogenesis in vivo by alphavbeta3-targeted magnetic resonance imaging," *Nat. Med.*, vol. 4, pp. 623–626, 1998.
- [19] D. Sullivan, "Challenges and opportunities for in vivo imaging in oncology," *Technol. Cancer Res. Treat.*, vol. 1, pp. 419–422, 2002.
- [20] P. Winnard and V. Raman, "Real time non-invasive imaging of receptor-ligand interactions in vivo," *J. Cell Biochem.*, vol. 90, pp. 454–463, 2003.
- [21] C. Abbey, A. Borowsky, E. McGoldrick, J. Gregg, J. Maglione, R. Cardiff, and S. Cherry, "In vivo positron-emission tomography imaging of progression and transformation in a mouse model of mammary neoplasia." *Proc. Natl. Acad. Sci. USA*, vol. 101, pp. 11 438–11 443, 2004.
- [22] S. Voytik-Harbin, B. Rajwa, and J. Robinson, "Three-dimensional imaging of extracellular matrix and extracellular matrix-cell interactions." *Methods Cell Biol*, vol. 63, pp. 583–597, 2001.
- [23] J. Lorenzen, R. Sinkus, M. Biesterfeldt, and G. Adam, "Menstrual-cycle dependence of breast parenchyma elasticity: estimation with magnetic resonance elastography of breast tissue during the menstrual cycle," *Invest. Radiol.*, vol. 38, pp. 236–240, 2003.

- [24] T. Krouskop, T. Wheeler, F. Kallel, B. Garra, and T. Hall, "Elastic moduli of breast and prostate tissues under compression," *Ultrason. Imaging*, vol. 20, pp. 260–274, 1998.
- [25] J. Mai and M. Insana, "Strain imaging of internal deformation," *Ultrasound Med Biol*, vol. 28, pp. 1475–1484, 2002.
- [26] F. Kallel and M. Bertrand, "Tissue elasticity reconstruction using linear perturbation method," *IEEE Trans. Med. Imag.*, vol. 15(3), pp. 299–313, 1996.
- [27] P. Chaturvedi, M. Insana, and T. Hall, "2-D Companding for Noise Reduction in Strain Imaging," *IEEE Trans. Ultrason. Ferroelec. Freq. Control*, vol. 45, pp. 179–191, 1998.
- [28] J. Ophir, I. Cespedes, H. Ponnekanti, Y. Yazdi, and X. Li, "Elastography: A Quantitative Method for Imaging the Elasticity of Biological Tissues," *Ultrasonic Imaging*, vol. 13, pp. 111–134, 1991.
- [29] J. Ophir, G. B. Alam, SK, F. Kallel, E. Konofagou, T. Krouskop, and T. Varghese, "Elastography: ultrasonic estimation and imaging of the elastic properties of tissues," *Proc. Instn. Mech. Engrs.*, vol. 213(H), pp. 203–233, 1999.
- [30] T. Hall, Y. Zhu, and C. Spalding, "In-vivo real-time freehand palpation imaging," *Ultrasound in Med. and Biol.*, vol. 29(3), pp. 427–435, 2003.
- [31] D. Regner, G. Hesley, N. Hangiandreou, M. Morton, M. Nordland, D. Meixner, T. Hall, M. Farrell, J. Mandrekar, W. Harmsen, and J. Charboneau, "Breast lesions: evaluation with us strain imaging—clinical experience of multiple observers," *Radiology*, vol. 238(2), pp. 425–437, 2006.
- [32] N. Nitta, T. Shiina, and E. Ueno, "Quantitative Assessment and Imaging of Viscoelastic Properties of Soft Tissues," in *Proc. IEEE International Ultrasonics Symposium*, ser. 078037582, 2002, pp. 1885–1889.
- [33] R. Lerner and K. Parker, "Sonoelasticity Imaging," *Acoustic Imaging*, pp. 317–327, 1988.
- [34] L. Taylor, B. Porter, D. Ruben, and K. Parker, "Three Dimensional Sonoelastography: principles and practices," *Phys. Med. Biol.*, vol. 45, pp. 1477–1494, 2000.
- [35] L. Sandrin, M. Tanter, S. Catheline, and M. Fink, "Shear modulus imaging with 2-D transient elastography," *IEEE Trans. Ultrason. Ferroelectr. Freq. Control*, vol. 49, pp. 426–446, 2002.
- [36] G. Torr, "The acoustic radiation force," *Am. J. Phys.*, vol. 52, pp. 402–408, 1984.

- [37] T. Sugimoto, S. Ueha, and K. Itoh, "Tissue hardness measurement using the radiation force of focused ultrasound," in *Proc. IEEE International Ultrasonics Symposium*, ser. 3, 1990, pp. 1377–1380.
- [38] A. Sarvazyan, O. Rudenko, S. Swanson, J. Fowlkes, and Y. Emelianov, "Shear Wave Elasticity Imaging: A New Ultrasonic Technology of Medical Diagnostics." *Ultrasound Medicine Biology*, vol. 24, pp. 1419–1435, 1998.
- [39] J. Bercoff, M. Tanter, and M. Fink, "Supersonic Shear Imaging: A new technique for soft tissue elasticity mapping," *IEEE Trans. on Ultr. Ferro. and Freq. Contr.*, vol. 51(4), pp. 396–409, 2004.
- [40] M. Fatemi and J. Greenleaf, "Vibro-acoustography: An imaging modality based on ultrasound-stimulated acoustic emission," *Proc. Natl. Acad. Sci.*, vol. 96, pp. 6603–6608, 1999.
- [41] ———, "Ultrasound stimulated vibro-acoustic spectrography," *Science*, vol. 280, pp. 82–85, 1998.
- [42] S. Chen, M. Fatemi, and J. Greenleaf, "Quantifying elasticity and viscosity from measurement of shear wave speed dispersion," *J. Acoust. Soc. Am.*, vol. 115(6), pp. 6603–6608, 2004.
- [43] K. Nightingale, M. Scott, R. Nightingale, and G. Trahey, "Acoustic Radiation Force Impulse Imaging: In-vivo demonstration of Clinical Feasibility," *Ultrasound in Med. and Biol.*, vol. 28, no. 2, pp. 227–235.
- [44] W. Walker, F. Fernandez, and L. Negron, "A method of imaging viscoelastic parameters with acoustic radiation force," *Phys. Med. Biol.*, vol. 45, pp. 1437–1447, 2000.
- [45] A. Veis, *The Macromolecular Chemistry of Gelatin*. New York: Academic Press, 1964.
- [46] I. Pezron and M. Djabourov, "X-ray diffraction of gelatin fibers in the dry and swollen states," *J. Polymer Sci.*, vol. 28, pp. 1823–1839, 1990.
- [47] V. Uricanu, M. Duits, R. Nelissen, M. Bennick, and J. Mellema, "Local Structure and Elasticity of Soft Gelatin Gels Studied with Atomic Force Microscopy," *Langmuir*, vol. 19, pp. 8182–8194, 2003.
- [48] C. Duhamel, D. Hellio, and M. Djabourov, "All Gelatin Networks: 1. Biodiversity and Physical Chemistry," *Langmuir*, vol. 18, pp. 7208–7217, 2002.
- [49] M. Usta, R. Piech, R. MacCrone, and W. Hillig, "Behavior and properties of neat and filled gelatins," *Biomaterials*, vol. 24, pp. 165–172, 2003.

- [50] A. Van Den Bulcke, B. Bogdanov, N. Rooze, E. Schacht, M. Cornelissen, and H. Berghmans, "Structural and Rheological Properties of Methacrylamide Modified Gelatin Hydrogels," *Biomacromolecules*, vol. 1, pp. 31–38, 2000.
- [51] P. Higgs and S. Ross-Murphy, "Creep measurements on gelatin gels," *Int. J. Biol. Macromolecules*, vol. 12, pp. 233–240, 1990.
- [52] W. Hayes, L. Keer, G. Herrmann, and L. Mockros, "Dynamic study of gelatin gels by creep measurements," *Rheologica Acta.*, vol. 36, pp. 610–617, 1997.
- [53] J. Ferry, *Viscoelastic Properties of Polymers*, 3rd ed. New York: John Wiley and Sons, 1980.
- [54] A. Ward, "The physical properties of gelatin solutions and gels," *Br. J. Appl. Phys.*, vol. 5, pp. 85–90, 1954.
- [55] M. Djabourov, N. Bonnet, H. Kaplan, N. Favard, P. Favard, J. Lechaire, and M. Mailard, "3D analysis of gelatin gel networks from transmission electron microscopy imaging," *J. Phys. II France*, vol. 3, pp. 611–624, 1993.
- [56] A. Bot, I. van Amerongen, R. Groot, N. Hoekstra, and W. Agterof, "Large deformation rheology of gelatin gels," *Polymer Gels and Networks*, vol. 4, pp. 189–227, 1996.
- [57] T. Hall, M. Bilgen, M. Insana, and T. Krouskop, "Phantom Materials for Elastography," *IEEE Trans. Ultrason. Ferro. Freq. Contrl.*, vol. 44, pp. 1355–1365, 1997.
- [58] E. Madsen, G. Frank, T. Krouskop, T. Varghese, F. Kallel, and J. Ophir, "Tissue-mimicking oil-in-gelatin dispersions for use in heterogeneous elastography phantoms," *Ultrason. Imag.*, vol. 25, pp. 17–38, 2000.
- [59] C. Pellot-Barakat, F. Frouin, M. Insana, and A. Herment, "Ultrasound Elastography Based on Multiscale Estimations of Regularized Displacement Fields," *IEEE Trans Medical Imaging*, vol. 23, no. 2, pp. 153–163, 2004.
- [60] C. Pellot-Barakat, J. Mai, C. Kargel, A. Herment, B. Trummer, and M. Insana, "Accelerating Ultrasonic Strain Reconstructions by Introducing Mechanical Constraints," in *Proceedings of SPIE, Medical Imaging 2002: Image Processing*, ser. 4684, 2002, pp. 323–333.
- [61] M. Fatemi, L. Wold, A. Alizad, and J. Greenleaf, "Vibro-acoustic tissue mammography," *IEEE Trans. Med. Imaging*, vol. 21, pp. 1–8, 2002.
- [62] A. Sharma, M. Soo, G. Trahey, and K. Nightingale, "Acoustic radiation force impulse imaging of in vivo breast masses," in *Proc. IEEE Ultrason. Symp.*, ser. 078038412, 2004, pp. 728–731.

- [63] R. Sinkus, M. Tanter, T. Xydeas, S. Catheline, J. Bercoff, and M. Fink, "Viscoelastic shear properties of in vivo breast lesions measured by MR elastography," *Magn. Reson. Imaging*, vol. 23, pp. 159–165, 2005.
- [64] M. Insana, C. Pellot-Barakat, M. Sridhar, and K. Lindfors, "Viscoelastic imaging of breast tumor microenvironment with ultrasound," *J. Mammary Gland Biol. Neoplasia*, vol. 9, pp. 393–404, 2004.
- [65] S. Jin, J. Oshinski, and D. Giddens, "Effects of wall motion and compliance on flow patterns in the ascending aorta," *J. Biomech. Eng.*, vol. 125, pp. 347–354, 2003.
- [66] A. Zoumi, X. Lu, G. Kassab, and B. Tromberg, "Imaging coronary artery microstructure using second-harmonic and two-photon fluorescence microscopy," *Biophys. J.*, vol. 87, pp. 2778–2786, 2004.
- [67] M. Ganten, J. Boese, D. Leitermann, and W. Semmler, "Quantification of aortic elasticity: development and experimental validation of a method using computed tomography," *Eur. Radiol.*, vol. 15, pp. 2506–2512, 2005.
- [68] X. Zhang, R. Kinnick, M. Fatemi, and J. Greenleaf, "Noninvasive method for estimating a complex elastic modulus of arterial vessels," *IEEE Trans. Ultrason. Ferroelectr. Freq. Control*, vol. 52, pp. 642–652, 2005.
- [69] J. Zlatanova and S. Leuba, "Stretching and imaging single dna molecules and chromatin," *J. Muscle Res. Cell Motil.*, vol. 23, pp. 377–395, 2002.
- [70] H. Ko, W. Tan, R. Stack, and S. Boppart, "Optical coherence elastography of engineered and developing tissue," *Tissue Eng.*, vol. 12, pp. 63–73, 2006.
- [71] D. Ingber, "Tensegrity II. How structural networks influence cellular information processing networks," *J. Cell Sci.*, vol. 116, pp. 1397–1408, 2003.
- [72] S. Weinbaum, X. Zhang, Y. Han, H. Vink, and S. Cowin, "Mechanotransduction and flow across the endothelial glycocalyx," *Proc. Natl. Acad. Sci. USA*, vol. 100, pp. 7988–7995, 2003.
- [73] B. Garra, E. Cespedes, J. Ophir, S. Spratt, R. Zurbier, C. Magnant, and M. Pannanen, "Elastography of breast lesions: initial clinical results," *Radiology*, vol. 202, pp. 79–86, 1997.
- [74] A. McKnight, J. Kugel, P. Rossman, A. Manduca, L. Hartmann, and R. Ehman, "MR elastography of breast cancer: preliminary results," *AJR: Am. J. Roentgenol.*, vol. 178, pp. 1411–1417, 2002.

- [75] C. Pellot-Barakat, M. Sridhar, K. Lindfors, and M. Insana, “Ultrasonic elasticity imaging as a tool for breast cancer diagnosis and research,” *Current Medical Imaging Reviews*, vol. 2, pp. 157–164, 2006.
- [76] M. Insana, M. Sridhar, J. Liu, and C. Barakat, “Ultrasonic mechanical relaxation imaging and the material science of breast cancer,” in *Proc. IEEE Ultrason. Symp.*, ser. 078039383X, 2005, pp. 739–742.
- [77] Y. Fung, *Biomechanics: Mechanical Properties of Living Tissues*. New York: Springer, 1993.
- [78] A. Wineman and K. Rajagopal, *Mechanical Response of Polymers*. Cambridge: Cambridge University Press, 2000.
- [79] N. Tschoegl, *Phenomenological Theory of Linear Viscoelastic Behavior*. New York: Springer, 1989.
- [80] P. Purslow, T. Wess, and D. Hukins, “Collagen orientation and molecular spacing during creep and stress relaxation in soft connective tissues,” *Journal of experimental biology*, vol. 201, pp. 135–142, 1998.
- [81] M. ODonnell, A. Skovoroda, B. Shapo, and S. Emelianov, “Internal displacement and strain imaging using ultrasonic speckle tracking,” *IEEE Trans. Ultrason. Ferroelectr. Freq. Control*, vol. 42, pp. 314–25, 1994.
- [82] F. Schwarzl and A. Staverman, “Higher approximation methods for the relaxation spectrum from static and dynamic measurements of visco-elastic materials,” *Appl. Sci. Res. A*, vol. 4, pp. 127–141, 1953.
- [83] K. Shung, M. Smith, and B. Tsui, *Principles of Medical Imaging*. San Diego: Academic Press, Inc., 1992.
- [84] The loss compliance  $\check{D}(\omega)$  (Eq (2.10)) for a first-order Voigt model is  $\check{D}(\omega) = (D_1\omega T_1)/(1 + \omega^2 T_1^2)$ . The spectrum peaks at  $\omega = 1/T_1$  as found from  $\frac{d\check{D}(\omega)}{d\omega} = 0$ .
- [85] To go from the discrete model of Eq (2.6) to a continuous distribution of retardance times, we assume  $\sum_{\ell=1}^L \frac{D_\ell}{(1+sT_\ell)}$  can be written as a uniformly sampled function  $\sum_{n=0}^{\infty} \frac{D_n}{(1+sn\Delta\tau)}$ , where  $T_\ell = n\Delta\tau$  for some integer value  $n$ . Using sampling theory,  $\sum_{n=0}^{\infty} \frac{D_n}{(1+sn\Delta\tau)} = \lim_{\Delta\tau \rightarrow 0} \int_0^{\infty} \frac{D(\tau)}{(1+s\tau)} \Delta\tau \sum \delta(\tau - n\Delta\tau) = \int_0^{\infty} d\tau \frac{D_s(\tau)}{(1+s\tau)}$ .  $D_s$  has units  $[\text{Pa s}]^{-1}$ .
- [86] E. Madsen, M. Hobson, H. Shi, T. Varghese, and G. Frank, “Tissue-mimicking agar/gelatin materials for use in heterogeneous elastography phantoms,” *Phys. Med. Biol.*, vol. 50, pp. 5597–5618, 2005.

- [87] I. Yakimets, N. Wellner, A. Smith, R. Wilson, I. Farhat, and J. Mitchell, "Mechanical properties with respect to water content of gelatin films in glassy state," *Polymer*, vol. 46, pp. 12 777 – 12 785, 2005.
- [88] M. Tanzer, "Intermolecular cross-links in reconstituted collagen fibrils," *J. Biol. Chem.*, vol. 243, pp. 4045–4054, 1968.
- [89] P. Gilsenan and S. Ross-Murphy, "Shear creep of gelatin gels from mammalian and piscine collagens," *Int. J. Biol. Macromol.*, vol. 29, pp. 53–61, 2001.
- [90] M. Sridhar and M. Insana, "Imaging microenvironment with ultrasound," in *Lecture Notes in Computer Science, IPMI 05*, vol. 5373. Springer, 2005, pp. 202–211.
- [91] W. Hayes, L. Keer, G. Herrmann, and L. Mockros, "A mathematical analysis for indentation tests of articular cartilage," *J. Biomech.*, vol. 5, pp. 541–551, 1972.
- [92] W. Press, B. Flannery, S. Teukolsky, and W. Vetterling, *Numerical Recipes: The Art of Scientific Computing*. New York: Cambridge University Press, 1986.
- [93] M. Bilgen and M. Insana, "Elastostatics of a spherical inclusion in homogeneous biological media," *Phys. Med. Biol.*, vol. 43, pp. 1–20, 1998.
- [94] D. Knapp, V. Barocas, and A. Moon, "Rheology of reconstituted type I collagen gel in confined compression," *J. Rheol.*, vol. 41, pp. 971–993, 1997.
- [95] R. Bagley, "A theoretical basis for the application of fractional calculus to viscoelasticity," *J. Rheol.*, vol. 27, pp. 201–210, 1983.
- [96] S. Welch, R. Rorrer, and R. Duren, "Application of time-based fractional calculus methods to viscoelastic creep and stress relaxation of materials," *Mechanics of Time-Dependent Materials*, vol. 3, pp. 279–303, 1999.
- [97] D. Ouis, "Characterization of polymers by means of a standard viscoelastic model and fractional derivate calculus," *International Journal of Polymeric Materials*, vol. 53, pp. 633–644, 2004.
- [98] A. Samani and D. Plewes, "A method to measure the hyperelastic parameters of ex vivo breast tissue samples," *Phys. Med. Biol.*, vol. 49, pp. 4395–4405, 2004.
- [99] R. Maurice and M. Bertrand, "Lagrangian speckle model and tissue-motion estimation–theory," *IEEE Trans. Med. Imaging*, vol. 18, pp. 593–603, 1999.
- [100] A. Sarvazyan, "Mechanical imaging: A new technology for medical diagnostics," *Int. J. Med. Inform.*, vol. 49(2), pp. 195 –216, 1998.
- [101] M. Sridhar, J. Tsou, and M. Insana, "In-vivo imaging of breast tissue viscoelasticity," in *Proc. IEEE Ultrason. Symp.*, 2006.

- [102] T. Laudadio, N. Mastronardi, L. Vanhamme, P. Van Hecke, and S. Van Huffel, "Improved Lanczos algorithms for blackbox MRS data quantitation," *J. Mag. Reson.*, vol. 157, pp. 292–297, 2002.
- [103] L. Vanhamme, T. Sundin, P. Van Hecke, and S. Van Huffel, "MR spectroscopy quantitation: a review of time domain methods," *NMR Biomed.*, vol. 14, pp. 233–246, 2001.
- [104] S. Marple, *Digital Spectral Analysis with Applications*. Englewood Cliffs, NJ: Prentice-Hall, Inc., 1987.
- [105] J. Hoch and A. Stern, *NMR Data Processing*. Hoboken, NJ: Wiley, 1996.
- [106] G. Millhauser, A. Carter, D. Schneider, J. Freed, and R. Oswald, "Rapid SVD for time-domain analysis of MR signals by use of the Lanczos algorithm," *J. Mag. Reson.*, vol. 82, pp. 150–155, 1989.
- [107] W. Walker, "The significance of correlation in ultrasound signal processing," *Proc. SPIE*, vol. 4325, pp. 159–171, 2001.
- [108] P. Bevington and D. Robinson, *Data Reduction and Error Analysis for the Physical Sciences*. Boston, MA: McGraw Hill, 1992.
- [109] H. Ponnekanti, J. Ophir, Y. Huang, and I. Cbspedes, "Fundamental mechanical limitations on the visualization of elasticity contrast in elastography," *Ultrasound in Med. and Biol.*, vol. 2(4), pp. 533–543, 1995.
- [110] J. Goodier, "Concentration of stress around spherical and cylindrical inclusions and flaws," *Trans. ASME*, vol. 55, pp. 39–44, 1933.
- [111] H. Schiessel and A. Blumen, "Hierarchical analogues to fractional relaxation equations," *J. Phys. A: Math. Gen.*, vol. 26, pp. 5057–5069, 1993.
- [112] M. Sridhar, J. Tsou, and M. Insana, "Viscoelasticity Imaging using Ultrasound: Parameters and Error Analysis," *Phy. Med. and Biol.* (In review).
- [113] H. Lianghao, J. Noble, and M. Burcher, "A novel ultrasound indentation system for measuring biomechanical properties of invivo soft tissue," *Ultrasound Med. Biol.*, vol. 29, pp. 813–823, 2003.

# Appendix A

## Projects and Publications

This appendix lists the publications and presentations done during the course of this doctoral program. Additional parallel projects that were conducted are also listed. Journal papers included in the dissertation are marked with a ‘\*’.

### Journal Publications

- \***M. Sridhar**, J. Liu and M. F. Insana, “Elasticity Imaging of Polymeric Media”, ASME Journal of Biomechanical Engineering (In print).
- C. Pellot-Barakat, **M. Sridhar**, M. F. Insana and K. K. Lindfors, “Ultrasonic elasticity imaging as a tool for cancer diagnosis and research”, Current Medical Imaging Reviews, 2 (1), 157-164 (2006).
- **M. Sridhar** and M. F. Insana, “Imaging the tumor microenvironment with Ultrasound”, Lecture Notes in Computer Science, 3565, 516-528 (2005).
- M. F. Insana, C. Pellot-Barakat, **M. Sridhar** and K. K. Lindfors, “Viscoelastic imaging of breast tumor microenvironment with ultrasound”, Journal of Mammary Gland Biology - Neoplasia. 9, 393-404 (2004).
- \***M. Sridhar**, J. Liu and M. F. Insana, “Viscoelasticity imaging using ultrasound: parameters and error analysis”, Physics in Medicine and Biology (In Review).

- \***M. Sridhar**, J. K. Tsou and M. F. Insana, “In-vivo imaging of breast tissue viscoelasticity using Ultrasound”, (In preparation).

## Conference Publications with Oral/Poster presentations

- **M. Sridhar**, J. Liu and M.F. Insana, “Towards a molecular level understanding of elasticity in tissues and hydrogels”, IEEE International Ultrasonics Symposium (2006) (Oral presentation).
- **M. Sridhar**, J. K. Tsou and M.F. Insana, “In-vivo imaging of breast tissue viscoelasticity using ultrasound”, IEEE International Ultrasonics Symposium (2006) (Oral presentation).
- **M. Sridhar**, J. K. Tsou and M.F. Insana, “In-vivo imaging of breast tissue viscoelasticity using ultrasound”, Biomedical Engineering Society (BMES 2006) (Oral presentation).
- M. F. Insana, **M. Sridhar**, J. Liu and C. Pellot-Barakat, “Ultrasonic Mechanical Relaxation Imaging describes the Material Science of Breast Cancer”, Proc. IEEE International Ultrasonics Symposium, 2,739 - 742 (2006) (Oral presentation).
- M. F. Insana and **M. Sridhar**, “Viscoelastic Imaging for discriminating breast tumors”, 30th International Symposium of Ultrasonic Imaging and Tissue Characterization, Arlington VA, May 2005 (Oral presentation).
- **M. Sridhar**, H. Du, C. Pellot-Barakat, J. K. Tsou and M. F. Insana, “Ultrasonic Imaging of Biochemical Changes in Tissues”, Proc. IEEE International Ultrasonics Symposium, 3, 2145-2148 (2004) (Poster presentation).
- **M. Sridhar**, H. Du, C. Pellot-Barakat, S. I. Simon, and M. F. Insana, “Ultrasonic Mechanical Relaxation Imaging of pH in Biopolymers,” SPIE Medical Imaging: Ultrasonic Imaging and Signal Processing, 5373, 202-211 (2004) (Oral presentation).
- **M. Sridhar**, C. Pellot-Barakat, and M. F. Insana, “Ultrasonic Mechanical Relaxation Imaging,” Proc. IEEE International Ultrasonics Symposium, 1, 929-932 (2003) (Oral presentation).

## **Additional projects**

### **Clinical elasticity imaging study**

Co-led the effort of an elasticity imaging clinical study at the UC, Davis medical center to recruit patients with breast masses. Consented patients according to IRB guidelines, acquired data using the Siemens ultrasonic clinical scanner. Also collected, processed and analyzed clinical data. Extensive software updates were done to current processing tools for efficient and large-scale processing of patient data.

### **Application of viscoelasticity imaging in pH imaging**

Led a project involving designing and conducting experiments to track dynamic spatial changes in material properties of hydrogels when different pH environments were created with the aim of simulating the impact of an acidic tumor on surrounding tissue mechanical properties. Measurement sensitivity to pH changes was also assessed.

### **Elasticity imaging of wound healing process in mice**

Developed experimental techniques and adapted algorithms to track skin wound healing process in mice by measuring mechanical properties of the wound over time.